The Henryk Niewodniczański Institute of Nuclear Physics
Polish Academy of Sciences

PARTICLE ACCELERATION AND HEATING IN MILDLY-RELATIVISTIC MAGNETIZED SHOCKS

Arianna Ligorini

Thesis submitted for the degree of Doctor of Philosophy
prepared under the supervision of prof. dr. hab. Jacek Niemiec

Kraków, 2020

ACKNOWLEDGEMENT

I would like to convey my gratitude to my PhD supervisor prof. dr. hab. Jacek Niemiec, for guiding me during this project at The Henryk Niewodniczański Institute of Nuclear Physics of the Polish Academy of Sciences, and for helping me and supporting me during all the years of my studies and during the preparation of this dissertation. I also wish to thank my colleagues dr. Oleh Kobzar, dr. Artem Bohdan, dr. Masanori Iwamoto, prof. Takanobu Amano, prof. Shuichi Matsukiyo, prof. Yosuke Matsumoto, prof. Martin Pohl and prof. Masahiro Hoshino for their valuable advice and interesting and fruitful discussion during our interantional collaboration. Finally, I would like to thank my husband and all my family, for the love and unconditional support they showed me during the past few years.

This work was supported by Narodowe Centrum Nauki through the research project DEC-2013/10/E/ST9/00662. Numerical simulations have been performed using computational and storage resources of the Prometheus system at ACC Cyfronet AGH

ABSTRACT

Jets of Active Galactic Nuclei (AGN) and gamma-ray bursts emit strong high-energy electromagnetic radiation and are the main candidates for sources of ultra high-energy cosmic rays. Particle acceleration is often assumed to take place at relativistic shocks in the jets. These shocks are typically magnetized and mostly quasi-perpendicular (superluminal). Their physics have been extensively studied in the ultrarelativistic regime, and mildly relativistic shocks are poorly explored. The aim of this dissertation is to investigate mildly relativistic shocks in magnetized electron-proton plasma with unprecedentedly high-resolution and large-scale kinetic particle-in-cell (PIC) simulations, for conditions typical for internal shocks in blazar cores. The simulations take into account ion-scale effects that cause corrugations along the shock surface. They are performed in two dimensions (2D) for two different configurations of the mean perpendicular magnetic field that is either in- or out- of the simulation plane. The focus of my studies in on particle heating and acceleration that results in the proton-to-electron energy transfer in the shock. My results show that the synchrotron maser instability persists to operate in mildly relativistic shocks in agreement with theoretical predictions and produces coherent emission of upstream-propagating electromagnetic waves. Shock front ripples are excited in both mean field configurations and they engender effective wave amplification. The action of these waves with plasma generates electrostatic wake-fields in the shock upstream that act to energise electrons. The wakefield acceleration (WFA) is not efficient and the majority of the energy transfer takes place in the shock and downstream, where the electron heating proceeds beyond adiabatic compression at the shock. I for the first time demonstrate that the shock rippling is crucial for the electron non-adiabatic energisation processes in the shock. The resulting ion-to-electron energy transfer is far below energy equipartition, independent of the mean magnetic field configuration. Downstream electron energy spectra are close to thermal distributions, although limited-range supra-thermal power-law components are also present. My results show that WFA at mildly relativistic magnetized shocks in AGN jets cannot be the source of high-energy cosmic rays. Limited level of the electron-ion coupling is in tension with leptonic models of blazar emission based on internal mildly relativistic shock scenario, unless the presence of the positron plasma component can facilitate enhanced ion-to-electron energy transfer.

STRESZCZENIE

Dżety aktywnych jąder galaktyk i błyski gamma emitują silne promieniowanie elektromagnetyczne wysokich energii i są głównymi kandydatami na źródła promieni kosmicznych najwyższych energii. Często przyjmuje się, że przyspieszenie cząstek w dżetach zachodzi w relatywistycznych falach uderzeniowych. Szoki te są zwykle zmagnetyzowane i quasi-prostopadłe (ponadświetlne). Ich fizyka jest dość dobrze zbadana w reżimie ultrarelatywistycznym, natomiast fale średnio relatywistyczne są mało poznane. Celem niniejszej rozprawy jest badanie średnio relatywistycznych szoków w zmagnetyzowanej plazmie elektronowo-protonowej za pomocą symulacji kinetycznych typu cząstka w komórce. Zastosowane symulacje wielkiej skali odznaczają się bardzo wysoką rozdzielczością i wykonane zostały dla warunków typowych dla wewnętrznych szoków w rdzeniach blazarów. Uwzględniają one efekty w skali jonowej, które prowadzą do pofałdowania powierzchni szoku, i wykonywane są w dwóch wymiarach dla dwóch różnych konfiguracji średniego prostopadłego pola magnetycznego, które znajduje się w płaszczyźnie symulacji lub tworzy z nią kąt 90^o. W moich badaniach skupiłam się na procesach grzania i przyspieszania cząstek, które skutkują przekazem energii od protonów do elektronów w fali uderzeniowej. Moje wyniki pokazują, że synchrotronowa niestabilność maserowa zachodzi w średnio relatywistycznych szokach zgodnie z przewidywaniami teoretycznymi i generuje emisję spójnych fal elektromagnetycznych rozchodzących się przed szokiem. Pofałdowania powierzchni fali są wzbudzane dla obu konfiguracji średniego pola, wzmacniając te fale. Ich oddziaływanie z plazmą z przodu fali generuje fale elektrostatyczne, które przyspieszają elektrony w procesie WFA. Proces ten nie jest jednak wydajny, a transfer energii odbywa się głównie w szoku i w obszarze za szokiem, gdzie procesy grzania elektronów odbiegają od adiabatycznej kompresji w szoku. Po raz pierwszy pokazuję, że pofałdowanie szoku ma kluczowe znaczenie dla nieadiabatycznych procesów przyspieszania elektronów. Przekaz energii proton-elektron zachodzi znacznie poniżej warunku ekwipartycji, niezależnie od konfiguracji średniego pola magnetycznego. Widma energii elektronów z tyłu szoku są bliskie rozkładom termicznym, choć występują również składowe ponadtermiczne w ograniczonym zakresie energii. Moje wyniki pokazują, że proces WFA w średnio relatywistycznych zmagnetyzowanych szokach dżetów aktywnych galaktych nie może być źródłem wysokoenergetycznych promieni kosmicznych. Ograniczony poziom sprzężenia elektron-proton stoi w sprzeczności z leptonowymi modelami emisji blazarów w ramach scenariusza średnio relatywistycznych szoków wewnętrznych, chyba że obecność składowej pozytronowej może znacznie wspomóc transfer energii protonów do elektronów.

TABLE OF CONTENTS

Page

CHAPTER 1
INTRODUCTION

The origin of energetic particles is a long-standing problem of major importance in astrophysics. High-energy charged particles are thought to be responsible for the intense non-thermal emissions observed from astronomical objects and in violent explosive phenomena in the Universe. They also reach Earth in great amounts as cosmic rays (CRs). Highest energy CRs may reach 10^{21} eV, and may be even more energetic at the production sites, since part of their energy becomes lost during propagation in intergalactic and/or interstellar media. It is widely assumed that CRs with energies up to $\sim 10^{15}$ eV are produced at non relativistic shocks in our Galaxy, in particular by supernova remnants. Concerning higher-energy particles, in particular these with energies above $\sim 10^{18}$ eV, it is presumed that they are of extra-galactic origin and generated in systems with relativistic plasma outflows. The main candidates are Active Galactic Nuclei (AGN) (such as blazars) and Gamma Ray Bursts (GRB). Observations of non-thermal synchrotron and inverse Compton emission in blazar jets that extends in broad energy range from radio up to TeV γ rays, indicates the presence of ultra relativistic electrons. Recently established possible association of one of the high-energy neutrino sources with a flaring blazar TXS 0506+056 [Aartsen et al., 2018] shows that also CRs hadrons can be produced in Active Galactic Nuclei. High-energy electrons are most likely also responsible for the inverse Compton component of the GRB jet afterglow emission at sub-TeV gamma-ray energies, as evidenced by recent discoveries [Acciari et al., 2019a,b, Abdalla et al., 2019]. It is often assumed that particles in AGN and GRBs can reach very high energies through acceleration in shock waves associated with the jets. These shocks have Lorentz factors, Γ_{sh}, ranging from mildly relativistic to ultra relativistic values. Diffusive Shock Acceleration (DSA) has been often invoked as the acceleration process, though this mechanism may not work at ultra relativistic ($\Gamma_{sh} \gg 1$) magnetized shocks due to inherent superluminal conditions in which particle diffusion across the magnetic field lines is difficult to achieve [e.g., Niemiec et al., 2006]. In fact, particle-in-cell simulation studies confirmed that ultra relativistic shocks can be efficient particle accelerators through DSA-like processes only if plasma magnetization is very small ($\sigma \lesssim 10^{-3}$, where σ is the ratio of the Poynting flux to the kinetic energy flux) or the shock is subluminal [for review see, e.g., Pohl et al., 2020].

As an alternative to the DSA model, it has been argued that wave-particle interactions of plasma collective phenomena can lead to an efficient particle acceleration at superluminal magnetized relativistic shocks. Such shocks are mediated by magnetic reflection of the incoming flow off the shock-compressed magnetic field [e.g., Gallant et al., 1992, Hoshino et al., 1992, Langdon et al., 1988]. Coherent gyration of particles at the shock front breaks up in bunches of charge and triggers the Synchrotron Maser Instability (SMI), which excites large-amplitude electromagnetic waves of the extraordinary mode (X-mode) that can escape towards the upstream region. This precursor wave emission has been confirmed through one-dimensional (1D) [e.g., Langdon et al., 1988, Hoshino and Arons, 1991, Gallant et al., 1992, Hoshino et al., 1992, Amato and Arons, 2006, Plotnikov and Sironi, 2019] and two-dimensional (2D) [e.g., Sironi and Spitkovsky, 2009, 2011, Iwamoto et al., 2017, Plotnikov et al., 2018, Iwamoto et al., 2018, Iwamoto et al., 2019] particle-in-cell (PIC) simulations.

In the electron-ion plasmas, interactions of the incoming electrons with the precursor waves can also generate large-amplitude longitudinal electrostatic (ES) oscillations, so-called wake-field [Lyubarsky, 2006]. It was shown that electrons and ions can be energised to very high energies in a manner analogous to Wake-field Acceleration (WFA) during the nonlinear process of the Langmuir wave collapse [Hoshino, 2008]. WFA has been first proposed in laboratory plasmas [Tajima and Dawson, 1979] and later applied to UHECR acceleration [e.g., Chen et al., 2002]. It was then demonstrated through laser plasma experiments and simulations [e.g., Kuramitsu et al., 2008] that the WFA produces power-law energy spectra with a spectral index of 2. Indeed, the WFA in relativistic shocks represents a promising scenario for ultra high energy CR (UHECRs) acceleration.

Relativistic magnetized shocks have recently been studied with 2D PIC simulations for the case of pair plasmas [Sironi and Spitkovsky, 2009, Iwamoto et al., 2017, 2018, Plotnikov et al., 2018], electron-ion plasmas [Sironi and Spitkovsky, 2011, Stockem et al., 2012, Iwamoto et al., 2019] and also mixed-composition plasmas [Stockem et al., 2012]. It has been demonstrated by Iwamoto et al. [2017] that simulations need to have high numerical resolution to detect fully the precursor waves. If this condition is met coherent waves continue to persist, even in weakly magnetized plasmas, dominated by the relativistic Weibel instability [e.g., Kato and Takabe, 2010, Sironi and Spitkovsky,

2011]. In pair plasmas, the precursor wave amplitudes were found to be systematically smaller in 2D simulations compared with the 1D case. However, the wave power is sufficient to disturb the upstream medium.

2D simulations with the magnetic field in the simulation plane showed that also ordinary mode (O-mode) waves are excited and at low magnetizations the Weibel instability amplifies these waves [Iwamoto et al., 2018]. The amplitudes in pair plasmas are in general much smaller than in ion-electron shocks [Iwamoto et al., 2019]. In conditions of high electron magnetization the wave energy exceeds that in pair plasmas by almost two orders of magnitude and the 2D amplitude is close to the one observed in one-dimensional simulations. In high-$\Gamma_{\rm sh}$ shocks this amplification over the pair plasmas is attributed to the so-called positive feedback process associated with the ion-electron coupling through the induced wake-fields. In the turbulent wake-fields close to the shock the electrons can be efficiently heated so that the energy equipartition between electrons and ions may be achieved before the flow reaches the shock front. At the same time non-thermal electrons and ions can be generated. This further confirms that Wake-field Acceleration may indeed be applicable for UHECR acceleration in relativistic astrophysical objects.

Most of the works reviewed above treat ultra relativistic shocks with Lorentz factors $\Gamma_{sh} \geq 10$. The mildly relativistic regime, $\Gamma_{sh} \approx 2$, has been instead poorly explored and only with low-resolution studies [Lyubarsky, 2006, Sironi and Spitkovsky, 2011]. It has been estimated that only for electron-ion shocks with $\Gamma_{sh} \gtrsim (m_i/m_e)^{1/3}$, where m_i/m_e is the ion-to-electron mass ratio, the electrons will form ring-like phase-space distribution unstable to SMI. Shocks with $\Gamma_{sh} \lesssim 10$ show very weak [Sironi and Spitkovsky, 2011] or no wake-field [Lyubarsky, 2006]. In consequence ion-to-electron energy transfer in the upstream is suppressed. The level of proton-to-electron energy transfer at mildly relativistic shocks is of importance to modelling the synchrotron and inverse Compton emission from blazar jets. It is often assumed that radiating particles are high-energy electrons and positrons accelerated in mildly relativistic internal shocks [e.g, Ghisellini and Madau, 1996]. Very strong coupling of electrons with protons indicated by PIC simulations of ultra relativistic shocks favour leptonic models for luminous blazar emission over the hadronic ones. On the other hand, reconciling the radiative consequences of these models with observed X-ray spectra poses quite strong

constraints on the location of the emission sites in the jet and on the pair content [e.g., Sikora et al., 2013]. However, the conclusions may be different if a lower-level coupling is observed for mildly relativistic and magnetized conditions.

The aim of this dissertation is to examine the physics of mildly relativistic shocks in magnetized electron-ion plasma for conditions in AGN jets. I use unprecedentedly high-resolution large-scale 2D PIC simulations to probe strictly perpendicular shocks, in which the mean magnetic field direction forms an 90° angle with the shock normal. Two different simulations are brought forth, with different inclination of the ambient magnetic field with respect to the simulation plane. I investigate the triggering of SMI and wake-fields and the mechanisms of particle heating, including WFA and the previously unreported effects of the ion-scale corrugations of the shock surface on particle acceleration. I also discuss the resulting level of electron-ion coupling. This dissertation is organised as follows:

- In Chapter 2 the physics of CRs is briefly introduced, and the current theories of UHECRs generation in AGN are outlined.
- In Chapter 3 a brief description of the shock physics in collisionless plasmas is provided.
- In Chapter 4 the main properties of the SMI and the WFA-related acceleration mechanisms are outlined.
- Chapter 5 presents the basics of the PIC simulation method and the techniques I used to suppress the numerical instabilities that affect simulations of relativistic plasmas. Results of test simulations defining the numerical PIC model used are presented.
- Chapter 6 presents the results of my 2D and 1D large-scale PIC simulations.
- Finally, Chapter 7 presents the summary and discussion of my results and their applications in astrophysics.

CHAPTER 2
HIGH ENERGY COSMIC RAYS AND ACTIVE GALACTIC NUCLEI

The discovery of CRs dates back to more than a century ago, when Victor Hess performed his balloon experiment in 1912 [Hess, 1912]. However, after over 100 years of investigations, the origin of CRs is still source of debate, especially concerning the highest energy particles. It is known that CR are charged particles (protons, pairs and some atomic nuclei) that reach Earth from various sources, both galactic and extra-galactic. The CR spectrum is known and it has been measured with a great accuracy.As seen in Fig. 2.1, the spectrum extends from about 1 GeV up to about 10^{21} eV, spacing roughly 12 orders of magnitude. Below 1 GeV, CR flux is heavily influenced by solar modulation. Above 1 GeV energy, CR spectrum can be roughly approximated with a power-law distribution, $F(E) \propto E^{-\alpha}$, with the spectral index $\alpha \approx 3$. However, at closer look the global spectrum of cosmic rays shows three distinctive features: the *knee* at energy of $E \approx 3 \times 10^{15}$ eV, where the spectral index α of the CR spectrum varies from 2.7 (appropriate for $E < 10^{15}$ eV) to 3.1; the *ankle* at energy of $E \approx 3 \times 10^{18}$ eV, where the spectral index flattens again to $\alpha = 2.7$; and the *GZK-cutoff* at $E \approx 5 \times 10^{19}$ eV [Zatsepin and Kuz'min, 1966, Greisen, 1966]. The latter is due to the energy losses that UHECR experience on their way towards Earth due to the interaction with Cosmic Microwave Background photons and consequent pion production. For energies higher than $E \approx 10^{19}$ eV, the CR flux is heavily suppressed, both by the GZK-cutoff and by the small amount of astrophysical sources capable of producing such high energy particles. Moreover, great uncertainties in the measurements due to the low flux affect this portion of the spectrum.

Suggestions on the origin of CRs can be inferred from their global spectrum. The spectrum transitions from a solar wind dominated one up to about 1 GeV into one dominated by cosmic rays from galactic sources like supernova remnants (SNRs) and pulsar wind nebulae. The knee is proposed to be a signature of the limit of CRs of galactic origin [Cesarsky, 1980, Lagage and Cesarsky, 1983]. The origin of the flux between $\approx 10^{15} \div 10^{18}$ eV is uncertain, although it is believed to be the intersection region in which galactic and extra-galactic sources contribute. The ankle can instead mark a transition to a flux of extra-galactic origin [Berezinsky et al., 2006, Allard et al., 2007, Hooper et al., 2007].

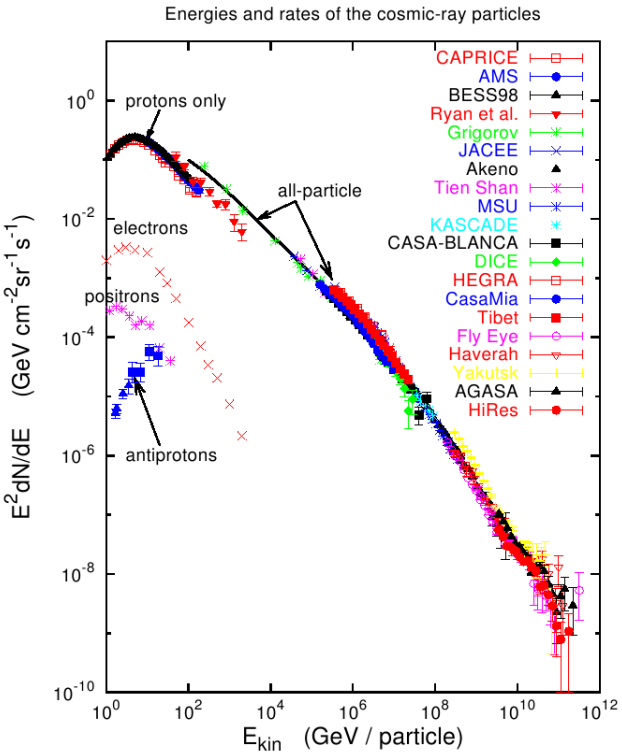

.

Figure 2.1: *Compilation of measurements of the energy spectrum of charged cosmic rays. The observations can be described by a power-law with spectral breaks at 3 PeV, referred to as the knee and the ankle at 1 EeV (from [Hillas, 2006])*

2.1 Galactic Cosmic Rays

The main source of CR in the galaxy is considered to be SNRs. SNRs are the leftovers of a supernova (SN) explosions, and they play a crucial role in CR physics. The hypothesis of supernovae as sources for Cosmic Rays was at first presented in the early age of CRs physics by Baade and Zwicky, who in 1934 displayed an interest for the liaison between these exploding stars and CRs production [Baade and Zwicky, 1934]. This hypothesis is based on energetic considerations: in fact, an exploding SN creates a shock carrying kinetic energy of about 10^{51}erg. If only 10% of this energy is converted to CR acceleration, with a rate of around 3 SN explosion per century in our galaxy it's possible to supply CR luminosity, i.e., $L_C R \approx 5 \times 10^{40}$erg/sec [Ginzburg and Syrovatsky, 1961, Webber, 1998]. Moreover, latest results by Fermi-LAT collaboration, which was able to spatially resolve and singularly study a great number of SNRs, seem to support this hypothesis [Weekes et al., 2002, Wakely and Horan, 2008, Blasi, 2009, Ackermann

et al., 2013]. The description of acceleration by SNR and the consequent behaviour of CR is known as *the SNR paradigm* [Blasi, 2009]. An exploding SN expels material and the ejecta of a stellar blast move supersonically. This leads to the formation of a shock front propagating in the interstellar or circumstellar medium, and the characteristic of this front (e.g., its extension, Mach number, etc.,) depend on the exploding SN type and the environmental conditions around the star. SN shock fronts usually are non relativistic, and they are thought to be able to accelerate CRs. Particle energisation at these shocks is mediated by the *first-order Fermi process*, also known as *diffusive shock acceleration (DSA)* [Fermi, 1949, Axford et al., 1977, Bell, 1978a,b, Blandford and Ostriker, 1978, Drury and Voelk, 1981]. In this process, acceleration occurs due to multiple crossings of the shock front, while particles are confined in the shock vicinity by pitch-angle scattering off the magnetic turbulence. The acceleration process leads to the formation of the power-law particle energy distribution which is compatible with observations. Multi-wavelength studies of supernova remnants provide evidence of high-energy particle production in SNRs [Aharonian et al., 2007, Morlino and Caprioli, 2011, Slane et al., 2014, Aleksić et al., 2015, Archambault et al., 2017].

2.2 Extra-galactic Cosmic Rays

CRs at energies above $E \approx 10^{18}$ eV (i.e., UHECRs, above the ankle) are assumed to be extra-galactic [Axford, 1994], and their origin is still debated. Two main types of processes invoked to explain their creation are the so-called "top-down models", in which UHECR are the results of decay or annihilation of supermassive primary particles which are even more energetic (e.g., supermassive dark-matter particles, [Berezinsky et al., 1997, Aloisio et al., 2015], and the "bottom-up models", presenting acceleration from low to high energy by astrophysical phenomena. Bottom-up models can be divided in two sub-categories. The first one assumes that particles are accelerated directly to very high energies by an extended electric field [Hillas, 1984], i.e, in the so-called “one-shot” mechanisms. The required electric fields are generally associated with the rapid rotation of small, highly magnetized objects such as white dwarfs [Zhang and Kumar, 2013, Asano and Mészáros, 2014], neutron stars [Mannheim et al., 2001, Kistler et al., 2014, Murase et al., 2014], or black holes [Aartsen et al., 2018, Keivani et al., 2018, Gao et al., 2019]. This acceleration mechanism is indeed fast, but it is

strongly hampered by the fact that acceleration occurs in astrophysical sites of very high energy density, where energy loss processes also play a significant role. The second sub-category assumes that particles gain energy gradually through multiple stochastic interactions with moving magnetized plasmas, as in the Fermi mechanisms [Fermi, 1949, 1954]. While the top-down models are at present still very exotic and seem to be excluded by recent observations [Aab et al., 2017a,b, Abbasi et al., 2019], many sources are known that have the capacity of accelerating particles to high energy via stochastic processes: active galactic nuclei (AGN) [Williams, 2004, Jacobsen et al., 2015, Vuillaume et al., 2018], jets of radio galaxies [Rees, 1966, Cohen et al., 1971, Pearson et al., 1981], and gamma-ray bursts [Berezinsky and Zatsepin, 1969, Milgrom and Usov, 1995, Baerwald et al., 2015]. Since the maximum energy gain by a particle in the Fermi processes depends on the confinement time in the source (high-energy particles will escape, thus ending their progressive acceleration), and the confinement time itself depends on the dimensions of the source and the strength of the magnetic field a criterion was proposed in [Hillas, 1984] that the acceleration of a particle can progress only until the particle gyro-radius does not exceed the size of the accelerator. Hence, the maximum energy that a charged particle can obtain in a source can be estimated as:

$$E_{max} < Z\, e\, R\, B \approx Z\, \beta (\frac{R}{kpc})(\frac{B}{10^{-6}G}) \times 10^{18} eV, \tag{2.1}$$

where B is the magnetic field strength, $Z\ e$ is the particle charge, R is the radius of the accelerator, and β=v/c is the ratio between the velocity of the particles' scattering centres and the speed of light. It follows that for larger accelerating sources, lower magnetic fields are enough to reach high energies. The possible acceleration sites can be represented on a B-vs-R Hillas plot (Fig. 2.2), which shows the various source classes that can be responsible for the acceleration of particles in various ranges of the source-size-magnetic-field strength. As one can see in Fig. 2.2, sources such as, e.g., GRBs, AGN and neutron stars are capable of producing a 10^{20}eV proton, while SNRs will not be able to accelerate protons beyond PeV energies. The focus of this thesis is on AGN as sources of high-energy CRs.

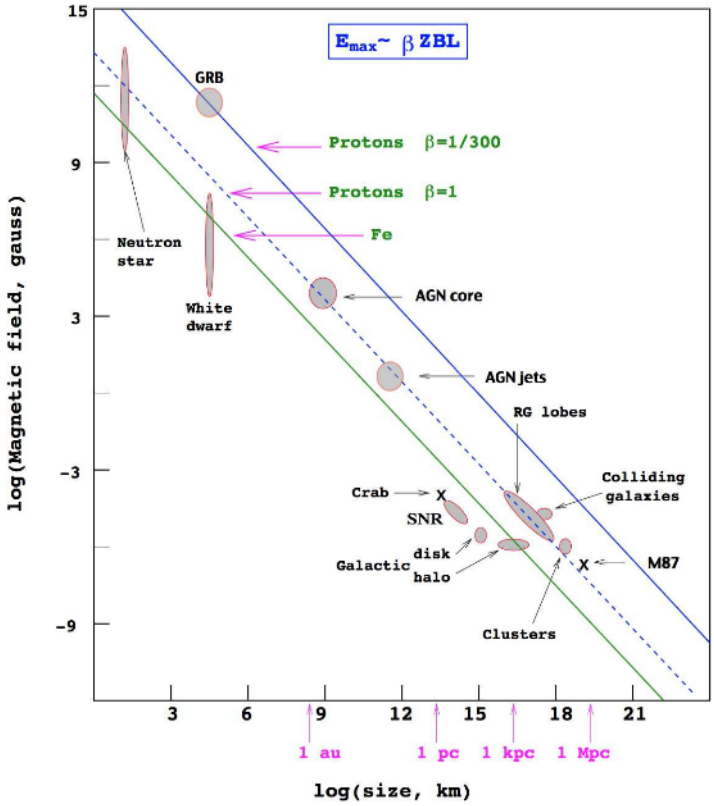

Figure 2.2: *A modern version on the the Hillas plot [Hillas, 1984], showing the various source classes that can be responsible for the acceleration of particles in various ranges of size-magnetic field strength (from [Letessier-Selvon and Stanev, 2011]).*

2.3 Active Galactic Nuclei as sources of UHECRs

In some galaxies, known as active galactic nuclei , the nucleus of the galaxy emits more radiation than the entire rest of the galaxy, to the point that it can even outshine the luminosity of the galaxy itself. The AGN emitted radiation has been found to be variable at all wavelengths at which it have been observed [Peterson, 2001]. At present, it it is understood that at the centre of the AGN is a supermassive black hole "engine", whose gravitational potential energy constitute the source for the AGN emitted luminosity [Rees, 1984, Urry and Padovani, 1995] (see Fig 2.3 for a schematic structure of an AGN). The emission has a very wide spectrum: turbulent processes in the accretion disk produce bright ultraviolet and maybe soft X-ray emission; hard X-ray radiation is also produced near the black hole; strong optical and ultraviolet emission is produced in clouds of gas (the so-called *broad-line region*) that rapidly move in the potential of the black hole [Urry and Padovani, 1995].

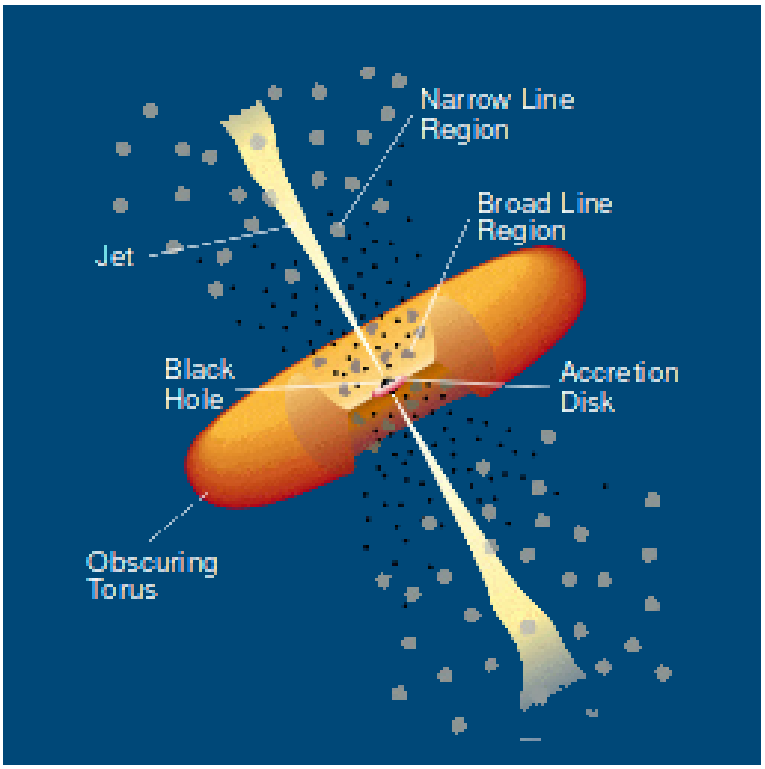

Figure 2.3: *Schematic view of an AGN, from Urry and Padovani [1995]*

The optical and ultraviolet radiation is obscured along some lines of sight by a torus of gas and dust which does not coincide with the accretion disk and broad-line region. Beyond the torus, slower moving clouds of gas produce emission lines with narrower widths. Outflows of energetic particles occur along the poles of the torus, escaping in the intergalactic medium and forming collimated, radio-emitting jets. The axisymmetric structure of AGN implies that AGN may appear radically different at different angles of observation. In particular, *blazars* are AGNs in which the emitted jet is almost aligned with line of sight to the observer. The jets are perpendicular to the accretion disc and collimated by strong magnetic fields: they appear to be stable up to kpc scales and are often characterised by a highly polarised radiation, short variability time-scales and an apparent superluminal motion [Fugmann, 1988, Impey et al., 1991, Valtaoja et al., 1992, Wills et al., 1992]. These relativistic jets, the turbulence and shocks inside them have been proposed as as sources of UHECRs.

Shocks can occur in various locations in the jet. At the lobes formed in the termination of the jet, where the ejecta enters the interstellar medium, an outward propagation bow shock is produced, as well as the corresponding reverse shock

propagating internally in the jet material producing the so-called hot spot. Inside the jet shocks can also originate if the central engine does not emit a continuous plasma flux, but instead it emits plasma shells moving at different speeds. These shells can collide with each other inside the jet, giving rise to the so-called internal shocks. In the regions closer to the engine, at the core, before the conical jet develops, a standing shock can also be created. The composition of the astrophysical jets is not precisely known, although it is thought that they consist of populations of electrons and protons, plus a positron component [Urry and Padovani, 1995, Wardle et al., 1998, Meli, 2012]. The internal shock discontinuities that form inside jets are of highest interest for this dissertation, as they are proposed as one of the places where cosmic rays from the bulk plasma can eventually get accelerated.

If a shock is *non relativistic*, the main acceleration mechanism proposed is DSA. As noted, this process produce power-law particle energy spectrum [Drury, 1983]:

$$f(E) \propto E^{-2}. \tag{2.2}$$

The calculated spectral index of -2 is compatible with the spectra observed in sources and also to the overall spectral index of the differential CR spectrum observed on Earth, after correcting for the propagation effects. However, this result does not carry over to relativistic shocks because of the strong anisotropy of the plasma distribution function due to rapid convection of particles through the shock and away downstream. Early works assuming relativistic shocks and a semi-analytical approach were brought forth for the limit of extremely small angle scattering (i.e., *pitch angle diffusion*) [e.g., Kirk and Schneider, 1987]. However the validity of the semi-analytic approximation is limited to the case of a weakly perturbed magnetic field [Niemiec and Ostrowski, 2006]. Application of such conditions in superluminal relativistic shocks does not allow for DSA, as particles are rapidly advected and do not cross the shock many times [Begelman and Kirk, 1990].

Monte Carlo techniques have been employed extensively to investigate relativistic shocks in view of their applicability to particle acceleration in AGN [Ellison et al., 1990, Ostrowski, 1991, Bednarz and Ostrowski, 1996, Meli and Quenby, 2003a,b, Niemiec and Ostrowski, 2004, Ellison and Double, 2004, Niemiec et al., 2006, Niemiec and Ostrowski, 2006]. Most studies showed a trend of spectral index flattening as a function of the

shock velocity, occasionally with spectral features, as well a clear deviation of the spectral index from the universal value for different shock inclination. These studies disputed the general belief that an universal power-law index of ≈ -2.2 had to be obtained from acceleration by both non-relativistic and relativistic shocks. It is now known that only quasi-parallel shocks, or shocks in weekly magnetized plasma recover this spectral index [Begelman and Kirk, 1990, Niemiec et al., 2006]. Numerical studies show that superluminal shocks do not show to be efficient accelerators for the very high energy cosmic rays via DSA [Langdon et al., 1988, Gallant et al., 1992, Niemiec and Ostrowski, 2004, Niemiec et al., 2006, Niemiec and Ostrowski, 2006, Sironi and Spitkovsky, 2009, 2011].

Various alternative mechanisms have been proposed to explain particle accelerations in relativistic jets, especially concerning AGN. *Relativistic magnetic reconnection* has been proposed as a source of acceleration for many different astrophysical objects: in highly conducting plasmas, the magnetic energy is released by reconnection of the magnetic lines of force where the magnetic field changes sign [Lyubarsky, 2005]. The relativistic magnetic reconnection was proposed as a source of the high-energy emission in pulsars [Lyubarskii, 1996, Kirk et al., 2002] and GRB [Drenkhahn and Spruit, 2002, Drenkhahn, 2002], as well AGN, such as blazars [Sikora et al., 2005a,b]. It was shown via PIC simulations that relativistic reconnection is very efficient in accelerating particles, producing power-law particle energy distributions with a spectral index close to 1 when the plasma is very strongly magnetized [Sironi and Spitkovsky, 2014, Guo et al., 2014, Werner et al., 2016, Guo et al., 2016, Nalewajko et al., 2016]. For blazars, a simplified scenario of *jets-in-a-jet*, in which magnetic reconnection creates compact emitting regions moving relativistically in the main plasma jests comoving frame was proposed by Giannios et al. [2009] and applied to observations by Nalewajko et al. [2011]. Advances in the PIC simulation capabilities allowed in recent years to investigate the magnetic reconnection with a greater care for the complexity of this phenomenon [Nalewajko et al., 2018, Ortuño-Macías and Nalewajko, 2019, Christie et al., 2019, Guo et al., 2019].

Other mechanisms that can be efficient in accelerating particles rely on wave-plasma interactions. Laser-plasma experiments in the laboratory demonstrated that when an intense laser pulse propagates in an electron-ion plasma a Langmuir wave is excited via

Raman scattering. The associated ponderomotive force expels electrons from the region of high laser intensity, while ions are mostly unaffected by the wave. As a consequence, a large charge-separation develops, which is associated with a longitudinal electric field – the so-called *wakefield*. As the phase velocity of the excited Langmuir wave is nearly equal to the group velocity of the laser pulse, and close to the speed of light, the wakefield is able to accelerate particles up to highly-relativistic energies via Landau resonance [Tajima and Dawson, 1979, Kuramitsu et al., 2008]. This mechanism, called *Wake-field Acceleration* (WFA, see Sec. 4.2) was extrapolated to the astrophysical environment by Chen et al. [2002], who showed how a large-amplitude Alfvén wave that propagates in a relativistic plasma generates an electrostatic wave behind itself, and a particle may be accelerated by the electric field of the wave up to energies compatible with UHECR energies. PIC simulation studies showed how in the presence of relativistic shocks large-amplitude electromagnetic waves are generated at relativistic shock fronts by the *Synchrotron Maser Instability* (see Ch. 4), triggered by the particles reflected by magnetic fields at the shock front [Langdon et al., 1988, Hoshino and Arons, 1991, Gallant et al., 1992]. This electromagnetic precursor has been proven to generate wake-fields of substantial amplitude when the shock is *ultra-relativistic* [Lyubarsky, 2006, Hoshino, 2008, Iwamoto et al., 2017, 2018, Iwamoto et al., 2019], and consequently causing the production of non-thermal electrons via WFA.

However, shocks in AGN jets are not exclusively ultra relativistic, and in fact models that try to explain spectral energy distributions of blazars specifically require *mildly relativistic* internal shocks [e.g, Spada et al., 2001a,b]. However, the literature investigating mildly relativistic shocks is quite sparse, and it is lacking in high resolution studies on the particular parameter regime applicable to internal shocks, especially in what concerns the efficiency of ion-to-electron energy transfer. This latter characteristics is of great importance for modelling the synchrotron and inverse Compton emission from blazar jets, as it is often assumed that particles responsible for this emission are high-energy electrons and positrons accelerated in mildly relativistic internal shocks. The principal models that require mildly relativistic shocks assume very strong coupling of electrons with shock-heated protons [e.g., Spada et al., 2001a,b, Ghisellini and Madau, 1996]. A strong coupling also favours leptonic over hadronic models to explain the origin of the luminous blazar emission, and thus introducing the necessity of

strong constraint on the emission site, and the jet composition [e.g., Sikora et al., 2013]. However, until now the level of coupling has been probed with sufficient resolution only for ultra-relativistic shocks. In this dissertation the problem of ion-to-electron energy transfer will be addressed for mildly relativistic magnetized shocks.

CHAPTER 3
SHOCKS IN PLASMA

Plasma physics is a relatively new branch of physics that became a mature science over the last half of the 20th century. In particular, it represents a large branch in astrophysical investigations, since processes in plasma are often invoked to provide an interpretation of a variety of astrophysical phenomena - in the Sun, the Earth magnetosphere, and emission of far-away objects. Since astrophysical shock phenomena are ubiquitous in nature and generally very difficult to reproduce in a laboratory, the investigation of these particular shocks system heavily relies on computer simulations to explore all the regimes.

In this chapter properties that describe a plasma properties and the selected aspects of shock physics which are relevant to AGN and blazar physics will be shortly presented.

3.1 Plasma properties and collisionless shocks

The plasma is an ionised medium in a state of electrical quasi-neutrality, the behaviour of which is dominated by collective interactions due to electromagnetic effects [Goossens, 2003]. In the simplified astrophysical description, plasma consists of charged particles (ions and electrons) and it so rarefied that particle collisions are rare. This is the so-called *collisionless plasma*.

In order to describe shocks in plasma, it is useful to define the main plasma parameters, which will be fundamental to understand the phenomena involved. In the electron-ion plasma, one can define electron and ion plasma frequencies, i.e.

$$\omega_{pe} = \sqrt{\frac{N_e q_i^2}{\epsilon_0 m_e}}, \tag{3.1}$$

$$\omega_{pi} = \sqrt{\frac{N_i q_e^2}{\epsilon_0 m_i}}, \tag{3.2}$$

where m_j and N_j are the mass and number density for species $j = e, i$, for electrons and ions, respectively, q_j is the electric charge, and ϵ_0 is the vacuum electric permittivity. Total plasma frequency is then defined as $\omega_p = \sqrt{\omega_{pe}^2 + \omega_{pe}^2} \sim \omega_{pe}$ - since $m_i \gg m_e$. The associated characteristic plasma lengths (skin depths) related to these basic plasma

modes are:

$$\lambda_{se} = \frac{c}{\omega_{pe}}, \tag{3.3}$$

and

$$\lambda_{si} = \frac{c}{\omega_{pi}}. \tag{3.4}$$

One can then define the Debye length, λ_D, as the distance describing the electric screening of the Coulomb potential of an individual particle in a plasma:

$$\lambda_D = \sqrt{\frac{\epsilon_0 k_b T_e}{N_e q^2}} = \frac{v_{th,e}}{\sqrt{2}\omega_{pe}}, \tag{3.5}$$

where k_B is the Boltzmann constant, T_e is the electron temperature and $v_{th,e} = \sqrt{\frac{2k_B T_e}{m_e}}$ is the electron thermal velocity. The number of charged particles within a Debye cube is defined as $n_D = N\lambda_D^3$, and it measures the number of particles that interact collectively in the plasma. One can see that this parameter must be large for the medium to be in the plasma state [Callen, 2006]. In fact, plasma becomes collisionless when the rate of particle collisions due to Coulomb scattering is much smaller then the plasma frequency. One can define electron mean free path as $l_{mfp,e} = \lambda_D n_D$ and then the collision rate becomes [Klimontovich, 1997]:

$$\nu \propto \frac{v_{th,\,e}}{l} = \frac{v_{th,\,e}}{\lambda_D\, n_D}. \tag{3.6}$$

Hence, using equation 3.5, one obtains:

$$\frac{\nu}{\omega_{pe}} = \frac{v_{th,\,e}\,\lambda_D}{\lambda_D\, n_D\, v_{th,\,e}} = \frac{1}{n_D}, \tag{3.7}$$

where $g = \frac{1}{n_D} \propto \frac{N_e^{1/2}}{T_e^{3/2}}$ is called the *plasma parameter*. In the absence of collisions g goes to zero. This happens if $n_D \gg 1$, i.e, in hot and rarefied plasma. The AGN jets are constituted by collimated disc accretion winds, and for these objects a value for $n_D \approx 10^5$ is estimated [Council, 2007]. One can therefore expect the conditions of collisionless plasma in these objects.

3.2 Shock description in MHD

A shock is defined as a sudden transition between a supersonic and a subsonic flow. In the framework of fluid dynamics, the shock is described by discontinuous solution to the fluid conservation equations [see, e.g., Landau and Lifshitz, 1959]. These solutions represent the *jump conditions*. At the shock the flow speed changes and dissipation takes place, causing an increase in the temperature. Hence the shock actually mediates the transfer from upstream bulk kinetic energy to downstream thermal energy.

3.2.1 Jump conditions

The jump conditions are usually derived in the reference frame in which the shock is at rest, exemplified in Fig. 3.1, where index 1 represents the upstream and index 2 the downstream physical quantities. P indicates the plasma pressure, ρ the plasma density and T its temperature. In the shock reference frame, the plasma has inflow velocity $v_1 = \gamma_1\beta_1$ upstream, while it flows away downstream with the outflow velocity $v_2 = \gamma_2\beta_2$.

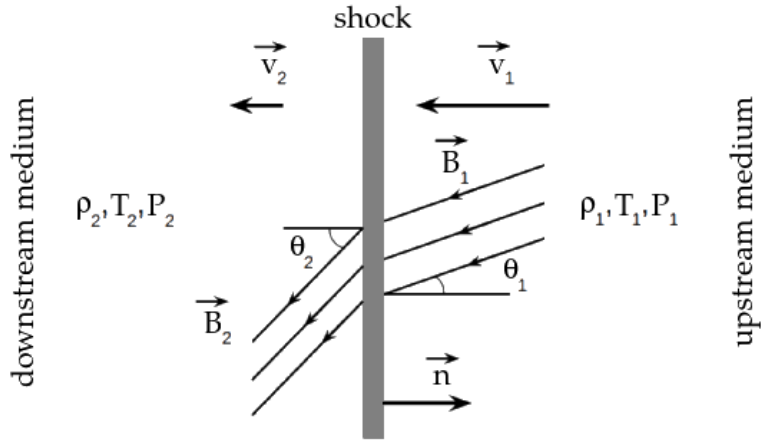

Figure 3.1: *Schematic illustration of the parameters of the plasma in the shock region, in the shock rest frame.*

Equations for density, magnetic flux, total energy and total momentum conservation in this frame are [Stockem et al., 2012]:

$$\gamma_{1,s}\,\beta_{1,s}\,n_{1,s} = \gamma_{2,s}\,\beta_{2,s}\,n_{2,s} \tag{3.8}$$

$$\beta_{1,s}\, B_{1,s} = \beta_{2,s}\, B_{2,s} \tag{3.9}$$

$$\gamma_{1,s}^2\, \beta_{1,s}\, w_1 + \beta_{1,s}\, \frac{B_{1,s}^2}{\mu_0} = \gamma_{2,s}^2\, \beta_{2,s}\, w_2 + \beta_{2,s}\, \frac{B_{2,s}^2}{\mu_0} \tag{3.10}$$

$$\gamma_{1,s}^2\, \beta_{1,s}^2\, w_1 + P_{1,s} + \frac{B_{1,s}^2}{2\mu_0} = \gamma_{2,s}^2\, \beta_{2,s}^2\, w_2 + P_2 + \frac{B_{2,s}^2}{2\mu_0}. \tag{3.11}$$

Here, the first index 1 or 2 refers to a quantity in the upstream or downstream region respectively, while the second index can take value 1, 2 or s and denotes the frame in which the quantity is evaluated (upstream plasma rest frame, downstream plasma (simulation) rest frame or shock rest frame, respectively). w_i is the fluid enthalpy, which is related to the adiabatic index and it is defined as $w_i = n_i\, mc^2 + (\Gamma_{ad}/(\Gamma_{ad} - 1))P_i$, where m is the total mass of the fluid components. Here, the single index denotes quantities evaluated in their rest frame (in lieu of the double index i, i).

One can perform a Lorentz transformation of Eq.s 3.8, 3.9, 3.10 and 3.11 to the downstream frame, as this is the frame used in our simulations. In the special case of perpendicular shock (i.e., the angle between the shock normal and the ambient magnetic field is $\theta_B = 90°$) one obtains [Plotnikov et al., 2018]:

$$\gamma_{1,2}(\beta_{1,2} + \beta_{s,2})\, n_1 = \beta_{s,2} n_2 \tag{3.12}$$

$$\gamma_{1,2}(\beta_{1,2} + \beta_{s,2})\, b_1 = \beta_{s,2}\, b_2 \tag{3.13}$$

$$\gamma_{1,2}^2\, (\beta_{1,2} + \beta_{s,2})\left(w_{1,2} + \frac{b_1^2}{\mu_0}\right) - \beta_{s,2}\left(P_{1,2} + \frac{b_1^2}{2\mu_0}\right) = \beta_{s,2}\left(w_2 - P_2 + \frac{b_2^2}{2\mu_0}\right) \tag{3.14}$$

$$\gamma_{1,2}^2\, \beta_{1,2}\, (\beta_{1,2} + \beta_{s,2})\left(w_{1,2} + \frac{b_1^2}{\mu_0}\right) + \left(P_{1,2} + \frac{b_1^2}{2\mu_0}\right) = P_2 + \frac{b_2^2}{2\mu_0}. \tag{3.15}$$

Here the proper densities n_i and magnetic field b_i are related to the apparent quantities as $N_{i,j} = \gamma_{i,j}\, n_i$, $B_{i,j} = \gamma_{i,j}\, b_i$, where $\gamma_{i,j}$ is the bulk Lorentz factor of the flow in the region denoted by the index i and seen in the rest frame denoted by the index j To simplify the derivations but still maintain their validity for all values of $\gamma_{1,2}$ the

only approximation one needs to make is the *strong shock limit*, $w_1 \approx n_1 mc^2$. Under this assumption the total upstream pressure terms $(P_{1,2} + B_1^2/2\mu_0)$ are negligible. Defining the upstream *plasma magnetization* as:

$$\sigma = \frac{b_1^2}{\mu_0 w_1 \gamma_{1,2}^2} = \frac{B_{1,2}^2}{\mu_0 N_{1,2} m\, c^2\, \gamma_{1,2}} \tag{3.16}$$

deducing b_2 from Eq. 3.13 and inserting it into Eq. 3.15 on can determine the downstream kinetic pressure as

$$\frac{P_2}{w_1} = \gamma_{1,2}^2 \beta_{1,2}(\beta_{1,2} + \beta_{sh})(1+\sigma) - \gamma_{1,2}^2 \frac{(\beta_{1,2} + \beta_{sh})^2}{\beta_{sh}^2} \frac{\sigma}{2} \tag{3.17}$$

One can insert this expression in Eq. 3.14, and combining with Eq. 3.12 for the density ratio one obtains for the shock speed the second order equation:

$$2\gamma_{1,2}\beta_{1,2}(1+\sigma)\beta_{sh}^2 - [2(\gamma_{1,2}-1)(\Gamma_{ad}-1) + \gamma_{1,2}\Gamma_{ad}\sigma]\beta_{sh} + \gamma_{1,2}\beta_{1,2}(2-\Gamma_{ad})\sigma = 0. \tag{3.18}$$

This relation is valid for any upstream plasma Lorentz factor, but the ultra relativistic limit can be easily recovered with appropriate approximations (i.e., for $\gamma_{1,2} \gg 1$, $w_2 = 1/(\Gamma_{ad}-1)P_{2,2}$) to be [e.g., Gallant et al., 1992, Kennel and Coroniti, 1984]:

$$\beta_{sh}^2\left(1 + \frac{1}{\sigma}\right) - \beta_{sh}\left(\frac{\Gamma_{ad}}{2} + \frac{1}{\sigma}(\Gamma_{ad}-1)\right) - \left(1 - \frac{\Gamma_{ad}}{2}\right) = 0 \tag{3.19}$$

In the same way, the non relativistic limit is recovered by imposing $\gamma_{1,2} \approx 1$. I perform a first run where the magnetic field points outside of the simulation plane (out-of-plane): in this simulation the particles are constrained to move in the simulation plane, and the adiabatic index is the one of the pure 2D case, i.e. $\Gamma_{ad} = 3/2$. For the second simulation, the magnetic field lies inside the simulation plane (in-plane), and the particles gain one additional degree of freedom. The appropriate adiabatic index in this case is $\Gamma_{ad} = 3/2$. For my simulation parameters I obtain for the shock velocities:

$$\begin{aligned} &\beta_{s,2} = 0.48 \qquad \text{for out-of-plane } B, \quad \Gamma_{ad} = 3/2 \\ &\beta_{s,2} = 0.42 \qquad \text{for in-plane } B, \quad \Gamma_{ad} = 4/3. \end{aligned} \tag{3.20}$$

The compression ratio can be deduced using Eq.s 3.12 and 3.13,

$$R = \frac{B_2}{B_{1,2}} = \frac{N_2}{N_{1,2}} = \frac{n_2}{\gamma_{1,2} n_{1,2}} = 1 + \frac{\beta_{1,2}}{\beta_{s,2}}, \tag{3.21}$$

and the downstream temperature is given by

$$\frac{k_B T_2}{\gamma_{1,2} mc^2} = \beta sh \beta_{1,2}(1+\sigma) - \frac{\beta_{1,2} + \beta_{sh}}{\beta_{s,2}} \frac{\sigma}{2}. \tag{3.22}$$

Imposing $\gamma_{1,2} \approx 1$, $\sigma = 0$ and the appropriate adiabatic index $\Gamma_{ad,\,nr} = 5/3$ the known compression ratio for the unmagnetized, non relativistic shock is recovered, i.e., $R = 4$. For the out of plane ultra relativistic 2D case, the compression ratio $R = 3$ is recovered with $\Gamma_{ad,\,rel} = 3/2$, $\gamma_{1,2} \gg 1$. For my simulations, the expected compression ratios are

$$\begin{aligned} R &= 2.8 \qquad \text{for out-of-plane } B, \\ R &= 3.1 \qquad \text{for in-plane } B. \end{aligned} \tag{3.23}$$

3.2.2 Perpendicular magnetized shocks

magnetized shocks can be classified in terms of the magnetic field orientation. Systems in which the ambient magnetic field forms an angle of $\theta_B = 0°$ with the shock normal are defined as strictly parallel, while cases in which the angle is $\theta_B = 90°$ are called strictly perpendicular. For intermediate obliquities, shocks are defined as quasi-parallel ($0° < \theta_B < 45°$) and quasi-perpendicular ($45° < \theta_B < 90°$).

In the presence of a magnetic field in the plasma one can express the shock velocity v_{sh} in terms of the Alfvén velocity by defining the Alfvén Mach number:

$$M_A = \frac{v_{sh}}{v_A}. \tag{3.24}$$

Here, v_A is the Alfvén velocity, defined as

$$v_A = \sqrt{\frac{B_0^2}{\mu_0 (N_e m_e + N_i m_i)}} \tag{3.25}$$

where B_0 is the large-scale upstream magnetic field embedded in the plasma, and μ_0 is the magnetic permeability of vacuum. In the case of magnetized plasma I can also

define useful temporal and spatial scales. The *relativistic gyrofrequency* for a species j is:

$$\Omega_j = \frac{eB_0}{m_j \gamma}, \tag{3.26}$$

where γ indicates the particle Lorenz factor. From this quantity one can define the *particle gyroradius*:

$$\lambda_{gj} = \frac{v_\perp}{\Omega_j} \tag{3.27}$$

where $v_\perp$ is the particle velocity perpendicular to the magnetic field direction.

A further shock classification distinguishes between *subluminal* and *superluminal* shocks: a shock is superluminal when particles cannot escape ahead of the shock by sliding along the magnetic field lines [Begelman and Kirk, 1990]. The threshold between sub- and superluminal shocks occurs when the magnetic inclination θ_B is greater than a critical angle θ_{crit}. In upstream frame, this critical angle is given by $\cos\theta'_{crit} = \beta'_{sh}$, where β'_{sh} is the shock speed in the upstream frame. In the downstream frame this corresponds to $\theta_{crit} = arccot\ (\Gamma_{sh}(\beta_{sh} + \beta_2))$, where Γ_{sh} and β_{sh} are the shock Lorentz factor and velocity (in units of c) of the shock in the downstream frame, while β_2 is the bulk plasma velocity in units of c in the downstream frame.

The magnetic inclination strongly influences the physics of the shock. In the case of subluminal shock, with particles escaping upstream along the field lines, the shock region is very large, up to the order of 100 ions gyroradii. In the superluminal case, instead, particle trying to escape upstream are constrained by the magnetic field and they remain in a narrow region, up to just a few iron gyroradii wide. The simulations in this thesis study strictly perpendicular shocks, which hence are superluminal.

3.3 Structure of a superluminal relativistic shock

A further classification of shocks distinguishes between subcritical and supercritical shocks. Subcritical shocks can be substained by pure resistive dissipation [Treumann, 2009]. Instead, resistive processes are not efficient enough to sustain a supercritical shock. In such shocks the dissipation of the excess energy occurs through reflection of a substantial portion of the incoming plasma back upstream. The number of reflected particles corresponds to the fraction of particles whose excess motional energy the shock is unable to convert into heat. A shock criticality is defined through the *critical sonic*

Mach number M_c. A shock is called *sub-critical* if $M_s < M_c$, and *supercritical* if $M_s > M_c$. The maximum value of the critical Mach number derived for perpendicular shocks is $M_c \approx 2.76$ [Marshall, 1955]. Relativistic shocks are therefore always supercritical.

In an ion-electron perpendicular shock, a fraction of the incoming ions is reflected by the shock compressed magnetic field. Reflected ions describe only a single gyration in the upstream, corresponding to a ring-like distribution in the velocity space. Then they gain enough energy in the upstream motional electric field to enter the downstream region at later times. Ion reflection generates the overshoot-undershoot pattern just behind the ramp. Since, as noted, relativistic shocks are always supercritical, their structure is described by the foot-ramp-overshoot pattern, as shown in Fig. 3.2.

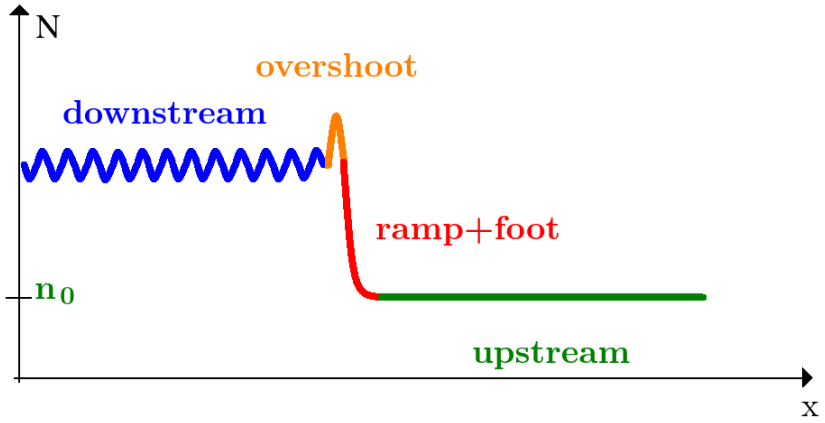

Figure 3.2: *Schematic view of a superluminal relativistic shock.*

In superluminal shocks reflected particles are able to move back upstream only by less than a single gyroradius before their gyromotion returns them back to the shock. The foot region then corresponds to the reflected ion region of thickness $\sim \lambda_{gi}$. Reflected ions also interact with the incoming plasma and can trigger multiple instabilities e.g., the Weibel instability, SMI, that mediate the shock dissipation and shape the structure of the shock.

3.3.1 Shock front corrugations

The presence of a highly anisotropic distribution of reflected ions gyrating at the front of low Mach number shocks has been shown in the non-relativistic case to drive the Alfvén Ion Cyclotron (AIC) temperature anisotropy instability or the mirror instability [e.g., Tanaka et al., 1983, Winske and Quest, 1988, Umeda et al., 2014, Lowe and Burgess, 2003]. 2D simulations of higher Mach number shocks instead indicated that the large

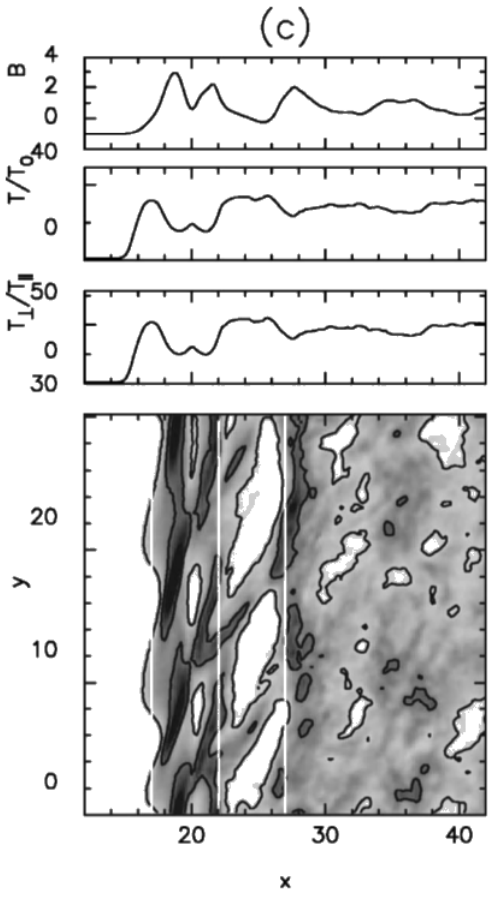

Figure 3.3: *Shock structure at fixed inflow speed $v_i = 5v_{Alfvén}$ for $B_z = 180\,\mathrm{deg}$ (i.e. pointing towards the page), with Alfvén Mach number $M_A = 7.6$. Top panels: y-averaged magnetic field magnitude, ion temperature normalized to upstream value, and temperature anisotropy ratio. Lower panel: gray-scale map of field magnitude shown with a white-black range of $0.9B_0 \div 6.5B_0$. White lines are shown at the nominal shock position and at +5 and +10 λ_{se} thereafter. From [Burgess and Scholer, 2007]*

temperature anisotropy introduced by the reflected ions is rapidly destroyed almost totally within the shock front [Winske and Quest, 1988], and only the small anisotropy left can drive AIC or mirror instability, although with a slow growth rate. The AIC modes propagate along the mean magnetic field, so they can be observed in 2D simulations only if the field is in the plane of the numerical grid. The assumption that an upstream magnetic field is perpendicular to the shock front and is directed out of the simulation plane alters the above picture, as in this configuration AIC and mirror instabilities are suppressed. 2D hybrid simulations of non relativistic, perpendicular, supercritical collisionless shocks with this specific magnetic field orientation were carried out by Burgess and Scholer [2007]. They observed a rippling feature at the

shock front, in which the ripples propagate along the shock surface in the direction of the ion gyration and at with the average ions speed at the shock. This effect is triggered for high shock Mach number and low plasma beta, where the plasma beta is the ration between the plasma thermal pressure and the magnetic pressure, defined as $\beta_{pl} = (2\mu_0 k_b T_j)/B^2$. It has also been observed for conditions of high-speed SNR shocks [Wieland et al., 2016] Fig. 3.3 shows the observed rippling feature in Burgess and Scholer [2007]. The shock corrugations are compatible with the ion gyration at the shock.

The shock ripples triggered by a similar mechanism to the one described in Burgess and Scholer [2007] have also been observed in PIC simulations of relativistic shocks with out-of-plane magnetic field configuration by Sironi et al. [2013]. They observed that in such a case the rippling develops for a limited regime of magnetization, $\sigma = [3 \times 10^{-3} \div 10^{-1}]$. For smaller magnetizations the corrugations are suppressed by pre-shock electron heating by the Weibel instability, while for higher magnetization the SMI-generated EM precursor destroys the shock ripples. It was noted in Sironi et al. [2013] that the shock rippling does not influence the injection of particles into the acceleration processes.

Large spatial scale simulations described in this dissertation allowed me to observe the shock corrugations for both the out-of-plane and the in-plane magnetic field orientations investigated. As will be presented in the thesis, the shock ripples play a significant role in shaping the structure of a mildly relativistic magnetized shock and the electron heating and acceleration processes.

CHAPTER 4
SYNCHROTRON MASER INSTABILITY AND WAKEFIELD ACCELERATION IN RELATIVISTIC SHOCKS

The plasma particles inflowing towards a relativistic perpendicular shock start gyrating in the shock compressed magnetic field. These gyrating particles form a ring-like distribution in the velocity space, which is unstable to the SMI. Due to the gyro-phase resonance the ring breaks up into bunches of charges that in turn radiate a train of large amplitude coherent electromagnetic waves that can propagate towards the upstream [Sprangle et al., 1977, Hoshino and Arons, 1991, Hoshino et al., 1992, Gallant et al., 1992]. These waves, called *precursor waves*, are mainly linearly polarised transverse waves of the extraordinary mode (X-mode). Emission of waves of the ordinary mode (O-mode) in this scenario it has been shown to be subdominant [Wu and Lee, 1979, Lee et al., 1980, Melrose et al., 1984]. However, SMI-related O-mode waves were detected in Iwamoto et al. [2018] (see Sec. 6.4.1(a)). Both gyrating electrons/positrons and ions are able to trigger SMI, but due to the difference in mass the growth rate of the ion-SMI is smaller than the electron-SMI. In pair-ion plasma SMI is then an instability composed of two phases: initially the pairs are unstable to SMI, and they start emitting precursor waves whose wavelength is comparable to the electrons Larmor radius in the shock compressed fields; ions are not affected by these waves as the wavelength is too short, and only in a later time the proton ring becomes unstable to SMI and in turn starts to emit long wavelength precursors. In the ion-pair plasma the emission of ion-generated precursor has been connected to positron acceleration [Hoshino and Arons, 1991, Amato and Arons, 2006] through particle-wave gyro-resonance. Electrons are not influenced by these waves, due to opposite gyration direction. For this reason the role that ion-SMI plays in the electron-ion plasma is limited [Lyubarsky, 2006].

In the electron-ion plasma, the presence of the precursor can excite the other type of waves. As the large amplitude precursor wave propagates upstream, incoming electrons experience intense transverse oscillations in the waves' strong fields. Electron guiding-centre velocity then decreases, while ions are unaffected by the presence of the waves due to their higher mass. The resulting difference in bulk velocity between electrons and ions results in the generation of a longitudinal electric field, known as the *wake-field*. This electric field can accelerate electrons and mediate ion-to-electron

energy transfer [Lyubarsky, 2006].

In the following sections, I will present the dispersion relation for the X-mode precursor waves, and show how the presence of the wakefield can result in electron acceleration via the WFA mechanism.

4.1 The dispersion relation for the X-mode waves

A general form of the dispersion relation for X-mode waves can be derived starting from the Vlasov equation. A method to obtain this relation is to determine the dielectric tensor. Here I follow the derivation in Krall and Trivelpiece [1973]. The Vlasov equation reads:

$$\frac{\partial f}{\partial t} + \mathbf{v} \cdot \nabla f + \mathbf{F} \cdot \frac{\partial f}{\partial \mathbf{p}} = 0, \tag{4.1}$$

where $f(t, \mathbf{x}, \mathbf{p})$ is the particle distribution function, $\mathbf{F}$ is the total force, p is the particle momentum, and v is their velocity.

One can rewrite the distribution function and the force as the sum of an unperturbed and a perturbed component (the latter denoted with tilde), where the perturbation is caused by the wave propagating in the plasma:

$$f = n_0 f_0 + \tilde{f}, \;\; F = F + \tilde{F}. \tag{4.2}$$

where f_0 is the unperturbed distribution normalised to unity. Then for the perturbed component $\tilde{f}$, the Vlasov equation is:

$$\frac{\partial \tilde{f}}{\partial t} + \mathbf{v} \cdot \nabla \tilde{f} + n_0 \tilde{\mathbf{F}} \cdot \frac{\partial f_0}{\partial \mathbf{p}} + \mathbf{F_0} \cdot \frac{\partial \tilde{f}}{\partial \mathbf{p}} = 0 \tag{4.3}$$

By using Liouville's theorem (integration by characteristics) one can estimate $f(t, \mathbf{x}, \mathbf{p})$ at any t from $f(t, \mathbf{x}(t), \mathbf{p}(t)) = f(t_0, x_0, p_0)$, where $(\mathbf{x}(t), \mathbf{p}(t))$ is the phase space trajectory so that $(\mathbf{x}(t_0), \mathbf{p}(t_0)) = (\mathbf{x_0}, \mathbf{p_0})$. However it may be very complex to describe such trajectories.

In the *absence of the wave* one has:

$$\begin{cases} \frac{d\check{\mathbf{x}}}{d\check{t}} = \mathbf{v}(\check{\mathbf{p}}) \\ \frac{d\check{\mathbf{p}}}{d\check{t}} = \mathbf{F_0}(\check{t},\ \check{\mathbf{x}},\ \check{\mathbf{p}}) \\ \check{\mathbf{x}}(\check{t} = t) = \mathbf{x} \\ \check{\mathbf{p}}(\check{t} = t) = \mathbf{p}, \end{cases} \tag{4.4}$$

when the accent $\check{}$ denotes particle properties along a trajectory not affected by the waves. When a wave is present, $f(t,\ \check{\mathbf{x}},\ \check{\mathbf{p}})$ is not conserved along this unaffected trajectory. However, choosing $(\check{\mathbf{x}},\ \check{\mathbf{p}})$ to be close to the trajectory in presence of the wave, $(x(t),\ p(t))$, it is possible to find how the distribution function evolves in the presence of the wave evolves along the unaffected trajectory. First, one considers Eq. 4.3 by taking the derivative of $\tilde{f}$ along $(\check{\mathbf{x}},\ \check{\mathbf{p}})$:

$$\frac{d}{d\check{t}}\tilde{f}(\check{t},\ \check{\mathbf{x}}(\check{t}),\ \check{\mathbf{p}}(\check{t})) = \left(\frac{\partial \tilde{f}}{\partial t} + \mathbf{v}\cdot\nabla\tilde{f} + \mathbf{F_0}\cdot\frac{\partial \tilde{f}}{\partial \mathbf{p}}\right)_{(\check{t},\ \check{\mathbf{x}}(\check{t}),\ \check{\mathbf{p}}(\check{t}))} = -\left(n_0\tilde{\mathbf{F}}\cdot\frac{\partial f_0}{\partial \mathbf{p}}\right)_{(\check{t},\ \check{\mathbf{x}}(\check{t}),\ \check{\mathbf{p}}(\check{t}))}, \tag{4.5}$$

where the lower index shows the variables on which the expressions are evaluated. Integrating over $\check{t}$ and using $(\check{\mathbf{x}},\ \check{\mathbf{p}}) \approx (x(t),\ p(t))$ one has:

$$-\int_{t_0}^{t}\left(n_0\tilde{\mathbf{F}}\cdot\frac{\partial f_0}{\partial \mathbf{p}}\right)_{(\check{t},\ \check{\mathbf{x}}(\check{t}),\ \check{\mathbf{p}}(\check{t}))} d\check{t} = \Delta\tilde{f}(t,\ \check{\mathbf{x}}(\check{t}),\ \check{\mathbf{p}}(\check{t})) = \Delta\tilde{f}(t,\ \mathbf{x},\ \mathbf{p}). \tag{4.6}$$

Hence the current induced by the force $\tilde{\mathbf{F}}$ is:

$$\mathbf{j}(t,\ \mathbf{x}) = e\int \mathbf{v}\ \Delta\tilde{f}(t,\ \mathbf{x}\ \mathbf{p})d^3p = -e\int d^3p\int_{t_0}^{t}\left(n_0\tilde{\mathbf{F}}\cdot\frac{\partial f_0}{\partial \mathbf{p}}\right)_{(\check{t},\ \check{\mathbf{x}}(\check{t}),\ \check{\mathbf{p}}(\check{t}))} d\check{t}. \tag{4.7}$$

In the presence of electromagnetic waves the force is the Lorentz force:

$$\tilde{\mathbf{F}} = e\ \tilde{\mathbf{E}}(\check{t},\ \check{\mathbf{x}})(1 - \frac{\mathbf{k}\cdot\check{\mathbf{v}}}{\omega} + \frac{\check{\mathbf{v}}\mathbf{k}}{\omega}), \tag{4.8}$$

with the complex field $\tilde{\mathbf{E}}(\check{t},\ \check{\mathbf{x}}) = \tilde{E}_0\ e^{-i\omega t + i\mathbf{k}\cdot\mathbf{x}}$. Eq. 4.7 now is:

$$\begin{aligned} \mathbf{j}(t,\ \mathbf{x}) &= \frac{m\ \sum_s \omega_{p,s}^2}{4\pi}\int d^3p\ \mathbf{v}\int_{t_0}^{t}\left(e\ \tilde{\mathbf{E}}(\check{t},\ \check{\mathbf{x}})(I\times(1 - \frac{\mathbf{k}\cdot\check{\mathbf{v}}}{\omega}) + \frac{\check{\mathbf{v}}\mathbf{k}}{\omega})\ \frac{\partial f_0}{\partial \mathbf{p}}\right)_{(\check{t},\ \check{\mathbf{x}}(\check{t}),\ \check{\mathbf{p}}(\check{t}))} d\check{t} = \\ &= \frac{i\omega}{4\pi}\ \hat{\chi}\ \tilde{E}_0\ e^{-i\omega t + i\mathbf{k}\cdot\mathbf{x}}, \end{aligned} \tag{4.9}$$

where I is he identity matrix, $\hat{\chi}$ is the susceptibility tensor, $\sum_s$ is summation over all species in the plasma, and $\epsilon = I + \sum_s \chi_s$ is the dielectric tensor.

The equations motion of the single particle in a magnetic field $\mathbf{B_0}$ is:

$$\begin{aligned} \frac{d\check{\mathbf{p}}}{d\check{t}} &= \frac{q}{m}\, \check{\mathbf{v}} \times \mathbf{B_0} \\ \frac{d\check{\mathbf{r}}}{d\check{t}} &= \check{\mathbf{v}} \\ \text{with } \check{\mathbf{v}} &= \frac{\check{\mathbf{p}}}{\gamma m}. \end{aligned} \tag{4.10}$$

The position and momentum vectors are defined such as :

$$\begin{aligned} \check{\mathbf{r}}(\check{t} = t) &= \mathbf{r} \\ \check{\mathbf{p}}(\check{t} = t) &= \mathbf{p}. \end{aligned} \tag{4.11}$$

Let us now define the components of the velocity as $v_x = v_\perp \cos\phi$ and $v_y = v_\perp \sin\phi$, and the cyclotron frequency for species s as $\Omega_s = qB_0/(mc\gamma)$. One can write $\tau = t - \check{t}$ to obtain:

$$\begin{aligned} \check{v}_x &= v_\perp \cos(\phi + \Omega_s \tau) \\ \check{v}_y &= v_\perp \sin(\phi + \Omega_s \tau) \\ \check{v}_y &= v_\parallel \\ \\ \check{x} &= x - \frac{v_\perp}{\Omega_s}[\sin(\phi + \Omega_s \tau) - \sin\phi \\ \check{y} &= y + \frac{v_\perp}{\Omega_s}[\cos(\phi + \Omega_s \tau) - \cos\phi \\ \check{z} &= z - v_\parallel \tau. \end{aligned} \tag{4.12}$$

Assuming now $f_0 = f_0(p_\perp, p_\parallel)$ (i.e. azimuthal anisotropy of the distribution fuction), and $k_x = k_\perp \cos\theta$, $k_y = k_\perp \sin\theta$ one obtains for the current:

$$\begin{aligned} \mathbf{j}(t, \mathbf{x}) = &\frac{m \sum_s \omega_{p,s}^2}{4\pi} \int d^3p \mathbf{v} \int_{t_0}^{t} d\tau\, e^{i\beta} \Big(E_x\, A\, \cos(\phi + \Omega_s \tau) + E_y\, B\, \sin(\phi + \Omega_s \tau) + \\ &+ E_z \left[\frac{\partial f_0}{\partial \mathbf{p}_\parallel} - C\, \cos(\phi - \theta + \Omega_s \tau) \right] \Big), \end{aligned} \tag{4.13}$$

where

$$A = \frac{\partial f_0}{\partial \mathbf{p}_\perp} + \frac{k_\parallel}{\omega}\left(v_\perp \frac{\partial f_0}{\partial \mathbf{p}_\parallel} - v_\parallel \frac{\partial f_0}{\partial \mathbf{p}_\perp}\right)$$

$$B = \frac{k_\perp}{\omega}\left(v_\perp \frac{\partial f_0}{\partial \mathbf{p}_\parallel} - v_\parallel \frac{\partial f_0}{\partial \mathbf{p}_\perp}\right) \tag{4.14}$$

$$C = \left(1 - \frac{n\Omega_s}{\omega}\frac{\partial f_0}{\partial \mathbf{p}_\parallel}\right) + \frac{n\Omega_s p_\parallel}{\omega p_\perp}\frac{\partial f_0}{\partial \mathbf{p}_\perp}$$

$$\beta = -\frac{k_\perp\, v_\perp}{\Omega_s}[\sin(\phi - \theta + \Omega_s\tau) - \sin(\phi - \theta)] + (\omega - k_\parallel v_\parallel)\tau.$$

The integral in 4.13 can be now decomposed as:

$$\int d^3p\, d\tau = \int dp_\parallel \int p_\perp\, dp_\perp \int d\tau \int d\phi. \tag{4.15}$$

First let us integrate in $d\phi$. Defining $z_s = (k_\perp v_\perp)/\Omega_s$, the various elements of 4.13 containing ϕ become:

$$\int_0^{2\pi} e^{iz_s[sin(\phi+\Omega_s\tau)-\sin\phi]} \begin{Bmatrix} \sin\phi\sin(\phi+\Omega_s\tau) \\ \sin\phi\cos(\phi+\Omega_s\tau) \\ \cos\phi\sin(\phi+\Omega_s\tau) \\ \cos\phi\cos(\phi+\Omega_s\tau) \\ 1 \\ \sin\phi \\ \cos\phi \\ \sin(\phi+\Omega_s\tau) \\ \cos(\phi+\Omega_s\tau) \end{Bmatrix} d\phi = 2\pi \sum_{n=-\infty}^{+\infty} e^{-in\Omega_s\tau} \begin{Bmatrix} (J_n')^2 \\ -\frac{i\,n}{z_s}J_nJ_n' \\ \frac{i\,n}{z_s}J_nJ_n' \\ \frac{n^2}{z_s^2}(J_n)^2 \\ (J_n)^2 \\ -iJ_nJ_n' \\ \frac{n}{z_s}(J_n)^2 \\ iJ_nJ_n' \\ \frac{n}{z_s}(J_n)^2 \end{Bmatrix} \tag{4.16}$$

where $J_n = J_n(z_s)$ are the Bessel functions. Now we integrate in $d\tau$. The components with $\sin(\Omega_s\tau)$ or $\cos(\Omega_s\tau)$ are solved in the integration of $d\phi$, resulting in the $e^{-in\tau}$ exponent in 4.16 that still needs to be integrated in $d\tau$. A second exponential in β, $e^{(\omega-k_\parallel v_\parallel)\tau}$, is also present in 4.13. The integral in $d\tau$ is then:

$$\int_0^{t-t_0} e^{i\tau(\omega-k_{\|}v_{\|}-n\Omega_s)}d\tau = \frac{e^{i(\omega-k_{\|}v_{\|}-n\Omega_s)(t-t_0)}}{i(\omega-k_{\|}v_{\|}-n\Omega_s)} \overset{\mathbf{Im}(\omega)>0}{=} \frac{i}{(\omega-k_{\|}v_{\|}-n\Omega_s)}. \tag{4.17}$$

One now has all the components to express the general dielectric tensor:

$$\epsilon(\omega,k) = I - \sum_s \frac{\omega_{p,s}^2}{\omega\Omega_s} \sum_{n=-\infty}^{+\infty} \int_0^{+\infty} 2\pi p_\perp \, dp_\perp \int_{-\infty}^{=\infty} dp_{\|} \left(\frac{\Omega_s}{\omega - k_{\|}v_{\|} - n\Omega_s} \Lambda_n \right) \tag{4.18}$$

Here Λ_n is the matrix, expressed in the general form by:

$$\Lambda_n = \begin{pmatrix} \frac{n^2(J_n)^2}{z_s^2} p_\perp A & \frac{i\ n\ J_n J_n'}{z_s} p_\perp A & \frac{n(J_n)^2}{z_s} p_\perp C \\ -\frac{i\ n\ J_n J_n'}{z_s} p_\perp A & (J_n)^2 p_\perp A & i\ n\ J_n J_n' p_\perp C \\ \frac{n(J_n)^2}{z_s} p_{\|} A & -i\ n\ J_n J_n' p_{\|} A & (J_n)^2 p_{\|} C \end{pmatrix} \tag{4.19}$$

4.1.1 Transversely propagating waves

For transverse electromagnetic waves propagating in the x-direction, $\mathbf{k} = (\mathbf{k_x}, \mathbf{0}, \mathbf{0},)$, across the magnetic field with the only component along the z-axis, $\mathbf{B} = (\mathbf{0}, \mathbf{0}, \mathbf{B_0})$, the wavevector paralellel to the magnetic field $k_{\|}$ is equal to 0 and only the following components of Λ_n are nonzero:

$$\Lambda_{n,kx} = \begin{pmatrix} \lambda_{xx} & \lambda_{xy} & 0 \\ \lambda_{yx} & \lambda_{yy} & 0 \\ 0 & 0 & \lambda_{zz} \end{pmatrix}. \tag{4.20}$$

The λ_{zz} component is polarised along $\hat{z}$, and hence relates to an O-mode wave. The other four components are related to the X-mode of interest. They are:

$$\Lambda^{n,\ reduced} = \begin{pmatrix} \frac{n^2(J_n)^2}{z_s^2} p_\perp \frac{\partial f_0}{\partial \mathbf{p}_\perp} & \frac{i\ n\ J_n J_n'}{z_s} p_\perp \frac{\partial f_0}{\partial \mathbf{p}_\perp} \\ -\frac{i\ n\ J_n J_n'}{z_s} p_\perp \frac{\partial f_0}{\partial \mathbf{p}_\perp} & (J_n)^2 p_\perp \frac{\partial f_0}{\partial \mathbf{p}_\perp}. \end{pmatrix} \tag{4.21}$$

Hence the general form of the dielectric tensor for the X-mode in this specific case is:

$$\epsilon(\omega,k)_{lq} = \delta_{lq} - 2\pi \sum_s \sum_{n=-\infty}^{+\infty} \frac{\omega_{p,s}^2}{\omega(\omega - n\Omega_s)} \int_0^{+\infty} p_\perp \, dp_\perp \int_{-\infty}^{=\infty} dp_{\|} \Lambda_{lq}^{n,reduced}, \tag{4.22}$$

where δ_{lq} is the Dirac delta. Eq. 4.22 is consistent with the one derived in Hoshino and Arons [1991].

4.1.2 Cold ring distribution

Eq. 4.22 can be re-written in terms of velocities, as expressed in Hoshino and Arons [1991]:

$$\epsilon(\omega,k)_{lq} = \delta_{lq} - 2\pi \sum_{s} \sum_{n=-\infty}^{+\infty} \frac{\omega_{p,s}^2}{\omega(\omega - n\Omega_s)} \int_0^{+\infty} v_\perp^2 \, dv_\perp \int_{-\infty}^{=\infty} dv_\parallel \frac{\partial f_0}{\partial \mathbf{v}_\perp} \psi_{lq}, \tag{4.23}$$

with

$$\psi = \begin{pmatrix} \frac{n^2 (J_n)^2}{z_s^2} & \frac{i\, n\, J_n J_n'}{z_s} \\ -\frac{i\, n\, J_n J_n'}{z_s} & (J_n)^2 \end{pmatrix}. \tag{4.24}$$

and z_s re-defined again in terms of velocities as $z_s = k_\perp c v_{\perp,s}/(\Omega_s \gamma_s)$. Assuming a cold ring distribution function for the particles, i.e.,

$$f_s(v_\perp, v_\parallel) = \frac{1}{2\pi v_{0,\,s}} \delta(v_\perp - v_{0,\,s}) \delta(v_\parallel), \tag{4.25}$$

where $v_{0,s}$ is the initial particle velocity directed along $\hat{x}$, Eq. 4.23 becomes

$$\epsilon(\omega,k)_{lq} = \delta_{lq} - 2\pi \sum_{s} \sum_{n=-\infty}^{+\infty} \frac{\omega_{p,s}^2}{\omega(\omega - n\Omega_s)} \int_0^{+\infty} v_\perp^2 \, dv_\perp \int_{-\infty}^{=\infty} dv_\parallel \frac{\partial (\frac{1}{2\pi v_{0,\,s}} \delta(v_\perp - v_{0,\,s}) \delta(v_\parallel))}{\partial \mathbf{v}_\perp} \psi_{lq}. \tag{4.26}$$

Integrating by parts, one obtains the componetns of the dielectric tensor:

$$\epsilon_{xx} = 1 - \sum_s \sum_{n=-\infty}^{+\infty} \frac{n^2 \omega_{p,s}^2}{z_s^2 \omega(\omega - n\Omega_s)} \left(2 z_s \, J_n \, J_n' - \frac{\gamma_s^2 - 1}{\gamma_s^2} \frac{\omega \, J_n^2}{\omega - n\Omega_s} \right)$$

$$\epsilon_{xy} = -\epsilon_{yx} = i \sum_s \sum_{n=-\infty}^{+\infty} \frac{n^2 \omega_{p,s}^2}{z_s^2 \omega(\omega - n\Omega_s)} \left(J_n \, J_n' + z_s ({J_n'}^2 + J_n \, J''_n) - \frac{\gamma_s^2 - 1}{\gamma_s^2} \frac{\omega \, J_n \, J_n'}{\omega - n\Omega_s} \right) \quad (4.27)$$

$$\epsilon_{yy} = 1 - \sum_s \sum_{n=-\infty}^{+\infty} \frac{n^2 \omega_{p,s}^2}{z_s^2 \omega(\omega - n\Omega_s)} \left(2 \, {J_n'}^2 + 2 z_s \, J_n' \, J''_n - \frac{\gamma_s^2 - 1}{\gamma_s^2} \frac{\omega \, {J_n'}^2}{\omega - n\Omega_s} \right).$$

The dispersion relation for X-mode waves is obtained from [Hoshino and Arons, 1991]:

$$(\eta^2 (\hat{k}\hat{k} - 1) + \epsilon) E = 0 \quad (4.28)$$

where $\eta = kc/\omega$. For $\mathbf{k}_{waves} = k\hat{x}$, one has

$$\hat{k}\hat{k} = \begin{pmatrix} 1 & 0 \\ 0 & 0 \end{pmatrix} \quad (4.29)$$

hence

$$\eta^2 (\hat{k}\hat{k} - 1) + \epsilon = \begin{pmatrix} \epsilon_{xx} & \epsilon_{xy} \\ \epsilon_{yx} & \epsilon_{yy} - n^2 \end{pmatrix}. \quad (4.30)$$

The solution of 4.28 is obtained by imposing that the determinant of the right hand term of Eq. 4.30 is equal to zero, i.e.:

$$\eta^2 = \epsilon_{yy} - \frac{\epsilon_{xy} \, \epsilon_{yx}}{\epsilon_{xx}} \quad (4.31)$$

which can be solved numerically.

4.1.3 X-mode dispersion relation in mildly relativistic electron-ion plasma

The dispersion relation calculated for the parameters assumed in my simulations is shown in Fig. 4.1. It was derived from Eq. 4.31, but assuming that both electrons and ions form *cold* rings in velocity space while they gyrate about the magnetic field lines with $\gamma_0 = 2$. This is justified here for my approximate analysis since the effects

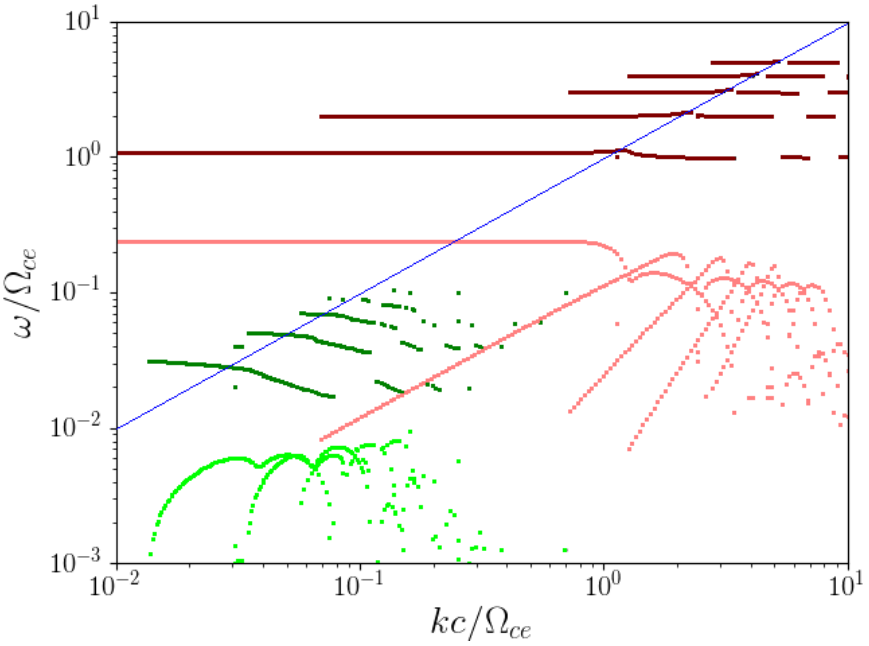

Figure 4.1: *The dispersion relation for X-mode waves in the electron-ion case, for the parameters of the simulations presented in this thesis, for electron-SMI (dark red: real part of ω; light red: imaginary part of ω) and ion-SMI (dark green: real part of ω; light green: imaginary part of ω). The blue line represents the light-wave dispersion relation. It is evident that the growth rate of the ion-SMI is lower than the the electron one, and it is mostly subluminous. For this this reason I expect to be able to observe the electron-SMI generated waves, while the ion-SMI is not expected to be detected due to the superluminal nature of the shock*

of the finite electron ring temperature are not significant for the ion maser instability [Hoshino and Arons, 1991]. The dispersion relations have harmonic structures for both the electron-generated SMI and the ion-generated SMI. For the electron SMI, the growth rate of the fundamental mode is comparable to that of the higher harmonic waves. The phase velocities of the unstable modes satisfy $\omega/kc \approx 1$. The bandwidth of the first harmonic unstable modes is wide, in particular for the fundamental wave, whose grow rate is flat for a wide range of k. The frequencies and growth rates of the ion unstable modes are lower than the electron ones by approximately the ion-to-electron mass ratio, and the growth rate slightly increases with higher harmonic number. In the periodic system one should thus expect two stages of the SMI to occur – first the electron SMI, then followed by the ion maser instability. However, upstream of a relativistic shock the situation may be different because the ion emission is mostly sub-luminous (the phase velocities of the modes are $\omega/kc \lesssim 1$) and the waves emitted at the shock may not

outrun it to reach the precursor.

Hence, under the assumption that only the electron contribution to SMI is relevant for the mildly relativistic shock in the ion-electron plasma, one can then obtain the form for the X-mode dispersion relation in the upstream (plasma rest) frame by imposing $\gamma_s = 1$ in Eq. 4.27 and inserting the components in Eq. 4.31. Since under this condition $z_s = 0$, one obtains $\epsilon_{xy} = \epsilon_{yx} = 0$ and

$$\eta'^2 = 1 - \frac{\omega_{pe}^2}{\omega'^2 - \Omega_{ce}} \,. \tag{4.32}$$

4.2 Wakefield Acceleration

The first study on SMI and wakefield acceleration in relativistic shocks in the electron-ion plasma has been performed by Lyubarsky [2006], who demonstrated that the large-amplitude precursor waves propagate towards the shock upstream and upon the interaction with the incoming plasma the velocity of the electron guiding centres decreases, while ions are unchanged. The relative motion between ions and electrons generates an electrostatic field that can lead to particle acceleration. The idea that an electrostatic wake-field can accelerate particles was first proposed and investigated in the laser-plasma experiment community [e.g., Tajima and Dawson, 1979, Esarey et al., 1996, Mourou et al., 2006], and then extended to the astrophysical plasma setting by Chen et al. [2002], who suggested that UHECRs may be generated by the wake-field acceleration. It was also demonstrated through laser plasma experiments and simulations [e.g., Kuramitsu et al., 2008] that the WFA produces power-law energy spectra with a spectral index of 2. Therefore, the WFA in relativistic shocks represents a promising scenario for UHECR acceleration.

Hoshino [2008] extended the study of relativistic shocks investigating wake-field generation and its role in particle acceleration. He showed that by the action of the ponderomotive force on electrons due to the large-amplitude electromagnetic (EM) precursor wave, electrons can be expelled from the precursor wave region and the large-amplitude electrostatic wake-field can be generated. The effect of the ponderomotive force can be investigated by considering a transverse EM wave in which the electric

and magnetic components are described by

$$\mathbf{E}(x,t) = \mathbf{E}_0(x,t)\ \cos(\omega\ t) \tag{4.33}$$

$$\mathbf{B}(x,t) = \mathbf{B}_0(x,t)\ \sin(\omega\ t) \tag{4.34}$$

and they are correlated trough the Faraday's Law,

$$\mathbf{B}(x,t) = -c\ \int_0^t \nabla\times\mathbf{E}_0(x,t)\ \cos\omega\ t \tag{4.35}$$

A charged particle in the wave fields has an equation of motion:

$$m\frac{d\mathbf{v}}{dt} = e\ \left(\mathbf{E}_0(x,t)\ \cos\omega\ t + \frac{\mathbf{v}}{c}\times\mathbf{B}(x,t)\right). \tag{4.36}$$

Following [Hoshino, 2008], one notices that the motion of the charged particle has two time scales: the simple harmonic motion in response to an electric field oscillating with high frequency, and the slow movement of the centre of oscillation. One can then write the variable $\mathbf{v}$ as the sum of two quantities,

$$\mathbf{v} = \mathbf{U} + \mathbf{u}, \tag{4.37}$$

where $\mathbf{U}$ is a slowly varying quantity, relative to the slow motion, while $\mathbf{u}$ is rapidly varying quantity related to the fast motion in the oscillating EM field. One can assume that $|\mathbf{U}| \ll |\mathbf{u}|$ and that $e\mathbf{E}_0/(m\omega\, c) \ll 1$. Then, at first order one retrieves the fast oscillating motion:

$$\frac{d\mathbf{u}}{dt} = \frac{e}{m}\mathbf{E}_0(x,t)\ \cos(\omega\ t), \tag{4.38}$$

and it follows that

$$\mathbf{u} = \frac{e}{m}\int_0^t \mathbf{E}_0(x,t)\ \cos(\omega\ t)\ dt. \tag{4.39}$$

To the next order, one can obtain the slowly varying motion. The oscillation average gives

$$m\frac{d\mathbf{U}}{dt}\mathbf{e}_x = \frac{e}{c}\langle\mathbf{u}\times\mathbf{B}\rangle = -\frac{e^2}{m}\langle\int_0^t \mathbf{E}_0(x,t_1)\ \cos(\omega\ t_1)dt_1 \times \int_0^t \mathbf{E}_0(x,t_2)\ \cos(\omega\ t_2)\ dt_2\rangle. \tag{4.40}$$

Here, $\mathbf{e}_x$ is the versor of axis x, and Eqs. 4.35 and 4.39 were used. If one can assume $\mathbf{E}_0(x,t) = \mathbf{E}_0(x)$ and $\mathbf{E}_0(x,t) = \mathbf{E}_0(x)$, then one obtains:

$$m\frac{d\mathbf{U}}{dt}\mathbf{e}_x = -\frac{e^2}{2m\omega^2}\nabla E_0^2(x)\langle \sin^2(\omega\, t)\rangle = -\frac{e^2}{4m\omega^2}\nabla E_0^2. \tag{4.41}$$

One can see that the particle can be accelerated due to the wave pressure force, called the *ponderomotive force* [Hoshino, 2008]:

$$m\frac{d\mathbf{U}}{dt} = \mathbf{F}_{pond} = -e\nabla\phi_{pond}, \tag{4.42}$$

with

$$\phi_{pond} = \frac{1}{4}\frac{e}{m\omega^2}E_0^2(x). \tag{4.43}$$

The ponderomotive force is proportional to the gradient of the wave pressure, and is independent of the sign of charge. However, the force on the electrons is much larger than that on ions, since $m_e \ll m_i$. For this reason, if one neglects the ion response, one can estimate the wake-field induced by the SMI-generated EM precursor waves by equating the electrostatic force and the ponderomotive force:

$$E'_{wake} = \frac{1}{e}\mathbf{F}'_{pond} \tag{4.44}$$

Here, the primed quantities denote that they are estimated in the upstream plasma rest frame, while unprimed quantities refer to the downstream (simulation) frame. The ponderomotive force is:

$$\mathbf{F}'_{pond} = -e\nabla'\phi'_{pond}, \tag{4.45}$$

with the potential:

$$\phi'_{pond} = \frac{1}{4}\frac{e}{m\omega'^2_0}E'^2_0(x), \tag{4.46}$$

where E'_0 and ω'_0 denote the injected (SMI-generated) EM wave amplitude and frequency, respectively. One can see that $E'_{wake} = E_{wake}$ is Lorentz invariant. In the case of relativistic shocks, the amplitude of the EM precursor can be very large [e.g., Iwamoto et al., 2017, 2018, Iwamoto et al., 2019]. Therefore in this case it is appropriate

to use the generalized ponderomotive force [Bauer et al., 1995]

$$\phi'_{pond} = m\,c^2\,\sqrt{1+\xi\,a'^2_0}, \tag{4.47}$$

where $a'_0 = (e\,E'_0)/(mc\omega'_0)$ is the normalized amplitude of the EM wave, and ξ depends on the wave polarization and is $\xi = 1$ for circular polarization and $\xi = 1/2$ for a linearly polarized wave.

It has been observed in relativistic magentized shock simulations [Hoshino, 2008, Iwamoto et al., 2017, 2018, Iwamoto et al., 2019] that the ponderomotive force is active not only at the tip of the precursor wave in the upstream, but also inside the precursor, because the wave amplitude inside the precursor region can be periodically modulated by either the stimulated Raman scattering or the self-modulation effects [Hoshino, 2008]. In the case of relativistic shocks, in the tip region of the precursor wave the wake-field has a sinusoidal waveform, and it causes a acceleration/deceleration pattern for electrons. However, behind the sinusoidal wavetrain, the wake-fields can collapse due to the nonlinear effects (see below). During this nonlinear process, the upstream cold electrons are heated and accelerated. The maximum attainable energy during the acceleration at the edge region of the precursor waves can be estimated as:

$$E_{max} \propto e\,E_{wake}L, \tag{4.48}$$

where E_{wake} and L are respectively the amplitude and the scale length of the wake-field. The efficiency of the electron acceleration increases with increasing upstream bulk Lorentz factor γ, and the accelerated electron energy can exceed the upstream bulk energy of ions if γ is larger than the ion-to-electron mass ratio [Hoshino, 2008].

Further processes can contribute to particle energisation in the turbulent wave region, in which the wakefield collapses. Of particular importance is the *phase slippage effect* [e.g., Tajima and Dawson, 1979], in which particles which are moving in the same direction as the wake-field can get in resonance with the wake-field electric field and get accelerated. In the phase slippage effect, the maximum energy attainable by a particle

in the upstream plasma rest frame is

$$\frac{E'_{max,\,ph.\,sl.}}{m_e c^2} \approx \frac{e\,E'_{wake} L'}{m_e c^2} \frac{c}{|c - v'_{ph}|'}, \tag{4.49}$$

where $v'_{ph} = \omega'/k'$ is the phase speed of the wake-field in the upstream plasma rest frame, and the term $c/(|c - v'_{ph}|)$ accounts for the phase slippage between the particle and the wake-field.

The process of wakefield formation can be understood to result from the parametric decay instability [PDI; e.g., Kruer, 1988]. Parametric instabilities are a common wave-wave interactions. They arise when a nonlinearity such as a pressure gradient couples waves. The waves must allow frequency and wavenumber matching which are consequences of energy and momentum conservation. In the case discussed here a large-amplitude electromagnetic (pump) wave decays into a Langmuir wave and a scattered electromagnetic (light) wave. Coupling to these wave modes occurs through the stimulated Raman scattering instability [Hoshino, 2008]. In the conditions with the pump wave frequency much larger than the plasma frequency, the Forward Raman Scattering (FRS) is triggered, in which the scattered electromagnetic wave and the Langmuir wave propagate in the same direction as the pump wave. The wavelength of the Langmuir wave is close to the electron inertial length, and its phase velocity approaches the group velocity of the pump wave, that is close to the speed of light. The enhanced emission of the precursor waves may also trigger the nonlinear FRS process [Hoshino, 2008]. In the first stage of FRS, the injected EM wave decays in a scattered EM wave and an electrostatic Langmuir wave, and in the second stage the scattered EM wave can further decay into another EM wave and a Langmuir wave. As this process may repeat many times, broadband wave spectrum can be generated. In the upstream plasma rest frame, these waves all propagate towards the upstream. However, when performing the Lorentz transformation to the simulation frame, a part of those EM and electrostatic waves can propagate towards the downstream. Since upstream propagating waves and the downstream propagating waves coexist in the shock upstream region, one can expect that the slippage effect between the particles with downstream-pointing momenta and the nonlinear FRS-produced wake-fields (which in turn are propagating toward the downstream in the simulation frame) can be triggered.

With a similar reasoning as Eq. 4.49, one obtains the maximum energy as

$$\frac{E'_{max,\ nlFRS}}{m_e c^2} \approx \frac{e\ E_{wake} L}{m_e c^2} \frac{c}{|c - v_{ph}|} \tag{4.50}$$

The acceleration efficiency is again expressed by the product of the wake-field scale length and the slippage effect, but for the FRS they are estimated in the simulation frame. Here, the scale size L increases with decreasing phase velocity, and the maximum energy efficiency is given for the largest wavenumber of the wake-field.

CHAPTER 5
NUMERICAL SIMULATIONS FOR PLASMA PHYSICS

Although the ideal way to study physical phenomena is the experimental approach, this is not always achievable. It is not possible, for example, to gain direct experimental access to most astrophysical systems. It is also still very difficult to reproduce astrophysical conditions in controlled laboratory conditions. In the same way, some systems can be too complex or nonlinear, and involve large number of degrees of freedom. This make them unsuitable also for a theoretical approach involving analytical methods. Under such circumstances, the development of tools allowing scientists to perform numerical simulations has been of prime importance. The latest developments in supercomputer (SC) construction allowing access to a unprecedented computational capability, has seen a great advancement in the potential of the computer modelling of the physical systems.

For this investigation, the particle-in-cell (PIC) numerical method has been used. In particular, a variant of THISMPI (**T**wo-and-a-**H**alf-D**i**mensional **S**tanford code with **M**essage **P**assing **I**nterface) code has been adapted, which is a modified version of the relativistic electromagnetic PIC code TRISTAN (Three-Dimensional Stanford code) [Buneman, 1993] with Message Passing Interface (MPI)-based parallelisation [Niemiec et al., 2008]. In this Chapter the PIC method is shortly introduced based mainly on the algorithms implemented in the THISMPI code.

5.1 Modelling the plasma: a kinetic description

The choice of the plasma modelling technique depends on the accuracy required in the study. For an investigation of a large-scale plasma system, the most used setup is the *fluid (Magneto-HydroDynamical, MHD)* description. In this technique, electrons and ions are treated as fluids, and their motion is described by fluid equations, based on macroscopic quantities. This model is inapt to describe the system micro-physics.

A *hybrid* description treats electrons as a fluid, but follows ions as single particles. It is therefore appropriate for the study of ion-scale physics. However, it is clearly unable to describe processes that occurs at the electron scales.

A *kinetic* model follows the full particle motions by solving the Vlasov equation, which contains self-consistent collective electromagnetic fields. It is a scheme

appropriate to investigate the micro-physics in the plasma, especially phenomena like particle acceleration and interactions with waves.

The Vlasov equation describes the evolution of the particle distribution function, $f = f(\mathbf{x},\ \mathbf{p}, t)$, in the self-consistent electromagnetic fields generated by the particles themselves. In this equation

$$\frac{\partial f_i}{\partial t} + \mathbf{v} \cdot \frac{\partial f_i}{\partial \mathbf{x}} + q_i(\mathbf{E}(\mathbf{x},\ t) + \mathbf{v} \times \mathbf{B}(\mathbf{x},\ t)) \cdot \frac{\partial f_i}{\partial \mathbf{p}} = 0, \tag{5.1}$$

index i represents particle species, $\mathbf{v} = \mathbf{v}(p)$ is the particle velocity $\mathbf{p}$ is the relativistic particle momentum and q is the electric charge. The evolution of the fields is given by Maxwell's equations:

$$\begin{aligned} \nabla \cdot \mathbf{E} &= \frac{\rho}{\epsilon_0}, \\ \nabla \cdot \mathbf{B} &= 0, \\ \nabla \times \mathbf{E} &= -\frac{\partial \mathbf{B}}{\partial t}, \\ \nabla \times \mathbf{B} &= \frac{1}{c}\frac{\partial \mathbf{E}}{\partial t} + \mu_0 \mathbf{j}, \end{aligned} \tag{5.2}$$

where ρ is the electric charge density and $\mathbf{j}$ is the electric current, defined as:

$$\begin{aligned} \rho(\mathbf{x},\ t) &= \sum_i q_i \int f_i(\mathbf{x},\ \mathbf{v},\ t)\ d^3\mathbf{v} \\ \mathbf{j}(\mathbf{x},\ t) &= \sum_i q_i \int f(\mathbf{x}, \mathbf{v}, t)\ \mathbf{v}\ d^3\mathbf{v}. \end{aligned} \tag{5.3}$$

Direct numerical solution of the Vlasov equation is possible, though computationally expensive and usually limited to small-scale systems. A far more convenient method is offered by the PIC model. This technique of solving the Vlasov equation employs the *method of characteristics* [Filbet et al., 2001]: we look for solutions that satisfy $\frac{d}{dt} f(\mathbf{x}\ (t), \mathbf{v}\ (t), t) = 0$, where $(\mathbf{x}\ (t), \mathbf{v}\ (t))$ is itself a solution of the system

$$\begin{aligned} \frac{d\mathbf{p}}{dt} &= F(\mathbf{x}\ (t), t), \\ \frac{d\mathbf{x}}{dt} &= \mathbf{v}\ (t). \end{aligned} \tag{5.4}$$

In the plasma case, $F(\mathbf{x}(t), t)$ is the Lorenz force, both generated by other particles and due to the self-consistent fields. So, the first equation in 5.4 becomes:

$$\frac{d\gamma m\mathbf{v}}{dt} = q(\mathbf{E} + \mathbf{v} \times \mathbf{B}), \tag{5.5}$$

where the sum on the index k involves all the fields. If the initial positions and velocities of the particles are known, as well as the external fields, it is possible to follow the evolution of the system only by solving Eq.s 5.4 and 5.5.

5.2 The Particle-In-Cell Method

The PIC method has been used since the 1950s [e.g., Harlow, 1956, Buneman, 1959, Yee, 1966, Okuda, 1972, Dawson, 1983, Langdon, 1985, Birdsall and Langdon, 1991]). It implements the following features to facilitate the computations:

1. The use of *discretisation*: the electromagnetic fields, electric charges and currents are discretised on a spatial grid, while particles can have arbitrary positions on the grid. Forces acting on particles are calculating by interpolation of the fields from the grid points to particle positions, using finite-difference methods. Quantities are also discretised in time. In this way, the dependence between the number of arithmetic operations N is *linear*. It therefore requires considerably less computational resources than a direct kinetic approach, that would involve calculations of interactions between all particles and N^2 arithmetic operations.

2. The *reduction of mass ratio*, m_i/m_e: in real plasma, processes acting on the ion or the electron scales are separated by a large spatial and temporal gap. This gap is often too large for computational resources, and it becomes convenient to compress the dynamical ranges by reducing the ion-to-electron mass ratio. The scale of the reduction needs to be chosen depending on the system under study, so that both the electron- and ion-scale processes can correctly reproduce the plasma behaviour, and a reasonable consumption of computational resources is achieved.

3. The definition of macroparticles: since investigating the plasma processes requires a very large number of particles, macroparticles are used instead. They represent many real particles, and since the Lorentz force depends only on the charge-to-mass ratio, a macroparticle will follow the same trajectory as a real particle would, provided that this ratio is preserved. This allows to save computational resources, while at the same time the physics of the system is not affected.

4. The *finite-size particle approach*: the macroparticles have a geometrical shape of "clouds" with a finite radius. This occurs naturally when we operate on a grid. For a radius which is comparable or larger than the Debye length, binary collisions cross section and frequency decrease much faster than for the point particles, making the finite-size particles approach very apt to describe collisionless plasma.

A PIC code computational cycle that solves the system of Eq.s 5.2, 5.3, 5.4 and 5.5 is made of four stages for every time-step, represented in schematic way in Figure 5.1. At first, the code integrates the relativistic particle equations of motion (5.5) under Lorentz force and advances particles to new positions (5.4). Secondly, equation 5.3 is discretised, and charges or currents are calculated by weighting particle contributions to appropriate grid locations. Thirdly, Maxwell's equations (5.2) are integrated on the grid. Fourthly, the new magnetic and electric fields are interpolated to new particle positions and new forces are calculated. At this point the cycle is finished, and a new cycle starts from the first stage.

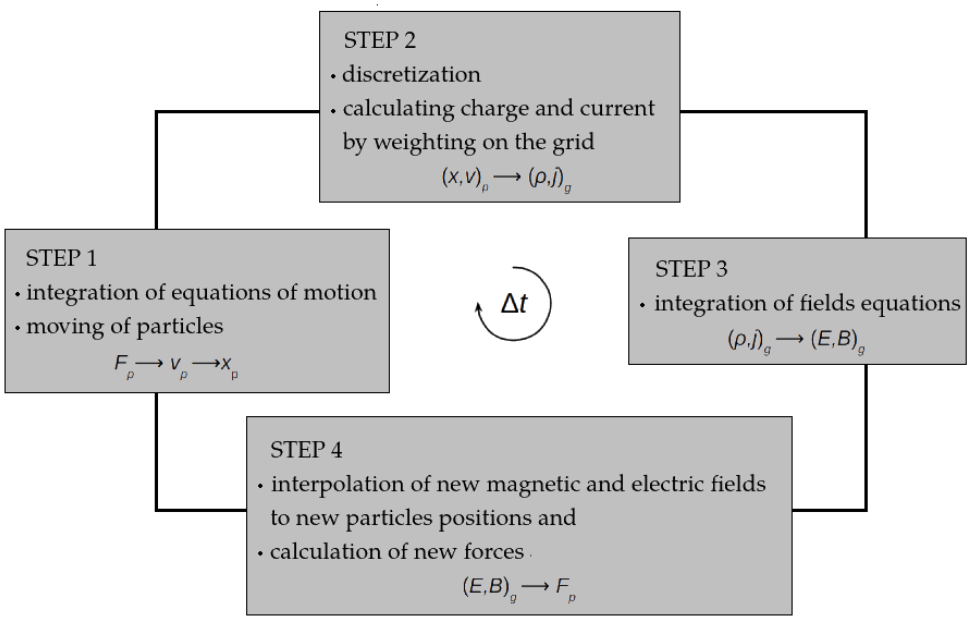

Figure 5.1: *The four stages of a a computational cycle in a PIC simulation program. Index p refers to particles, while the g index is related to grid points.*

Below, the basic algorithms implemented in the THISMPI code are shortly described. The presentation is not complete, as details can be found in, e.g., Buneman [1993]. The introduction here serves mainly as a basis to describe the code extensions necessary to perform simulations of mildly relativistic shocks.

5.2.1 Integration of particle equations of motion

The most commonly used integration scheme for particle equations of motion in PIC codes is the *leapfrog* method [Birdsall and Langdon, 1991]. This method is very efficient in terms of number of arithmetic operations and has a second-order calculation accuracy. A characteristic of the leapfrog method is that particle positions and forces acting on a particle are defined at full-integer time steps, $n\Delta t$, while particle velocities are calculated at half-integer time steps, $(n+1/2)\Delta t$ (see Figure 5.2).

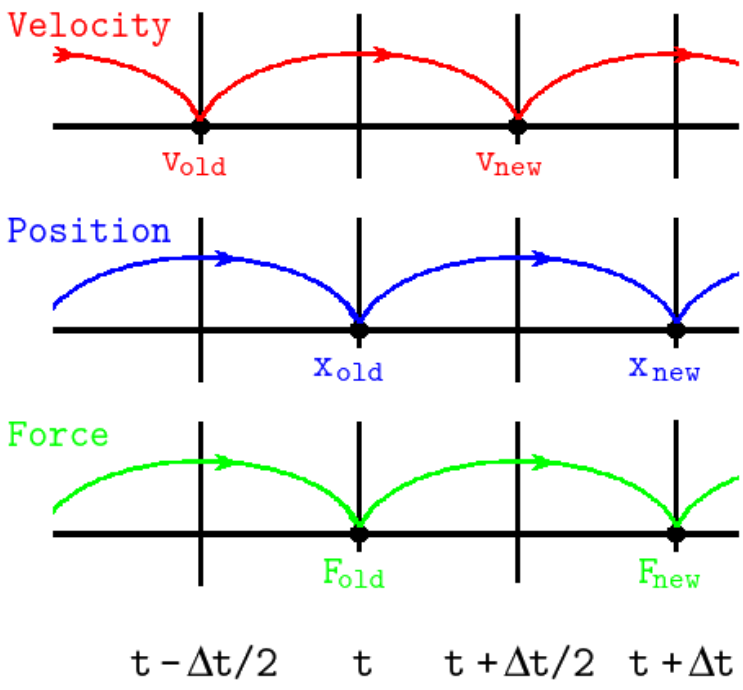

Figure 5.2: *Graphical representation of the leapfrog method for the discretization of equations of motion. Particle positions and forces acting on particles are defined at full-integer time steps, $n\Delta t$, while particle velocities are calculated at half-integer time steps, $(n+1/2)\Delta t$.*

The discretization of equations of motion 5.4 in the leapfrog scheme can be done in the following way:

$$\begin{aligned} m\frac{\mathbf{v}^{n+1/2}-\mathbf{v}^{n-1/2}}{\Delta t} &= \mathbf{F}(\mathbf{x}^{n}), \\ \frac{\mathbf{x}^{n+1}-\mathbf{x}^{n}}{\Delta t} &= \mathbf{v}^{n+1/2}, \end{aligned} \tag{5.6}$$

where, for simplicity, the formulas are given in the non relativistic limit, where the particle Lorentz factor $\gamma \to 1$. In this form the scheme is explicit and centred in time. It also allows to keep the particle position and velocity data only for a single time-step and then overwrite it for the next time-step. In this wave the integration method

does not require large RAM memory. For this reason, the leapfrog method is the best compromise between computational accuracy and the limited computational resources.

The integration of Eq. 5.5 with the Lorentz force is more complicated than the advancement of particle positions. Since the fields are calculated at integer time-steps, we need a formula to calculate the velocity at the same time-step $n\Delta t$. A discretization by finite-difference scheme of 5.5 (now in its relativistic formulation) yields :

$$m\,\frac{\gamma^{\,n+1/2}\,\mathbf{v}^{\,n+1/2}-\gamma^{\,n-1/2}\,\mathbf{v}^{\,n-1/2}}{\Delta t}=q(\mathbf{E}^{\,n}+\mathbf{v}^{\,n}\times\mathbf{B}^{\,n}). \tag{5.7}$$

The velocity $\mathbf{v}^{\,n}$ must be defined from velocities calculated at half-integer points, $\mathbf{v}^{\,n+1/2}$ and $\mathbf{v}^{\,n-1/2}$. The THISMPI code uses a solution proposed in Vay [2008]. With

$$\mathbf{v}^{\,n}=\frac{\mathbf{v}^{\,n+1/2}+\mathbf{v}^{\,n-1/2}}{2}, \tag{5.8}$$

Eq. 5.7 can be solved by defining a new quantities $\mathbf{u}\;=\;\gamma\,\mathbf{v}$, $\gamma^{\,n+1/2}=\sqrt{1+(u^{\,n+1/2}/c)^2}$, and

$$\mathbf{u}'=\mathbf{u}^{\,n-1/2}+\frac{q\Delta t}{m}\left(\mathbf{E}^{\,n}+\frac{\mathbf{v}^{\,n-1/2}}{2}\times\mathbf{B}^{\,n}\right). \tag{5.9}$$

In this way, $u^{\,n+1/2}$ and $\gamma^{\,n+1/2}$ at half-integer time steps are defined as:

$$\mathbf{u}^{\,n+1/2}=s\left(\mathbf{u}'+\left(\mathbf{u}'\cdot\frac{\tau}{\gamma^{\,n+1/2}}\right)\frac{\tau}{\gamma^{\,n+1/2}}+\mathbf{u}'\times\frac{\tau}{\gamma^{\,n+1/2}}\right) \tag{5.10}$$

and

$$\gamma^{\,n+1/2}=\sqrt{\frac{\zeta+\sqrt{\zeta^2+4(\tau^2+u^{*\,2})}}{2}}, \tag{5.11}$$

where $s=1/(1=t^2)$, $\tau=(q\Delta t/2m)\mathbf{B}^{\,n}$, $u^*=\mathbf{u}'\cdot\tau$ and $\zeta=(1+\mathbf{u}'/c^2)-\tau^2$. Hence, the value of $\mathbf{u}^{\,n}$ at the integer time-step is given by:

$$\mathbf{u}^{\,n}=\mathbf{u}^{\,n-1/2}+\frac{q\Delta t}{2m}(\mathbf{E}^{\,n}+\mathbf{v}^{\,n-1/2}\times\mathbf{B}^{\,n}). \tag{5.12}$$

5.2.2 Integration of Maxwell's equations and current deposition

In most PIC simulations electromagnetic fields are computed using the finite-difference time-domain (FDTD) method first introduced by Yee [Yee, 1966]. The Yee method is a very simple and robust tool for electromagnetic simulation, and the most

popular technique for the solution of differential equations. The method employs a cubic lattice of cells to approximate Maxwell's curl equations, as shown in Fig. 5.3. A grid point in space is defined as $(i,\ j,\ k) = (i\Delta x,\ j\Delta y,\ k\Delta z)$. Fig. 5.3 shows Yee computational grid for $\Delta x = \Delta y = \Delta z = 1$.

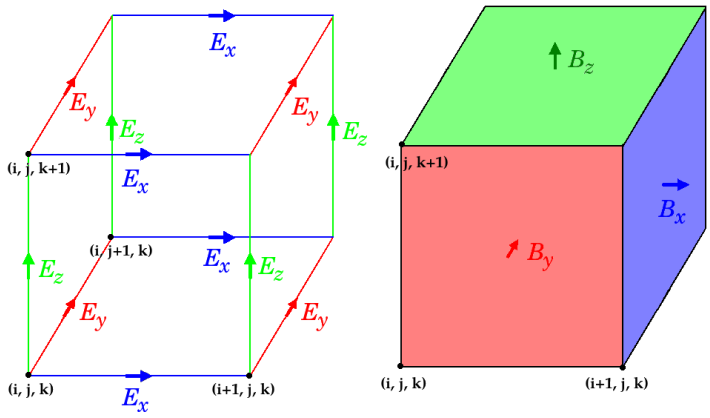

Figure 5.3: *Representation of the positions of electric and magnetic field components in Yee lattice: electric field components are defined at mid-cell edges, and the magnetic field at mid-cell surfaces*

In the Yee scheme the electric field components are defined at mid-cell edges, and the magnetic field at mid-cell surfaces, i.e.,

$$\begin{aligned} E_x\,(i,j,k) &\rightarrow E_x\,(i+0.5,j,k) \\ E_y\,(i,j,k) &\rightarrow E_y\,(i,j+0.5,k) \\ E_z\,(i,j,k) &\rightarrow E_z\,(i,j,k+0.5) \end{aligned} \tag{5.13}$$

for the electric field components, and

$$\begin{aligned} B_x\,(i,j,k) &\rightarrow B_x\,(i,j+0.5,k+0.5), \\ B_y\,(i,j,k) &\rightarrow B_y\,(i+0.5,j,k+0.5), \\ B_z\,(i,j,k) &\rightarrow B_z\,(i+0.5,j+0.5,k), \end{aligned} \tag{5.14}$$

for the magnetic field components. For the electric currents the same convention as for the electric field is used, and charge density is defined on nodes of the lattice. This staggered definition of quantities ensures that the change of **B** flux through a cell surface equals the negative circulation of **E** around that surface, and the change of **E** flux

through a cell surface equals the circulation of **B** around that surface minus the current through it. This helps in simplifying the discretization of the Maxwell's equations.

The THISMPI code uses the last two Maxwell's equations 5.2 to calculate the electric and the magnetic fields ($\epsilon_0 = 1$, $\mu_0 = 1/c^2$):

$$\frac{\partial \mathbf{E}}{\partial t} = c\,\nabla \times \mathbf{B} - \mathbf{j}, \tag{5.15}$$

$$\frac{\partial \mathbf{B}}{\partial t} = -\,c\,\nabla \times \mathbf{E}. \tag{5.16}$$

Time-centred discretization of these equations on the Yee lattice gives:

$$\left(\frac{\partial \mathbf{E}}{\partial t}\right)^{n+1/2} = \frac{\mathbf{E}^{\,n+1} - \mathbf{E}^{\,n}}{\Delta t} = c\,(\nabla \times \mathbf{B})^{\,n+1/2} - \mathbf{j}^{\,n+1/2}, \tag{5.17}$$

$$\left(\frac{\partial \mathbf{B}}{\partial t}\right)^{n} = \frac{\mathbf{B}^{\,n+1/2} - \mathbf{E}^{\,n-1/2}}{\Delta t} = c\,(\nabla \times \mathbf{E})^{\,n}. \tag{5.18}$$

Here the leapfrog scheme is applied, in which **E** is the quantity defined every integer time step, while **B** and **j** are defined at every half-integer time-step. In the 2D implementation the scheme thus gives for the magnetic field pusher ($\Delta t = 1$):

$$\begin{aligned}
B_x^{\text{new}}(i,\,j) &= B_x^{\text{old}}(i,\,j) + c\,(E_z^{\text{old}}(i,\,j) - E_z^{\text{old}}(i,\,j+1)),\\
B_y^{\text{new}}(i,\,j) &= B_y^{\text{old}}(i,\,) + c\,(E_z^{\text{old}}(i+1,\,j) - E_z^{\text{old}}(i,\,j)),\\
B_z^{\text{new}}(i,\,j) &= B_z^{\text{old}}(i,\,j) + c\,(E_y^{\text{old}}(i,\,) - E_y^{\text{old}}(i+1,\,j) + E_x^{\text{old}}(i,\,j+1) - E_x^{\text{old}}(i,\,j)),
\end{aligned} \tag{5.19}$$

and for the electric field pusher:

$$\begin{aligned}
E_x^{\text{new}}(i,j) &= E_x^{\text{old}}(i,j) + c\,(B_z^{\text{old}}(i,j) - B_z^{\text{old}}(i,j-1)) - j_x^{\text{old}}(i,\,j)\\
E_y^{\text{new}}(i,j) &= E_y^{\text{old}}(i,j) + c\,(B_z^{\text{old}}(i-1,j) - B_z^{\text{old}}(i,j)) - j_y^{\text{old}}(i,\,j),\\
E_z^{\text{new}}(i,j) &= E_z^{\text{old}}(i,j) + c\,(B_y^{\text{old}}(i,j) - B_y^{\text{old}}(i-1,j) + B_x^{\text{old}}(i,j-1) - B_x^{\text{old}}(i,j)) - j_z^{\text{old}}(i,\,j).
\end{aligned} \tag{5.20}$$

The remaining Maxwell's equations are solved implicitly. Taking time derivative of the second equation 5.2, we have (again, $\epsilon_0 = 1$, $\mu_0 = 1/c^2$):

$$\frac{\partial}{\partial t}(\nabla \cdot \mathbf{B}) = \nabla \cdot \frac{\partial \mathbf{B}}{\partial t} = -\,c\,\nabla \cdot (\nabla \times \mathbf{E}), \tag{5.21}$$

which means that if initially $\nabla \cdot \mathbf{B} = 0$, then it will always stay equivalent to zero during the simulation. For the same operation on the first equation we obtain:

$$\frac{\partial}{\partial t}(\nabla \cdot \mathbf{E} - \rho) = \nabla \cdot \mathbf{j} - \frac{\partial \rho}{\partial t}. \tag{5.22}$$

This equation expresses the charge conservation that must be rigorously fulfilled to satisfy the Poisson's equation. In the THISMPI code, the zigzag scheme developed by Umeda et al. [2003] is used for charge-conserving current deposition. This method is very accurate and computationally very efficient.

5.2.3 The CFL condition

When we use discretization of space and time variables (necessary for numerical simulations) we must remember a caveat: if the grid spacing or the time step is too large, the numerical stability of the calculations can be severely impaired. We have then to derive a threshold that guarantees the stability of our integration scheme.

Let us consider a physical quantity, $A(x,t) = A_0\, e^{ikx - i\omega t}$. Applying the space-centred discretization scheme that we use for the leapfrog method we obtain:

$$\begin{aligned} \frac{\partial A}{\partial x} &= \frac{\Delta A(x,t)}{\Delta x} = \frac{A(x_0 + \Delta x/2, t) - A(x_0 - \Delta x/2, t)}{\Delta x} = \\ &= \frac{e^{ik\Delta x/2} - e^{-ik\Delta x/2}}{\Delta x} A_0(x_0,t) = i \frac{\sin(k\Delta x/2)}{\Delta x/2} A_0(x_0,t) = i\, K\, A_0(x_0,t), \end{aligned} \tag{5.23}$$

where $K = \frac{\sin(k\Delta x/2)}{\Delta x/2}$. In the same way, we can perform a time-centred discretization:

$$\begin{aligned} \frac{\partial A}{\partial t} &= \frac{\Delta A(x,t)}{\Delta t} = \frac{A(x, t_0 + \Delta t/2) - A(x, t_0 - \Delta t/2)}{\Delta t} = \\ &= \frac{e^{-i\omega\Delta t/2} - e^{i\omega\Delta t/2}}{\Delta t} A_0(x_0,t) = -i \frac{\sin(\omega\Delta t/2)}{\Delta t/2} A_0(x_0,t) = i\, \Omega\, A_0(x_0,t), \end{aligned} \tag{5.24}$$

where $\Omega = \frac{\sin(\omega\Delta t/2)}{\Delta t/2}$. Hence, the dispersion equation for an electromagnetic wave on our grid will be $\Omega^2 = c^2 K^2$, and inserting the values for Ω and K we have:

$$\left(\frac{\sin(\omega\Delta t/2)}{c\Delta t}\right)^2 = \sum_{a=x,y,z} \left(\frac{\sin(k_a \Delta a/2)}{\Delta a}\right)^2. \tag{5.25}$$

A condition to have a real ω (and thus no instability development) is:

$$1 > (c\Delta t)^2 \sum_{a=x,y,z} \left(\frac{1}{\Delta a^2}\right) \tag{5.26}$$

If the grid has cubic cells (i.e. $(\Delta x = \Delta y = \Delta z)$ the condition becomes:

$$c\sqrt{D} < \frac{\Delta x}{\Delta t}, \tag{5.27}$$

where D is the number of dimensions. Eq. 5.27 is known as the Courant-Friedrichs - Lewy (CFL) condition [Courant et al., 1928]. When this condition is violated, ω becomes complex, and nonphysical growth of waves occurs.

The simulations performed for this thesis use 2D computational boxes, so the CFL condition is $c < (1/\sqrt{2})\Delta x/\Delta t \sim 0.7\Delta x/\Delta t$. For the assumed $\Delta_x = \Delta_y = 1$ and $\Delta t = 1$, we set $c = 0.5$, which satisfies the CFL condition.

5.3 Numerical techniques for reducing the noise

Since any physical quantity in our simulations is discretized on the grid, it follows that we cannot resolve scales which are smaller that the grid size. This causes Fourier power spectra of spatial quantities to present non-physical modes called *aliases*. When aliases interact with the physical modes the physics can be disturbed, producing nonphysical instabilities, numerical noise, and spurious forces. It is then necessary to devise some numerical techniques to decrease the influence of aliases and reduce the numerical noise.

Since statistical noise decreases as $N_{pcc}^{-1/2}$ (where N_{pcc} is the number of particles per cell) a first basic method to damp numerical noise is the use of large N_{pcc}. However, this method is not always exploitable, since it makes the simulation computationally heavier. Higher-order computational schemes for integration of field equations, e.g., the fourth-order integration instead of the second order one, can be used to provide further damping of the noise (see Section 5.5). Also higher-order interpolation methods for calculations of physical quantities that use higher-order particle shape factors (see Section 5.3.1) can be implemented. On top of these additional digital noise filtering methods can be implemented.

5.3.1 Particle shape

It was already mentioned that PIC simulations make use of finite-size macroparticles, i.e. "clouds" of plasma particles. The choice of the macroparticle shape depends on the required order of approximation. The charge weights which should be assigned to appropriate grid points are defined by the *particle shape function*.

The simplest particle shape is the zero-order approximation (Figure 5.4, panel 1), and the corresponding shape function is defined as:

$$S_1(x) = \begin{cases} 1, & \frac{x-x_p}{\Delta x} < \frac{1}{2} \\ \frac{1}{2}, & \frac{x-x_p}{\Delta x} = \frac{1}{2} \\ 0, & \frac{x-x_p}{\Delta x} > \frac{1}{2} \end{cases} . \tag{5.28}$$

Here, x is the discretized position coordinate along the grid, and x_p is a particle position. In this way every particle is assigned to the nearest grid point. However, this particle shape function produces a high computational noise.

The first-order approximation is the so-called cloud-in-cell (CIC) model (Figure 5.4, panel 2). In this setup the electric charge of the particle is shared between two adjacent grid points, and the weights linearly depend on the particle position relative to the grid points. The shape function for the CIC model is:

$$S_2(x) = \begin{cases} 1 - \frac{x-x_p}{\Delta x}, & \frac{x-x_p}{\Delta x} \leq 1 \\ 0, & \frac{x-x_p}{\Delta x} > 1 \end{cases} . \tag{5.29}$$

This method presents a higher accuracy, but is more computationally expensive, because each particle shares its charge into two grid points in 1D case and the four grid points in the 2D case.

Even more higher accuracy is obtained by implementing a second-order approximation, the triangular-shape-cloud (TSC) (Figure 5.4, panel 3). The macroparticles have a triangular shape and particle charge is assigned to three grid points in 1D case and nine grid points in 2D case. The shape function in this case is:

$$S_3(x) = \begin{cases} \frac{3}{4} - \left(\frac{x-x_p}{\Delta x}\right)^2, & 0 \le \frac{x-x_p}{\Delta x} \le \frac{1}{2} \\ \frac{1}{2}\left(\frac{3}{2} - \left(\frac{x-x_p}{\Delta x}\right)\right)^2, & \frac{1}{2} \le \frac{x-x_p}{\Delta x} \le \frac{1}{2} \\ 0, & \frac{x-x_p}{\Delta x} > \frac{3}{2} \end{cases} . \tag{5.30}$$

This high-order particle shape functions is more computationally expensive. However, this model is very efficient in reducing the numerical noise in the simulations. This set-up in fact works like a low-pass filter, by cutting the highest frequencies in Fourier decomposition of integrated quantities [Umeda, 2004]. The TSC shape factors are used in the simulations presented in this thesis.

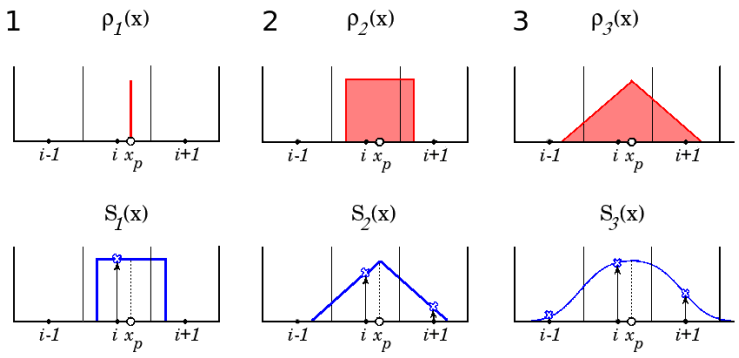

Figure 5.4: *Distributions of electric charge for particles (top) and corresponding shape functions (bottom) for zero-order approximation (panel 1), cloud-in-cell (CIC) approximation (panel 2), and triangular-shape-cloud (TSC) approximation (panel 3)*

5.3.2 Filtering

If the amount of available computational resources (CPU time, RAM memory) is limited, or the other techniques not efficient enough, additional noise filtering methods must be implemented to improve overall accuracy and reduce noise, in particular where finite difference algorithms for ∇ and ∇^2 become most inaccurate. In Fourier-based codes, which operate directly on the Fourier spectra of physical variables, one can simply use low-pass filters to cut high frequencies related to aliases. In the PIC codes, such as the THISMPI code, one cannot operate directly on the Fourier spectra of physical variables. For this reason, the filtering must be done in x space and methods of digital filtering must be used. The most commonly used filter in PIC simulation is the

binomial filter [Birdsall and Langdon, 1991]. Let the quantity to be filter to be defined as $A(x_i) \equiv A_i$, which is a periodic quantity and it is known at the grid points $x_i \equiv i\Delta x$. Applying a simple filter to A_i means substituting the physical quantity with its filtered counterpart, defined as:

$$A'_i = \frac{W\, A_{i-1} + A_i + W\, A_{i+1}}{1+2W}, \tag{5.31}$$

where W is the weight. In the Fourier space, the representation of this filter may be obtained by assuming that the Fourier transform of the original quantity, $A_i(k)$, is given by $\sum_{i=1}^{N} A(x_i)\, e^{ikx_i}$. Hence, the filtered quantity in the Fourier space is

$$A'_i(k) = \sum_{i=1}^{N} \frac{W\, A_{i-1} + A_i + W\, A_{i+1}}{1+2W}\, e^{ikx_i} \tag{5.32}$$

and defining $p = i-1$ and $q = i+1$ one gets for A'_i:

$$A'_i(k) = \frac{W\, \sum_{p=0}^{N-1} A(x_p)\, e^{ikx_{p+1}} + \sum_{i=1}^{N} A(x_i)\, e^{ikx_i} + \sum_{q=2}^{N+1} A(x_q)\, e^{ikx_{q-1}}}{1+2W} \tag{5.33}$$

Remembering now that A_i is periodic, i.e., the numbering of the grid points can start anywhere, one find the result

$$A'(k) = \frac{1+2W\cos(k\Delta x)}{1+2W} A(k) = S(k\Delta x)\, A(k) \tag{5.34}$$

where $S(k\Delta x)$ is the smoothing function. It can be noted that for $W > 0.5$ the smoothing function flips sign in the region $0 < k\Delta x < \pi$, which is an undesirable behaviour. For $W = 0.5$, the smoothing function is instead always positive, and it goes to zero quadratically as $k\Delta x$ approaches π. Application N times leads to filtering to order of $\cos^{2N}(k\Delta x)$, in analogy of what would be obtained from a single-pass filter with binomial coefficients [Birdsall and Langdon, 1991]. The filter with $W = 0.5$ is hence called the *binomial filter*.

A simple example of application of a binomial 2D filter is then:

$$A'(x_i, y_j) = A(x_j, y_j) \otimes \begin{pmatrix} 1 & 2 & 1 \\ 2 & 4 & 2 \\ 1 & 2 & 1 \end{pmatrix} \tag{5.35}$$

where $\otimes$ designates convolution of matrices. A binomial filter is applied in the code

used for this dissertation to the components of currents, which are the source terms in Maxwell's equations.

A severe source of noise in relativistic plasma simulations is the Cerenkov emission, caused by the fact that fields in PIC simulations are computed using FDTD method, which is affected by numerical phase error. In fact, on grid, the dispersion relation for electromagnetic waves is given by Eq. 5.25, while in contrast, electromagnetic waves in real space propagate according to:

$$\frac{\omega^2}{c^2} = k_x^2 + k_y^2 + k_z^2 = k^2 \ . \tag{5.36}$$

One can see that the numerical dispersion relation (Eq. 5.25) approximates equation 5.36 only at low frequencies (where $\sin x \sim x$). The numerical wave propagation speed at high frequencies is slower than the physical wave propagation speed. If relativistic particles are in a simulation, their velocities are close to c and may exceed the numerical wave propagation speed at high frequencies. This results in the appearance of non-physical numerical Cerenkov radiation fields that may significantly disturb the system and for this reason they must be eliminated.

Among the methods that can be used to efficiently damp the numerical Cerenkov emission [see, e.g., Greenwood et al., 2004] is the Friedman filter [Rambo et al., 1989, Friedman, 1990]. It uses the standard Yee update equation for the electric fields presented Eq. 5.17, while the magnetic field pusher in Eq.5.18 is augmented to take the form:

$$\mathbf{B}^{\,n+1/2} = \mathbf{B}^{\,n-1/2} - \Delta t \nabla \times \left[\left(1 + \frac{\theta_f}{2}\right) \mathbf{E}^{\,n} - \theta_f \left(1 - \frac{\theta_f}{2}\right) \mathbf{E}^{\,n-1} + \frac{1}{2}(1-\theta_f)^2 \, \theta_f \, \mathbf{E}^{\,n-2} \right] . \tag{5.37}$$

Here, the parameter θ_f is introduced that sets the strength of the filter in a range $0 \leq \theta_f \leq 1$, and $\mathbf{E}^{\,n-2} = \mathbf{E}^{\,n-2} + \theta_f \, \mathbf{E}^{\,n-3}$. The standard fields updating (equations 5.17 and 5.18) is recovered for $\theta_f = 0$. It seems that a compromise between an efficient suppression of the Cerenkov nonphysical modes and the need to guarantee that the physics of the phenomena to be studied is not affected is achieved for $\theta_f = 0.05$ [Greenwood et al., 2004]. Through test simulations it was verified that this is true also for the parameters of the simulations performed for this thesis (see Section5.4).

Therefore, here I set $\theta_f = 0.05$.

5.3.3 Fourth-order field pusher

Another solution to damp the numerical noise, especially nonphysical Cerenkov radiation, is the alteration of the computational stencil. This requires changing the approximation to the spatial derivatives for the FDTD method [Greenwood et al., 2004]. The Yee method uses second-order centred finite differences. A higher-order approximation takes more values around the point of interest, as illustrated in Figure 5.5.

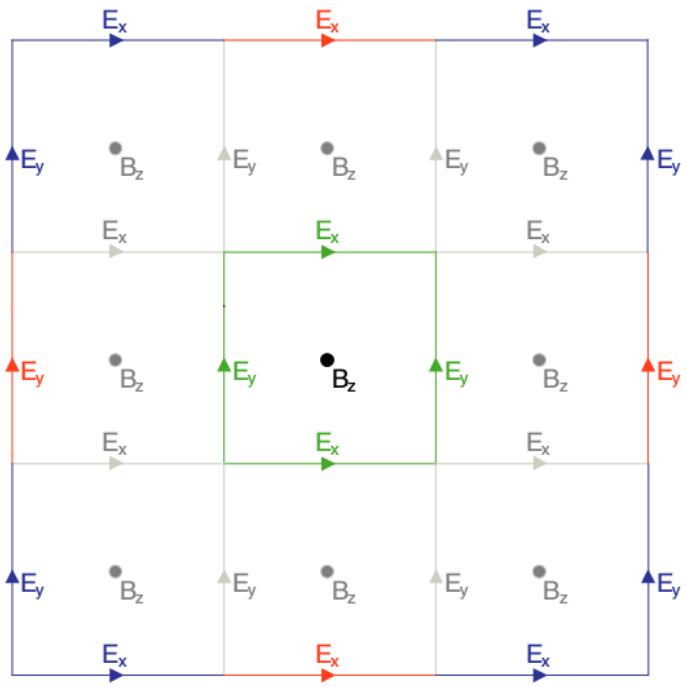

Figure 5.5: *Fourth-order approximation: the E_x and E_y values are used to compute $\nabla \times \mathbf{E}$ to update B_z. The standard Yee FDTD scheme uses the values shown in green. The values shown in red and blue are used in addition to the values shown in green.*

In the fourth-order approximation we can calculate $\nabla \times \mathbf{E}$, necessary to update the B_z-field at a point located in the centre in Figure 5.5, in three ways. First, with the values showed in green (Yee standard scheme) give:

$$\begin{aligned} B^z(i,j,k) &= \hat{z} \cdot (\nabla \times \mathbf{E})_{(i+1/2,j+1/2,k)} \\ &= \frac{E^y_{(i+1,j+1/2,k)} - E^x_{(i+1/2,j+1,k)} - E^y_{(i,j+1/2,k)} + E^x_{(i+1/2,j,k)}}{\Delta} + O(\Delta^2) \,, \end{aligned} \tag{5.38}$$

where again a notation $A_{(i,j,k)}$ indicates a quantity evaluated at the position ($i\Delta x$, $j\Delta y$,

$i\Delta z$) on the grid, and we assume $\Delta x = \Delta y = \Delta z = \Delta$. A second way is to approximate the curl by using the values shown in red:

$$B^z(i,j,k) = \frac{E^y_{(i+2,j+1/2,k)} - E^x_{(i+1/2,j+2,k)} - E^y_{(i-1,j+1/2,k)} + E^x_{(i+1/2,j-1,k)}}{3\Delta} + O(\Delta^2)\,, \tag{5.39}$$

and the third one is to use the values shown in blue:

$$\begin{aligned} B^z(i,j,k) = \frac{1}{6\Delta}\Big(&E^y_{(i+2,j-1/2,k)} + E^y_{(i+2,j+3/2,k)} - E^x_{(i+3/2,j+2,k)} - E^x_{(i-1/2,j+2,k)} \\ &- E^y_{(i-1,j+3/2,k)} - E^y_{(i-1,j-1/2,k)} + E^x_{(i-1/2,j-1,k)} + E^x_{(i+3/2,j-1,k)}\Big) + O(\Delta^2)\,. \end{aligned} \tag{5.40}$$

Each of these approximations is second-order accurate. Hence, a linear combination of them is also second-order accurate. We can then approximate the curl as $B_z = K_1$ Eq.5.39 + K_2 Eq. 5.40 + $(1 - K_1 - K_1)$ Eq. 5.38, where K_a are weight factors [Hadi and Picket-May, 1997]. The case with $K_1 = K_2 = 0$ recovers the standard Yee FDTD scheme. The fourth order accurate approximation is recovered with $K_1 = -1/8$, and $K_2 = 0$ [Cangellaris and Lee, 1992]. It has been shown how in this configuration even relativistic particle do not excede the numerical light propagation speed for most time-steps, Δt [Greenwood et al., 2004]. Moreover, this $K_1 - K_2$ combination provides the largest maximum stable time-step among the configurations that effectively damp the nonphysical Cerenkov radiation. For these reasons, this fourth-order accurate field-pusher is incorporated in the THATMPI code used for my simulations. A series of preliminary tests allowed us to determine that in order to suppress efficiently nonphysical Cerenkov radiation in our simulation setup the use of the fourth order approximation is necessary.

5.4 Code stability tests

In order to assess the stability of our configuration against numerical instabilities several tests have been performed. They are summarised here and parameters of the most representative tests are listed in Table 5.1. For the tests we put an electron-ion plasma slab in 2D simulation box and allowed it to propagate freely with the flow Lorentz factor $\Gamma_0 = 2$ along the x-direction for time $t\omega_{pe} = 1000$. This time frame corresponds to the distance $(x - x_0) = 870\lambda_{se}$ travelled by the beam. We need the plasma to propagate unperturbed as far as possible to avoid any numerical instability to arise

before the plasma interacts with the shock or with upstream propagating waves. The box is periodic in all directions, which allows us to calculate the box-average quantities that characterise the system. The tests summarised here have been performed with the electron skin depth $\lambda_{se} = 10\Delta$ and ion-to-electron mass ratio $m_i/m_e = 50$.

Table 5.1: *Summary of the most representative stability tests. Investigated are the effects of the Friedman filter parameter θ_f, the fourth order field pusher, a different time step value, Δt, and the plasma upstream electron thermal velocity, $v_{e,th}$.*

	σ	θ_f	$v_{e,th}$	Field pusher	Δt
T1	0.0	0.05	0.01c	2-nd order	1.0
T2	0.0	0.05	0.01c	4-th order	1.0
T3	0.0	0.00	0.01c	4-th order	1.0
T4	0.0	0.05	0.01c	4-th order	0.5
T5	0.0	0.05	0.01c	4-th order	1.1
T6	0.1	0.05	0.01c	4-th order	1.0
T7	0.1	0.05	0.0	4-th order	1.0

A system with a plasma beam propagating in an empty space should be not different from the plasma system at rest, due to Lorentz invariance. However, numerical instabilities described above may significantly alter the system and in the extreme case even completely destroy the beam to the point of its isotropization. The most efficient in the beam destruction are the grid-Cerenkov effects, that develop very fast if damping numerical techniques are not implemented. In the tests I investigated the effect of the Friedman filter, the fourth order field pusher, different time steps, Δt, and the electron upstream thermal velocity, $v_{e,th}$. It must be noted that obtaining eternally stable configurations is not possible. I then look for a parameter set that enables us to keep the plasma stable for an appropriate time, to guarantee that in a final simulation any interaction with the shock will happen before nonphysical instabilities build up. Results for different tests are compared in Figure 5.6, in which I plot the beam velocity in the plasma rest frame. As noted, in a stable system, this velocity should be zero. Any significant bulk plasma motion in its original rest frame is thus a good proxy for the amplitude of the numerical instabilities in a numerical setup.

The first tests have been performed for unmagnetized plasma, runs T1-T5. One can see that models using the second-order field pusher, run T1, or no Friedman filtering, run T3, are highly unstable. On the other hand, the stability is ensured when applying the fourth-order field pusher and a Friedman filter with a parameter $\theta_f = 0.05$, run T2.

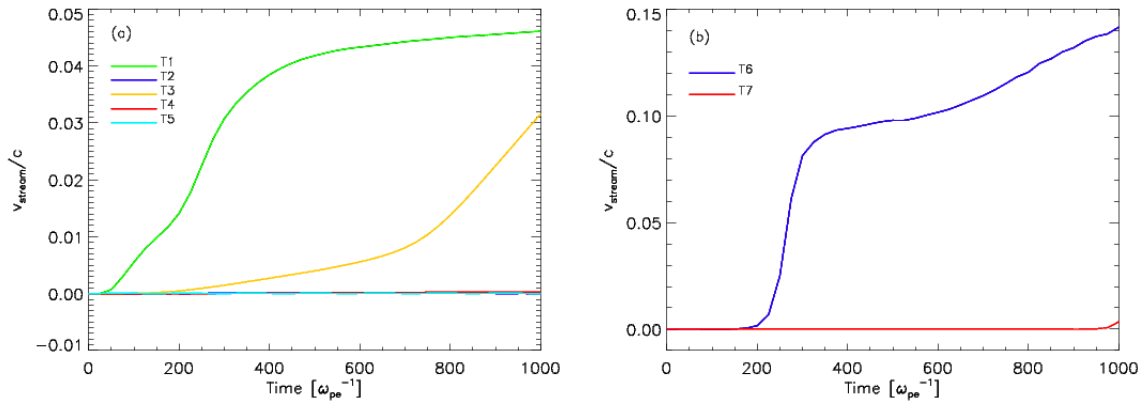

Figure 5.6: *Stream velocity in the plasma rest frame for the runs listed in Table 5.1. Test with an unmagnetized plasma are presented in panel (a), tests T1-T5, and the magnetized one in panel (b), tests T6-T7. In panel (a), the lines for tests T2, T4 and T5 overlap at zero.*

The stability of this model does not depend on the choice of the time-step, as verified for $\Delta t = 0.5$ (run T4) and $\Delta t = 1.1$ (run T5), results for which overlap in Figure 5.6a. Note that these time-steps are consistent with the CFL condition (see Section 5.2.3). The independence of the code stability on the time-step in our code is in contrast to the so-called implicit codes, for which a specific CFL number can be found that minimises the excitation of the numerical instabilities [e.g., Ikeya and Matsumoto, 2015].

In the second types of tests, the plasma carries a large-scale magnetic field perpendicular to the simulation plane, runs T6-T7. The strength of this field gives the plasma magnetization assumed in the production simulations. Run T6 uses the model proved to be stable for the unmagnetized beam. However, in the magnetized case, the Cerenkov radiation quickly sets in and destroys the beam. Run T6, as other test runs, T1-T5, assumed an almost cold beam with the electron mean thermal velocity $v_{e,th} = 0.01$ in the beam rest frame. Further tests showed that the beam stability in the magnetized beam could be assured only when applying the so-called *quiet start* method, in which $v_{e,th} = 0$. Results for run T7 in Figure 5.6b show that in this case the plasma is much more stable, although a small heating is present at the end of the run. However, in a shock simulation the beam interaction with the shock happens much earlier than the travel time allowed within time frame of $t\omega_{pe} = 1000\Delta t$. The stability is also improved at much higher resolution of $\lambda_{se} = 80\Delta$ used in the production runs. The T7 model can thus be safely applied to study magnetized mildly relativistic shocks.

CHAPTER 6
SIMULATIONS OF PERPENDICULAR SHOCKS

In this chapter I present results of my very-large-scale high-resolution 2D PIC simulations of mildly-relativistic shocks in the electron-ion plasma. I will demonstrate generation of electromagnetic precursor waves through SMI and production of wakefields in the shock upstream and discuss particle acceleration mechanisms upstream and downstream of the shock. I will investigate the effects of the shock rippling on the shock structure and particle energisation. Simulation setup is presented in Section 6.1, in which a rationale for performing very high-resolution studies is given in Section 6.1.1. The 2D simulations are performed for two configurations of the perpendicular mean magnetic field with respect to the simulation plane – the out-of-plane, with results presented in Section 6.2, and the in-plane, described in Section 6.4. For comparison, in Section 6.3 I also show results for a 1D simulation.

6.1 Simulation setup

As the computational cost of 3D PIC experiments is prohibitively high for the resolution required in my study, I restrain to 2D3V simulations that use two-dimensional spatial grid but follow three components of particle momenta and electromagnetic fields (a 2D3V model). The plasma beam lies in the $x-y$ plane. My simulations exploit the commonly used *reflective wall* setup, where a cold electron-ion beam is injected at the right side of the box to flow in the negative x-direction. Upon reflection off the conductive wall at the left side of the simulation box, the beam collides with the incoming flow to form a shock propagating in the positive x-direction. In order to suppress numerical Cerenkov radiation I implemented Friedman filtering with parameter θ_f and a fourth order accurate FTFD technique, as described in Section 5.3. The CFL condition is satisfied by $\Delta t = \Delta x = 1.0$, $c = 0.5$ and the plasma beam is totally cold, which is the most stable configuration as shown in Sec. 5.4. The beam carries a large-scale magnetic field $\mathbf{B_0}$ that is set to be perpendicular to the shock normal. I probe two values of the magnetic field inclination angle with respect to the simulation frame: $\varphi_B = 90^\circ$, in which the large scale magnetic field is perpendicular to simulation plane (the out-of-plane setup) and $\varphi_B = 0^\circ$, in which the magnetic filed lies in the simulation plane (the in-plane setup). Corresponding motional electric field

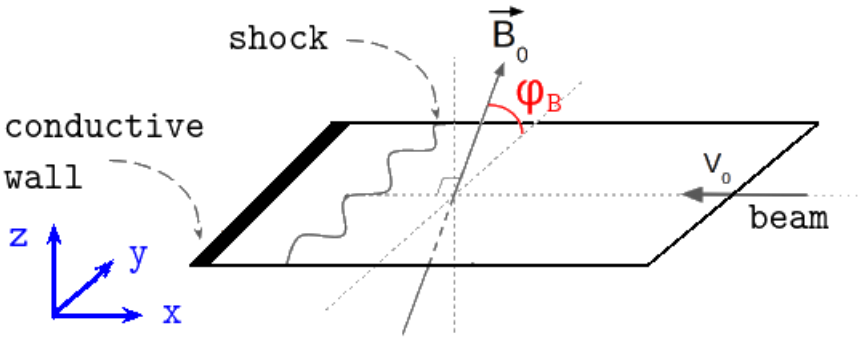

Figure 6.1: *Simulation setup for the simulations described in this dissertation: I make use of the reflective wall setup, in which the incoming beam collides with the conductive surface and is then reflected, thus forming a shock propagating backwards along the x-axis. The ambient magnetic field is perpendicular to the shock normal and forms the angle φ_B with the simulation plane.*

$\boldsymbol{E_0} = -\boldsymbol{v_0} \times \boldsymbol{B_0}$ is also initialised in the plasma, with the beam velocity $\boldsymbol{v_0}$. This motional field lies in the simulation plane ($\boldsymbol{E_0} = -E_y \hat{\boldsymbol{y}}$) in the out-of-plane setup and it points out of the simulation plane ($\boldsymbol{E_0} = E_z \hat{\boldsymbol{z}}$) in the in-plane magnetic field case. Note that due to different number of degrees of freedom (3 and 2 in the in-plane and the out-of-plane case, respectively) the shock physics may in general be different in the two models.

For the large-scale simulations the box has a transverse dimension of $L_y = 5760$ cells, and I used 10 particles per cell and per species. The use of such a large transverse box size is due to the necessity to fully resolve the features that develop in the shock surface and that have characteristic lengths of several λ_{si}. The lateral box size, L_x, expands in x-direction during simulations and reaches the final size of $L_x = 160000\Delta \simeq 283\lambda_{si}$ at $t_{\max}$. The unit of length used here is the ion skin depth, $\lambda_{si} = c/\omega_{\rm pi} = 566\Delta$. Both the value for λ_{si} and N_{ppc} are determined through the convergence tests described in Sec. 6.1.1. The box is then $\sim 10\lambda_{si}$ wide.

I probe a mildly relativistic regime, appropriate for the internal shock model of AGN jets, and I use the system parameters that are representative of the jet physics. The beam Lorentz factor is set to $\gamma_0 = 2.02$, so that the resulting Lorentz factor of the shock is $\Gamma_{sh} \simeq 2.2$ in the shock upstream rest frame. Furthermore, I assume a total plasma magnetization $\sigma = 0.1$, with

$$\sigma = \frac{B_0^2}{\mu_0 N_i (m_e + m_i) \gamma_0 c^2}, \tag{6.1}$$

where μ_0 is the permeability of free space, and the upstream quantities – magnetic field strength, B_0, and the ion density, N_i – are given in the simulation (shock downstream) frame [Hoshino et al., 1992]. With this definition, it follows that $1/\sigma = 1/\sigma_e + 1/\sigma_i$, where σ_e and σ_i are electron and ion magnetizations, respectively. I assumed a reduced ion-to-electron mass ratio of $m_i/m_e = 50$, to reduce the computational burden of my simulations. This mass ratio is large enough to separate electron and ion scales. Through test simulations I verified that our results do not change if a higher mass ratio of $m_i/m_e = 100$ is used. With $m_i/m_e = 50$ the electron magnetization is $\sigma_e = 5.2$. Time and all temporal dependencies is expressed in units of the ion cyclotron frequency $\Omega_{ci} = (eB_0)/(m_i\gamma_0)$. 2D simulations ran for a long time into the nonlinear phase, up to $t\Omega_{ci} = 84.3$ and complementary 1D simulation reaches $t_{\max} = 163.1\,\Omega_{ci}^{-1}$. The time-step I used is $\delta t = 1/1131\,\omega_{\rm pi}^{-1} = 1/3556.8\,\Omega_{ci}^{-1}$.

6.1.1 The need for high-resolution studies

The main problem with performing numerical simulations of shocks in plasma is the constraint by the available computational resources. Present-day simulations employ billions of computational particles but at the same time the size of the simulation grid and its resolution and a final simulation time must be properly chosen for the characteristic physical distances and frequencies of the problem under study. The inclusion of ions in PIC simulations constitutes a further challenge: in fact , if the simulated system is only composed by electrons and positrons with mass m_e, the characteristic time scale that must be resolved is typically $\omega_{pe}^{-1} \sim \sqrt{m_e}$, and it is possible to run a simulation for thousands of ω_{pe}^{-1} and analyse the system up to a strongly non-linear phase. However, studying protons in the simulations requires much longer time scales. In order to correctly capture the ion behaviour, a PIC simulation must resolve a good number of ion characteristic time scales, $\omega_{pi}^{-1} \sim \sqrt{m_i}$. If one were to perform a simulation for a realistic mass ratio $m_i/m_e \approx 1836$ this would correspond to running the simulation for a time interval that is $\sqrt{m_i/m_e} \approx 42$ times longer than for the case involving only leptons. The spatial scale also constitutes a problem, since ions require correspondingly larger spatial scales. It can be seen that in principle the simulation box size that is necessary to model electron-proton plasmas increases compared to that required by leptonic plasmas by a factor of $\sim \sqrt{D}$, where D is the number of spatial dimensions resolved by the code [Bret and Dieckmann, 2010]. For this reason PIC

simulations that use realistic electron-to-ion mass ratio are very unusual and mostly restricted to 1D regimes [e.g., Dieckmann et al., 2006] and to 2D simulations that need to resolve a very small spatio-temporal domain [e.g., Honda et al., 2000], while 2D PIC simulations that cover a large domain and 3D PIC simulations normally introduce reduced mass ratio of $16 \div 100$ (e.g. [e.g., Spitkovsky, 2007, Niemiec et al., 2008, Hoshino et al., 1992, Martins et al., 2009, Stockem et al., 2012, Iwamoto et al., 2019]). However, caution must always be exercised since some phenomena such as magnetic reconnection and Buneman instability have been shown to be influenced by the mass ratio [Guo and Lu, 2007, Bohdan et al., 2017].

A second, but very important factor is the simulation the space resolution, i.e., the number of simulation cells used to resolve electron and ion skin depths. High-frequency short-wavelength oscillations characteristic of, e.g., precursor waves emitted by the shock towards the upstream plasma may be easily damped out in case of insufficient resolution. Consequently, simulations which aim at investigating these kind of waves must set this parameter carefully. If, on one hand, applying a lower resolution eases the computational burden, on the other hand it may fully or partially suppress physical phenomena. Very low resolutions of $\lambda_{se} = 10\Delta x$ have been used in, e.g., Sironi and Spitkovsky [2011] and $\lambda_{se} \approx 2.3\Delta x$ in [Stockem et al., 2012]. Iwamoto et al. [2017] investigated the relation between the value of these simulation parameters and the numerical damping of the SMI shock-emitted waves by performing numerical convergence tests in N_{ppc} and the resolution. They observed that the precursor wave amplitude systematically increases with the resolution until the value at which a convergence is achieved, that occurs for $\lambda_{se} = 40\Delta x$ in their model. This proves that the precursor wave emission is very sensitive to numerical resolution. As the code used for my simulations is structured differently from the one in [Iwamoto et al., 2017], I performed my own set of test simulations, to find the appropriate simulation parameters.

I have performed two sets of test simulations for a numerical convergence study. In the first set I used 2D simulations with the setup the same as in our run with the out-of-plane magnetic field, $\varphi_{\mathrm{B}} = 90\circ$, and I probed different resolutions in terms of the electron skin depth values of $\lambda_{se} = 15\Delta$, 40Δ and 80Δ, and different number of particles per cell, $N_{\mathrm{ppc}} = 10, 20$ and 40. The transverse size of the numerical grid was

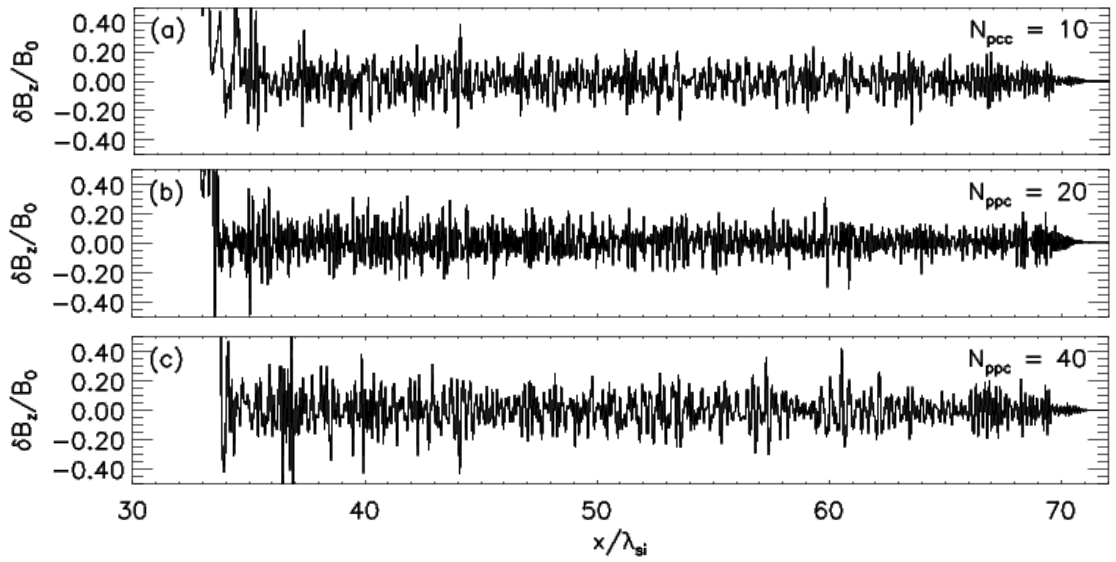

Figure 6.2: *Profiles of B_z magnetic field fluctuations upstream of the shock located at $x/\lambda_{si} \simeq 33$ at time $t\Omega_{ci} \simeq 22.5$ and different $N_{ppc} = 10$ (a), 20 (b) and 40 (c) for the 2D convergence tests. Profiles are taken in the middle of the box along $y/\lambda_{si} = 1.5$ and are normalised to the initial magnetic field strength. Here $\lambda_{se} = 15\Delta$.*

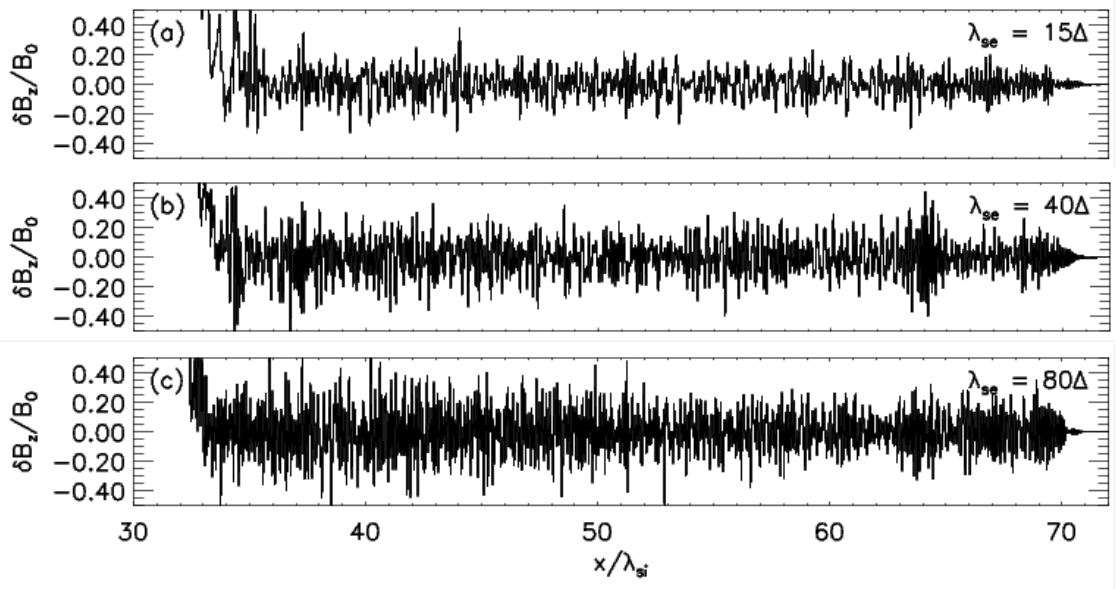

Figure 6.3: *Profiles of B_z magnetic field fluctuations upstream of the shock located at $x/\lambda_{si} \simeq 33$ at time $t\Omega_{ci} \simeq 22.5$ and different $\lambda_{se} = 15\Delta$ (a), 40Δ (b) and 80Δ (c) for the 2D convergence tests. Profiles are taken in the middle of the box along $y/\lambda_{si} = 1.5$ and are normalised to the initial magnetic field strength. Here $N_{ppc} = 10$.*

adjusted to have $L_y \simeq 3\lambda_{si}$ in each case. Figure 6.2 shows the profiles of B_z magnetic field fluctuations taken in the middle of the box along $y/\lambda_{si} = 1.5$ at time $t\Omega_{ci} \simeq 22.5$ for $\lambda_{se} = 15\Delta$ and different $N_{\rm ppc}$. Similarly, Figure 6.3 presents results for the case of $N_{\rm ppc} = 10$ and different λ_{se}. In Figure 6.4 we compare the normalised amplitudes of the waves at different λ_{se} and $N_{\rm ppc}$. The amplitudes are averaged in the region of $x/\lambda_{si} = 35 - 40$, located about $2\lambda_{si}$ from the shock. One can see that the number of particles per cell does not influence the amplitude of the precursor waves, and so that I choose $N_{\rm ppc} = 10$ for our 2D large-scale production runs. However, the amplitude increases with the electron skin depth.

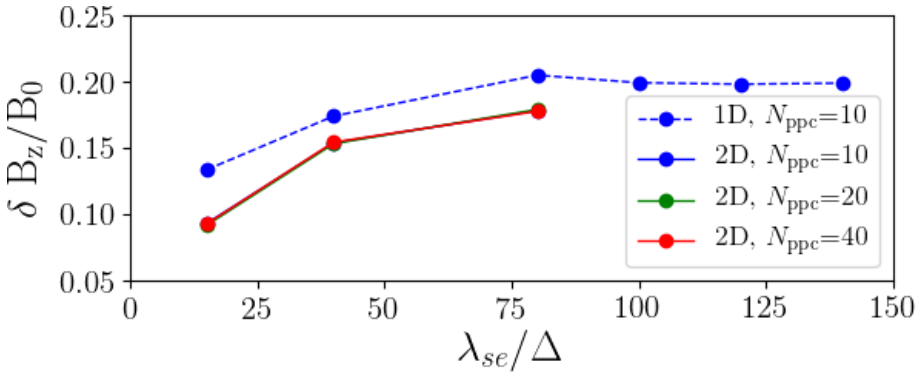

Figure 6.4: *Normalized amplitudes of δB_z at different λ_{se} and $N_{\rm ppc}$ obtained in 1D (blue dashed line) and 2D (solid blue, green, and red lines) convergence test runs. The amplitudes are calculated at $t\Omega_{ci} \simeq 22.5$ and are averaged in the region of $x/\lambda_{si} = 35 - 40$, located about $2\lambda_{si}$ from the shock (compare Fig. 6.19). Note that results for 2D tests and different $N_{\rm ppc}$ overlap.*

To verify whether $\delta B_z/B_0$ is saturated at the maximum resolution of $\lambda_{se} = 80\Delta$ tested with 2D simulations, we performed the second set of test runs with 1D simulations with the same λ_{se} and also extending the probed resolution range for the cases with $\lambda_{se} = 100\Delta$, 120Δ, and 140Δ. For 1D tests we take $N_{\rm ppc} = 10$ and use the 2D simulation code but with 5 cells in the y-direction, which is the minimum number of grid points in the transverse direction allowed in our code. 1D tests show that the convergence is indeed obtained for $\lambda_{se} = 80\Delta$, which is the value used in our production runs. Note that the amplitudes in 1D simulations are slightly larger than in 2D runs at the same skin depth because the shock has not yet reached a steady state (see discussion in Section 6.2.2(d) and compare Fig. 6.19).

6.2 Results for out-of-plane setup

In this section I describe the structure of a mildly relativistic strictly perpendicular shock in ion-electron plasma observed in the setup with the large-scale magnetic field pointing out of the simulation plane. I simulated up to $t_{\max}\Omega_{ci} = 84.3$. Differently from what has been observed for highly relativistic flows [e.g., Sironi and Spitkovsky, 2011, Iwamoto et al., 2019], the mildly relativistic shock is not laminar throughout the entire simulation but quickly develops corrugations in its surface. These shock rippling, visible in both density and electromagnetic field maps, start appearing at $t\Omega_{ci} \sim 6.5$, and fully unfold by $t\Omega_{ci} \sim 8.5$. In Sec. 6.2.1 I first present the structure of the laminar shock at $t\Omega_{ci} \simeq 7.5$ to demonstrate that the SMI is already operating at this early stage in line with theoretical expectations. In Sec. 6.2.2 I compare the laminar shock stage results with the nonlinear physics of fully-evolved rippled shock.

6.2.1 Laminar shock stage

The shock structure in the initial stages of my simulations ($t\Omega_{ci} = 7.5$) is shown in Fig. 6.5. The shock front is located at $x/\lambda_{si} \sim 11$. The density increase in the downstream is averaging around ~ 3, consistent with the value of $R = 2.83$ derived from Eq. 3.23 in Sec. 3.2.1. The last two panels of Fig. 6.5 show details of the upstream region of the shock.

The features in B_z are fully compatible with those in E_y, hence E_y map is not showed here. The shock front is located at $x \simeq 11\lambda_{si}$. Upstream of the shock, at $x \gtrsim 12\lambda_{si}$, one can see plane-wave fluctuations in B_z magnetic field (see 2D map of $\delta B_z = B_z - B_0$ in Fig. 6.5c and transversely-averaged profile in Fig. 6.5e), that move with the speed of light away from the shock (i.e., their wave vector is along positive x, $\mathbf{k}_{\mathrm{Bz}} = k_x\hat{\mathbf{x}}$). They are polarised in the z-direction, parallel to the large-scale magnetic field. The associated fluctuations in E_y are transverse both to the mean magnetic field and to the propagation wave vector. These waves are then *electromagnetic* waves of the X-mode type. In the shock upstream one can also see longer-wavelength longitudinal fluctuations in E_x electric field (Figs. 6.5b and 6.5d) with $\boldsymbol{k}_{\mathrm{Ex}} = k_x\hat{\boldsymbol{x}}$ and moving also with the speed of light. The normalised amplitude of these *electrostatic* waves averaged over the three oscillations observed, $E_y/B_0c \simeq 1.8 \cdot 10^{-2}$, is an order of amplitude smaller than the X-mode waves amplitude. Note that already in this very early stage of the simulation the shock surface

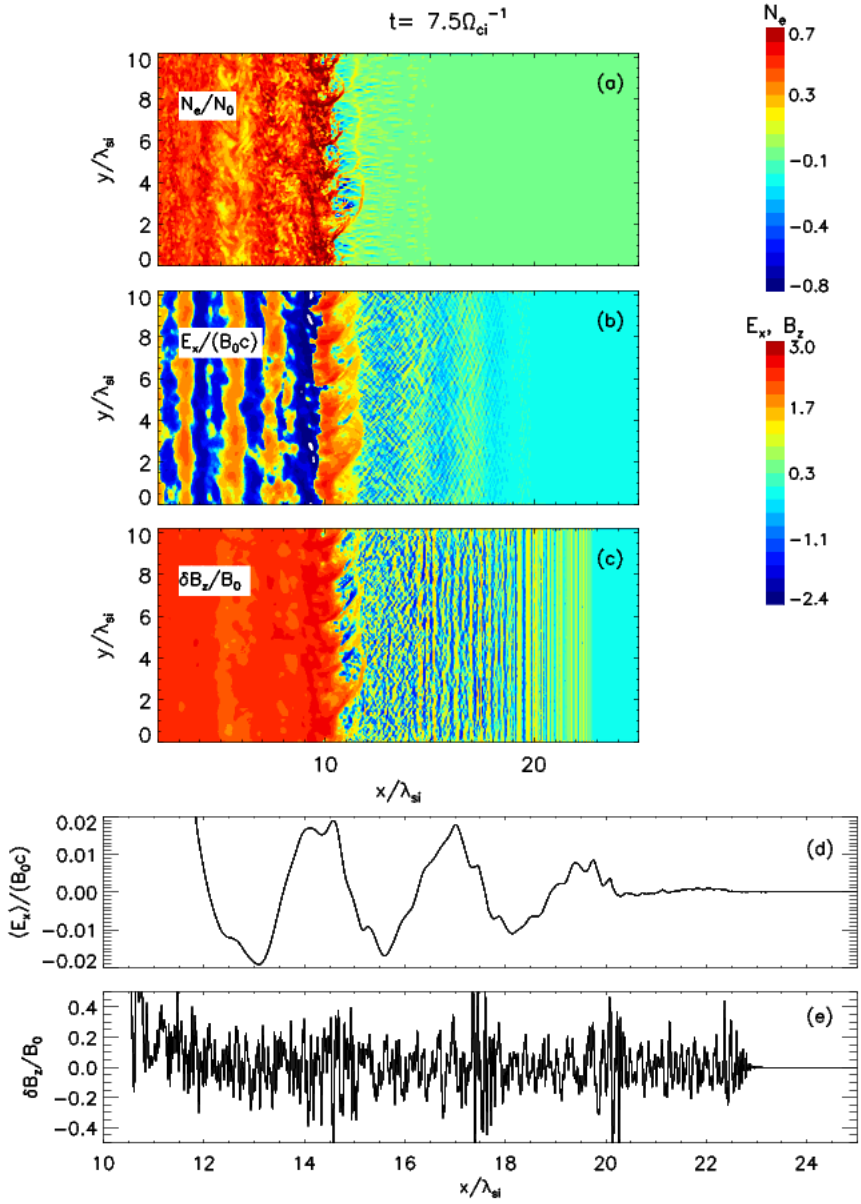

Figure 6.5: *Distribution of the normalised electron number density* N_e/N_0 *(a) and the structure of* E_x *electric field (b) and turbulent* B_z *magnetic field (c) components at time* $t\Omega_{ci} = 7.5$*. Logarithmic scaling is applied to the density map. The scaling for electromagnetic fields is also logarithmic, but sign-preserving (e.g.,* $\mathrm{sgn}(B_z) \cdot \{2 + \log[\max(|B_z|/B_0, 10^{-2})]\}$*), so that field amplitudes below* $10^{-2}B_0$ *are not resolved. Field amplitudes are normalised to the initial magnetic field strength. Panel (d) shows transversely averaged profile of the electric field,* $\langle E_x \rangle$*, upstream of the shock, and panel (e) the profile of* δB_z *taken in the middle of the box along* $y/\lambda_{si} = 6$*.*

is perturbed by the developing shock-front ripples.

The emission of X-mode polarised electromagnetic waves from the shock towards the upstream region is a signature of SMI [e.g., Hoshino, 2008, Iwamoto et al., 2017, 2018]. Linear dispersion relation for this waves for parameters used in this study is

presented in Sec. 4.1. Direct comparison with the linear theory will be discussed in the following sections, since the limited extension of the shock precursor at this early stage restricts the dynamic range of wave-vectors. However, here I demonstrate that the waves observed in the precursor of my mildly relativistic shock have been generated through the SMI mechanism by analysing the wave power spectrum, shown for the oscillations in B_z in Fig. 6.6a. I choose the region upstream of the shock at $x/\lambda_{si} = 13-18$ (see Fig. 6.5). The waves emitted immediately after the beam reflection off the conducting wall and now localised in the $x/\lambda_{si} \sim 20-23$ region are heavily affected by the initial conditions and hence are not considered in this analysis.

One can see in the spectra that the waves are mostly parallel with $k_{\mathrm{Bz,x}}/\lambda_{si} \simeq 10-20$, though a weak oblique component is also present. The wave spectrum has a cutoff at lower wave-numbers and the wave power is mostly to the right of the white solid line. This line represents an estimate of the theoretical cutoff wavenumber. This cutoff represents the minimum wave number above which the waves can propagate upstream ahead of the shock. It expresses the requirement that the upstream-directed group velocity of the precursor waves is larger than the shock velocity. To estimate this wavenumber, one can start from the the X-mode waves dispersion relation in the upstream, Eq. 4.32:

$$\eta'^2 = \epsilon_{yy} \rightarrow \frac{c^2\, k'^2}{\omega'^2} = 1 - \frac{\omega_{pe}^2}{\omega'^2 - \Omega_{ce}^2}. \tag{6.2}$$

Here and in the following, upstream rest frame quantities are denoted with prime. In the upstream plasma rest frame, the wavenumber is $k' = k_x$. One observes that if $\omega' \gg \omega_{pe}$ we retrieve the dispersion relation in a weekly magnetized plasma, $\omega'^2 = k'^2c^2 + \omega_{pe}^2$. In case of $\omega' \rightarrow \infty$ the dispersion relation tends to the one for a wave in vacuum $\omega'^2 = k'^2c^2$. Considering that $\Omega_{ce}^2 = \omega_{pe}^2\sigma^2$ and by performing a Lorentz transformation one obtains the dispersion relation in the simulation rest frame:

$$\frac{\omega^2}{\omega_{pe}^2} = \frac{\sigma}{\gamma^2(1+\beta\ \eta\ cos\theta)} + \frac{1}{1-\eta^2}\ . \tag{6.3}$$

As we consider precursor waves propagating towards the upstream, $-\pi/2 < \theta < \pi/2$ is the angle between the $x-$axis and the wave propagation direction. One observes that, in the first term on the right hand side $(1 + \beta\eta\cos\theta)$ is always equal or greater than

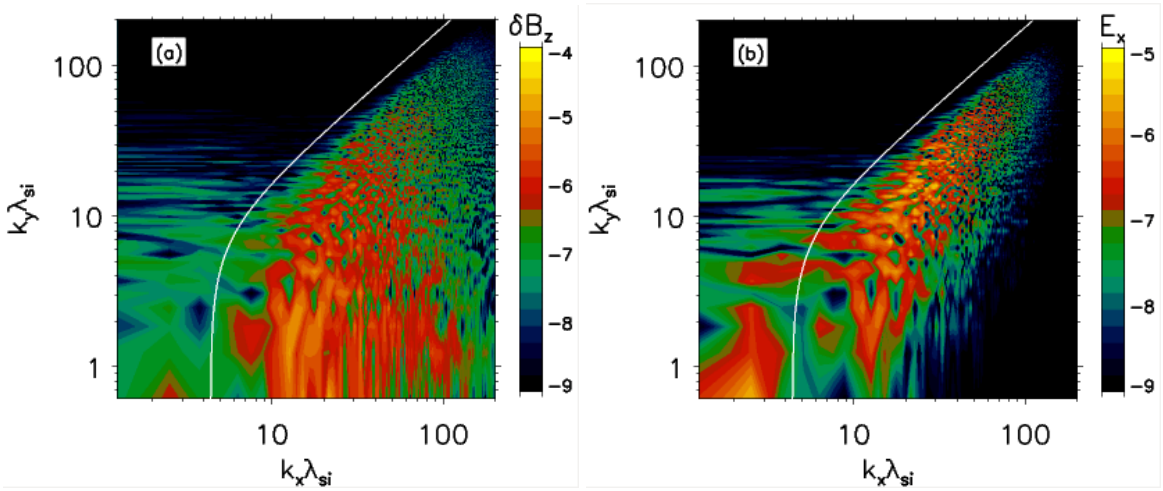

Figure 6.6: *Fourier power spectra for B_z field fluctuations and E_x in the early stage of the shock evolution, $t = 7.5\Omega_{ci}^{-1}$, calculated upstream of the shock in the region $x/\lambda_{si} = (13-18)$ (compare Fig. 6.5). The solid white line represents the precursor wave theoretical cutoff wavenumber.*

unity. I then estimate the maximum contribution to the dispersion relation by this term as σ/γ^2, and the dispersion relation in its approximated form can be written:

$$\frac{\omega^2}{\omega_{pe}^2} \approx \frac{\sigma}{\gamma^2} + \frac{1}{1-\eta^2}. \tag{6.4}$$

This gives

$$\omega \approx \sqrt{(1+\frac{\sigma}{\gamma^2})\omega_{pe}^2 + c^2k^2}, \tag{6.5}$$

where the terms in the fourth power of $\omega_{\rm pe}$ were discarded. The waves group velocity is then:

$$v_{\rm gr} = \frac{\partial\omega}{\partial k} = \frac{c^2k}{\sqrt{(1+\frac{\sigma}{\gamma^2})\omega_{pe}^2 + c^2k^2}}. \tag{6.6}$$

From the group velocity one can estimate the cutoff wavenumber for the precursor waves propagating in the upstream. Equating the $x-$component of the wave group velocity $v_{gr,x} = v_{gr}\cos\theta$ with the shock velocity, $c\beta_{\rm sh}$ one obtains:

$$k_x = \beta_{\rm sh}\Gamma_{sh}\sqrt{(1+\frac{\sigma}{\gamma^2})\frac{\omega_{pe}^2}{c^2} + k_y^2}. \tag{6.7}$$

To calculate the theoretical cutoff wavenumber I used the shock velocities measured from the simulations.

In the magnetized electron-proton plasma the interaction of the precursor waves

with the upstream medium should lead to the generation of electrostatic fluctuations, so-called wake-field. Fig. 6.6b shows the Fourier power spectrum of E_x in the same upstream region that was selected to obtain Fig. 6.6a. Parallel component (with $k_y \approx 0$) is clearly present at $k_{\mathrm{Ex},x}\lambda_{si} \simeq 2.5-3.0$. Higher-intensity oblique spectral component at $k_x \gtrsim 4$ also exists for E_x. As discussed in the next section, these waves are electromagnetic SMI-induced modes generated at oblique angles due to the shock ripples already emerging at this stage. The signal at $k_x\lambda_{si} \sim 1-4$ and $k_y\lambda_{si} \sim 3-20$ is due to upstream filamentation and is described in detail in Sec. 6.2.2(c).

The wavelength of the waves in the E_x component propagating in the $x-$direction can be inferred from Fig. 6.6 to be $\lambda_{Ex} \sim 3.2\lambda_{si}$. Under the assumption that wake-field waves are generated via Raman scattering, it is expected that if in the upstream frame the frequency of the electromagnetic pump wave is larger than ω_{pe}, then for the Langmuir wave $\omega'_L \simeq \omega_{pe}$, and $k'_L \simeq 1/\lambda_{se}$ [Kruer, 1988, Hoshino, 2008], This condition is met in our simulation, since the frequencies of the precursor waves $\omega'/\Omega_{ce} \gtrsim 1$ and $\Omega_{ce}/\omega_{pe} \simeq 2.25$ (see Sec.4.1). After performing the Lorentz transformation we obtain the wavenumber, k_L, of the electrostatic waves in the downstream (simulation) frame:

$$\begin{aligned} k_L =& \gamma_0\, k'_L\, (1-\beta\, \frac{\omega'_L}{c\, k'_L}) \simeq \gamma_0\, \frac{1}{\lambda_{se}}(1-\beta\, \frac{\omega_{pe}\, \lambda_{se}}{c}) \\ =& \frac{\gamma_0}{\lambda_{si}}\, \sqrt{\frac{m_i}{m_e}}\, (1-\beta). \end{aligned} \tag{6.8}$$

For our parameters, this gives the theoretical wavenumber $k_{\mathrm{Ex}}\lambda_{si} \simeq 1.86$, corresponding to the wavelength of $\lambda_{\mathrm{Ex}} \simeq 3.4\lambda_{si}$. A slight discrepancy with the observed signal is due to a coarse sampling for the wavenumbers allowed by a limited extension of the precursor wave region at this stage (compare Fig. 6.5). A better agreement is observed in the later stage (see Fig. 6.11b in Sec. 6.2.2(b), in which the Fourier spectra are calculated in a region of double width.

6.2.2 Nonlinear Shock Structure

Fig. 6.7 shows the map of the B_z magnetic field fluctuations at time $t\Omega_{ci} = 56.2$ in the region extending from near the shock to the far upstream. For this stage I analysed the properties of the precursor waves and compare them with the linear theory in Fig. 6.8. Fig. 6.9 shows the full shock structure and the shock region structure respectively, at

the final stage of my simulation at $t\Omega_{ci} = 84.3$.

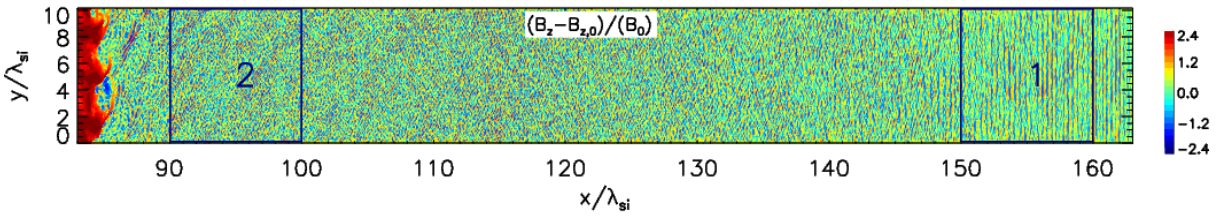

Figure 6.7: *Map of the normalised B_z magnetic field fluctuations, δB_z, at time $t\Omega_{ci} = 56.2$. The shock is located at $x/\lambda_{si} \simeq 84$ and waves beyond $x/\lambda_{si} \gtrsim 162$ resulting from the initial transient are not shown. Logarithmic scaling is applied (see Fig. 6.5). Regions 1 and 2 highlighted with blue squares for $x/\lambda_{si} = 150 - 160$ and $x/\lambda_{si} = 90 - 100$, respectively, mark the initial positions of the regions chosen for the Fourier analysis of the waves presented in Fig. 6.8. Note that the colour scale is saturated at the shock to enhance the visibility of the precursor waves.*

6.2.2(a) Precursor Waves

As one can see in Fig. 6.7, far upstream from the shock, from $x/\lambda_{si} \gtrsim 148$, the precursor waves retain their plane-wave character. Closer to the shock, the structure of the waves changes and they acquire an oblique component. Near the shock and up to $x/\lambda_{si} \sim 120$ (see also Fig. 6.9) the waves form a quasi-regular pattern of stripes of oblique waves of modulated amplitude. This feature is related to the ripples in the shock surface. However, the waves in the whole precursor (both oblique and plane) are extraordinary electromagnetic waves generated through SMI, as in the linear stage discussed in Sec. 6.2.1. To verify this, I performed the Fourier analysis in the frequency-wavevector domain of the waves in two selected regions of the shock precursor. The regions are fixed in the upstream plasma rest frame, and they move in the simulation frame with the appropriate speed. Their location at the initial time-step of my analysis is framed with square boxes in Fig. 6.7. The regions move towards the shock, and by the last time step of the analysis they covered a distance of $\approx 1.5\lambda_{si}$.

The Fourier-Laplace power spectra shown in Fig. 6.8 are calculated from quantities in the upstream plasma rest frame, which facilitates a direct comparison with the theoretical dispersion relation discussed in Sec. 4.1, but at the same time does not permit a direct visual comparison with Fig. 6.6. The theoretical dispersion relation is overlaid in the plots with white dots. To derive the spectra, I selected a region in the shock upstream which is at rest in the upstream plasma frame. For every time step, I then perform the Lorentz transformation of the field map from corresponding region

in the simulation frame and subtract the background magnetic field component. Then I perform Fourier-Laplace analysis to investigate the evolution in time of a 1D profile of the waves taken in a selected range of x along $y = 5\lambda_{si}$. The time frame of $2000\delta t$ used for the calculations is between $t\Omega_{ci} \simeq 56.23$ and 56.79, that corresponds to $\sim 28.1\,\Omega_{ce}^{-1}$. The field data is stored every 10 time steps, so that the maximum frequency resolved is $\omega_{\max} = \pi/(10\delta t) \simeq 22.3\,\Omega_{ce}$. The limited time span of our analysis does not allow us to resolve the low frequency modes of SMI generated by ions. However, as discussed in Sec. 4.1, I do not expect to observe the ion-induced SMI, as the emission by ions is mostly subluminous.

The Fourier power spectrum of the waves in *Region 1* at $x/\lambda_{si} = 150 - 160$ is shown in Fig. 6.8a. This region includes the plane-waves with $k \approx k_x$ analysed in Sec. 6.2.1 that travelled with a speed close to the speed of light towards upstream and have been identified with the electron SMI-generated modes. The observed signal matches very well the theoretical dispersion relation for the electron SMI. In particular, the wave power is mostly along the light mode, $\omega = kc$, and a few first harmonic modes exist for a wide range of wave vectors. The power spectrum in *Region 2* at $x/\lambda_{si} = 87 - 97$ presented in Fig. 6.8b is calculated only for the k_x component of the waves. The spectrum in this region is heavily influenced by the the effects of the shock rippling and

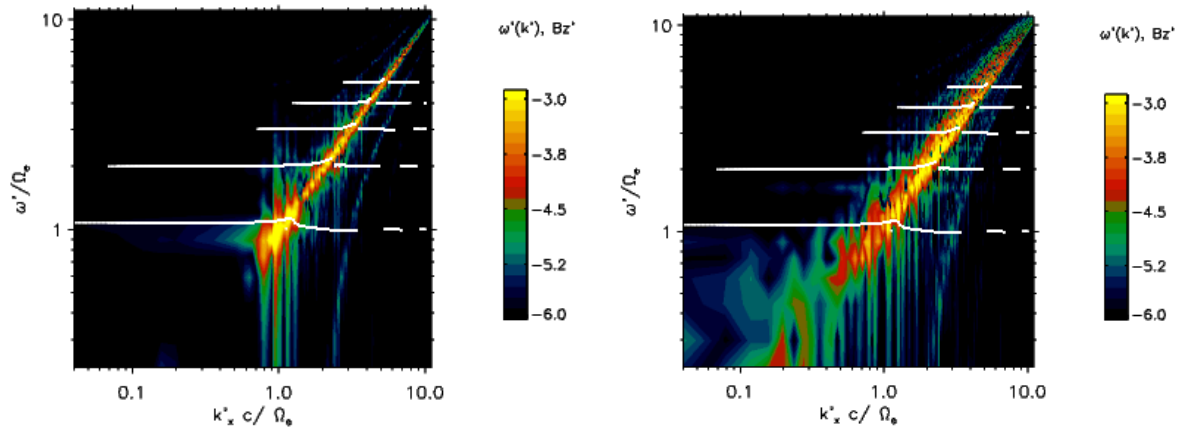

(a) *Region 1* **(b)** *Region 2*

Figure 6.8: *Fourier power spectrum of B_z magnetic field oscillations in $\omega - k_x$ space taken along $y = 5\lambda_{si}$ in Regions 1 and 2 marked in Fig. 6.7. The time interval is $0.562\,\Omega_{ci}^{-1} \simeq 28.1\,\Omega_{ce}^{-1}$, starting from time $t\Omega_{ci} \simeq 56.23$. The analysis is performed in the* upstream *plasma rest frame. The angular frequency, ω, is normalized with the electron cyclotron frequency, Ω_{ce}, and the wavevector, k_x, by Ω_{ce}/c. Overlaid with white dots is the theoretical dispersion relation derived from the linear analysis presented in Sec. 4.1.*

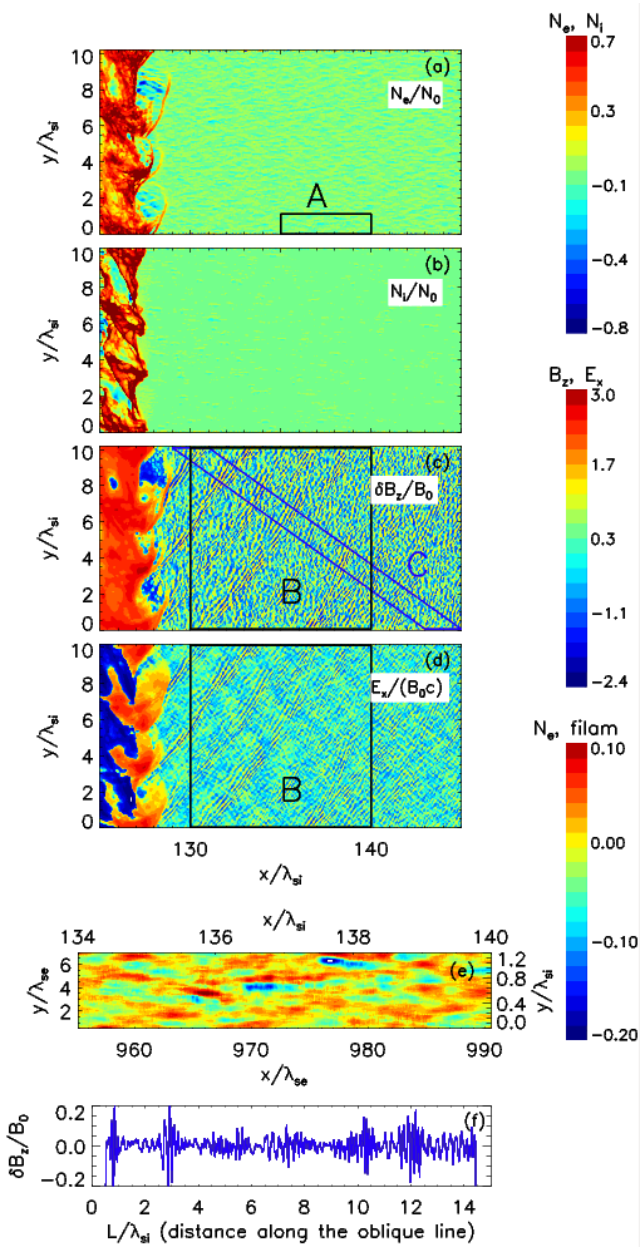

Figure 6.9: *Distribution of the normalised electron number density (a), ion density (b), B_z magnetic field fluctuations, δB_z (c), and E_x electric field (d) at the final stage of the simulation, $t\Omega_{ci} = 84.3$. Logarithmic scalings are applied to density and field maps (see Fig. 6.5). Panel (e) shows a close-up of Region A in the electron density plot (a). The axes show scales in units of both the ion, λ_{si}, and the electron, λ_{se}, skin depth. Region B marked with squares in panels (c) and (d) for $x/\lambda_{si} = 130 - 140$ is chosen for the Fourier analysis of the waves presented in Fig. 6.11. Region C marked with a blue parallelogram in panel (c) is chosen to plot the averaged and smoothed profile of B_z precursor waves shown in panel (f), in which the distance along the oblique direction is given in units of λ_{si} with an arbitrary starting point.*

also by the nonlinear evolution of the wave modes, as in particular can be noted in the low frequency and wavenumber part of the plot. Nevertheless, the spectrum retains its qualitative agreement with the theory of the electron SMI.

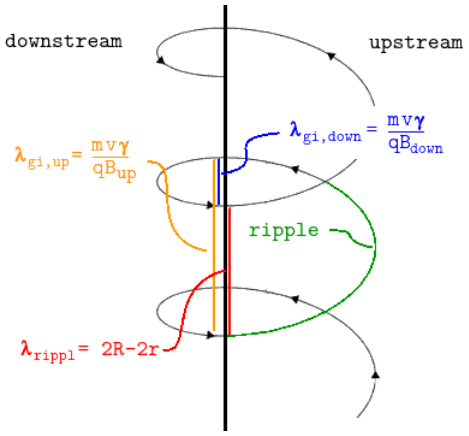

Figure 6.10: *Scheme of the derivation of the ripple scale lenght L as a function of the upstream and downstream ion gyroradii (R and r respectively).*

6.2.2(b) Effects of Shock Rippling on the Waves

The shock front ripples are visible in Figs. 6.7 and 6.9 through correlated fluctuations in density and all electromagnetic field components. They propagate along the $-y$-direction with an average velocity consistent with the velocity of reflected ions gyrating at the shock. Their observed mean wavelength along the shock surface, $\lambda_{\rm rippl} \approx 3.3\lambda_{si}$, fits a scale of a double of the cumulative ion gyro-radius, $\lambda_{gi,\,rippl} = \lambda_{gi,\,up} - \lambda_{gi,\,down} \approx 1.7\lambda_{si}$, as shown in Fig. 6.10. This supports the interpretation that the origin of the rippling is in the instability resulting from a modulation of shock-reflected ions along the shock surface [Burgess and Scholer, 2007], as described in Sec. 3.3.1.

In my simulation of a mildly relativistic magnetized shock with out-of-plane magnetic field configuration the shock surface ripples grow quickly from small-scale fluctuations to a long-wave mode visible in Figs. 6.7 and 6.9. However, their structure is highly dynamic on timescales shorter than Ω_{ci}^{-1}. As one can see in Fig. 6.9, the wavelength of the mode is determined by the modulation in the ion density, but its structure is given by the effects of the magnetic field compression and charge-separation induced because of different inertia of electrons and ions. These effects shape the ripples to a form of arcs of increased magnetic field and electron density and associated electric fields. As evidenced in the maps of the B_z and E_x field components in Figs. 6.9c-d, these arcs are apparently related to the observed pattern of oblique waves.

The oblique structure of the precursor waves can be understood to result from a combination of two effects – relativistic aberration of light and precursor wave emission

in a direction normal to a local tangent to the surface of the ripplings' arcs. The velocity of the ripples along the negative y-direction is $v_{rippl} \approx 0.8c$, close to the speed of light. The emitted radiation is then affected by the relativistic aberration, i.e., the angle between the wave propagation and the source velocity in the observer (simulation) frame is given by:

$$\cos\vartheta = \frac{\cos\vartheta' - \frac{v}{c}}{1 - \frac{v}{c}\cos\vartheta'}, \tag{6.9}$$

where v is the source velocity in the observer frame and ϑ' is the angle between the source direction of motion and the wave-vector of the emitted waves in the source rest frame. If a wave is emitted along the x-axis in the ripple frame of reference (i.e., $\vartheta' = 90°$), we obtain that in the simulation frame the radiation appears to be emitted at an angle of $\approx 37°$ with the y-axis, close to the observed wave front inclination angle. The emission normal to the arcs' surface results from the effect of the phase bunching of electron distribution [Hoshino and Arons, 1991, Sprangle et al., 1977]. This phenomenon takes place when the frequency of the wave is just slightly higher than the plasma cyclotron frequency. Then, the particles on average travel through an angle less than 2π in coordinate space in a wave period, they slip behind the waves and their distribution after an integer number of wave periods is bunched in gyrophase. The wave emission thus will be defined by the structure of the compressed magnetic field at the arcs, in which the electrons gyrate and produce the emission of precursor waves. The combined effects of the gyrophase bunching and the light aberration cause the precursor wave emission angle to change with the evolving shape of the ripples, leading to a wide range of the obliquity angles, as visible in Figs. 6.7 and 6.9c-d and apparent in 2D Fourier power spectra of fluctuations in B_z and E_x shown in Figs. 6.11a-b for waves in *Region B* marked in Fig. 6.9. Note however, that the dominant emission pattern comes from an average ripple profile, and the high intensity emission shows compatibility with the ripple scale length.

An effective emission angle of the bunched precursor waves is about 45°. Fig. 6.9f shows the averaged and smoothed profile of the B_z magnetic field fluctuations taken along the oblique direction, as marked with a blue parallelogram in panel (c). One can note the large wavelength in a range $(2-3.5)\lambda_{si}$, consistent with λ_{rippl}. Similar wave profile is observed in E_x and E_y electric field components (not shown). The short-wavelength modes have their magnetic fields in B_z. The associated electric field

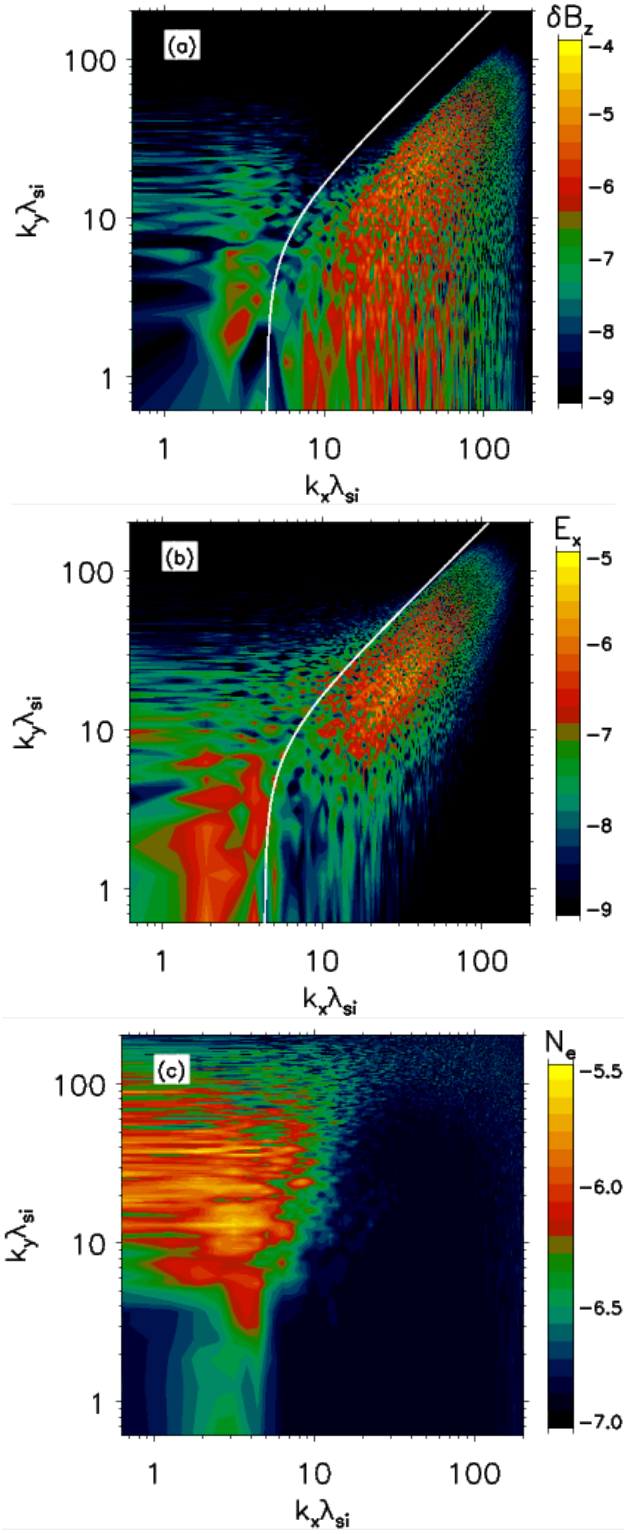

Figure 6.11: *Fourier spectra for B_z fluctuations (a), E_x (b) and the electron density (c) for Region B at $x/\lambda_{si} = 130-140$ at time $t\Omega_{ci} = 84.3$ (see Fig. 6.9). The solid white line represents the precursor wave theoretical cutoff wavenumber.*

has components laying in the $x-y$ plane, that are transverse to the magnetic field and the oblique wave-vector. The waves are thus of the X-mode type. Their spectra have

cutoffs at lower wave-numbers, as expected on theoretical grounds (see Fig. 6.11a-b, the spectrum of E_y fluctuations, not shown, is compatible with B_z). Therefore the peculiar structure of the precursor waves in my mildly relativistic shock results from the large-scale effects of the rippled shock surface, while the emission mechanism is generic and corresponds to the well known process of the electron synchrotron maser.

In addition to the dominant oblique component, the Fourier power spectrum of B_z oscillations in Fig. 6.11a shows the presence of parallel waves with $k_{B_z} \approx k_x \simeq (10-30)\lambda_{si}$, demonstrating the precursor wave emission from an average shock structure. As one can see in the map of E_x in Fig. 6.9d and the spectrum in Fig. 6.11b, the wake-field resulting from the precursor waves in the close upstream region of the shock has an oblique structure, that corresponds to the dominantly oblique precursor waves. The spectral signal has wave-vector $k\lambda_{si} \simeq 2$, in agreement with the theoretical wavenumber for the wake-field induced by the standard electron SMI scenario, as estimated in Equation 6.8. It couples in a nonlinear way to the magnetic field and density perturbations that show corresponding oblique long-wave component in their spectra (Figs. 6.11a and 6.11c).

6.2.2(c) Parametric Instability and filaments generation

The Fourier power spectrum of electron density in Fig. 6.11c has a significant wave power for transverse wavevectors with $k_y\lambda_{si} \sim 10-30$ with a longitudinal component around $k_x\lambda_{si} \sim 2-4$. The corresponding density perturbations are visible in Figs. 6.9a and 6.9e, the latter showing the density map in *Region A* in the linear scale. They form filamentary structures whose transverse scale is several electron skin depths, λ_{se}. I ascribe these perturbations to the parametric filamentation instability [Kaw et al., 1973, Drake et al., 1974] triggered when intense electromagnetic waves interact with the incoming upstream plasma. Such filaments in density and magnetic fields have been recently identified in high-resolution studies of ultrarelativistic magnetized pair shocks [Iwamoto et al., 2017, 2018, Plotnikov et al., 2018] and electron-ion shocks [Iwamoto et al., 2019]. Their presence indicates that the precursor waves remain coherent during the simulation. The filaments observed in pair plasmas largely retain their structure while convected toward the shock with the upstream flow. On the other hand, the filaments in the electron-ion plasmas quickly merge to form longer ion-scale turbulent structures ahead of the shock. In my mildly-relativistic shock the filaments resemble

those at pair shocks: they extend in a very large region upstream, up to $x/\lambda_{si} \sim 200$, but their structure is disrupted by the wave emission at oblique angles. These waves also cause a reduction in the amplitude of the filaments (compare the filaments in the *in-plane* case discussed in Sec. 6.4.1). As a result the corresponding filamentary structures are not observed in the magnetic field maps. However weak wave powers are visible at $k_x \approx 0$ in the B_z and E_x Fourier spectra in Figs. 6.11a-b, indicating nonlinear coupling. Though in conditions of mildly relativistic shocks the strength of the precursor waves is limited compared to the ultrarelativistic case and the parametric instability is not strongly unstable, this result demonstrates that high-resolution simulations are able to detect even weak signatures of a coherent precursor wave emission.

6.2.2(d) Precursor Wave Amplitudes

Fig. 6.12 shows the profiles of the precursor B_z and the wake-field E_x wave components upstream of the shock. The profile of δB_z is taken along $y/\lambda_{si} = 6$, whereas the electrostatic field $\langle E_x \rangle$ is y-averaged to filter out the E_x component of the oblique large-amplitude precursor waves. These profiles can be compared to corresponding profiles obtained in 1D simulation with the same parameters and shown in Fig. 6.18 in Sec. 6.3 .

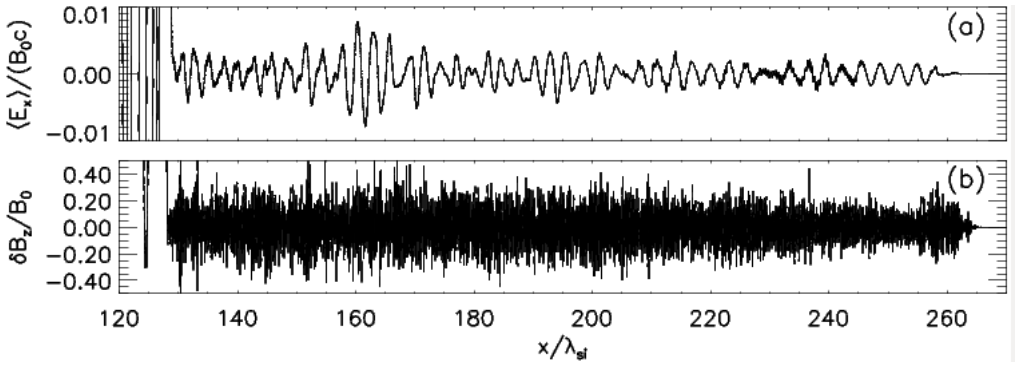

Figure 6.12: *Profiles along the shock normal of normalized upstream waves at time* $t\Omega_{ci} = 84.3$. *The electric field* $\langle E_x \rangle$ *is averaged over y-direction (a) and* δB_z *magnetic field is taken in the middle of the box along* $y/\lambda_{si} = 6$ *(b).*

The amplitudes of the precursor waves are comparable in 2D and 1D simulations. In 2D, the average amplitude of the waves in the broad upstream region extending up to $x/\lambda_{si} \approx 230$ is even larger than the waves in the tip of the precursor, that includes the strongly coherent oscillations generated in the linear stage of the shock evolution (compare also magnetic field amplitudes in the map of δB_z in Fig. 6.7). This is in

contrast to the wave structure in 1D simulation, in which the waves closer to the shock are weaker, possibly due to the effects of the effective thermal spread of the electrons reaching the shock. A final thermal spread of electrons gyrating at the shock suppresses higher harmonic wave growth and becomes significant at lower harmonics with increasing electron ring temperature [Amato and Arons, 2006]. In a 2D simulation, thermal effects are similarly expected to act toward a decrease of the precursor wave amplitude. Moreover, inhomogeneities at the shock surface may cause the wave coherency loss in the precursor. I ascribe the effective amplification of the precursor waves observed in mildly relativistic shock to the effects of the shock front rippling. As explained in Sec. 6.2.2(b), the shock ripples are organised as to produce a semi-coherent in phase and modulated train of oblique precursor waves. Thus, instead of acting destructive on the waves, the ripples actually increase their amplitudes in the extended upstream region.

The magnetic field fluctuation amplitudes normalised to the upstream field strength, $\delta B/B_0$, and to the upstream *electron* kinetic energy, $\epsilon_p = \delta B^2/(2\mu_0\gamma_0 N_e m_e c^2)$, are listed in Table 6.1, in which comparison with other works is also provided. Here, δB refers to the total magnetic field that constitute the precursor ($\delta B = \delta B_z$ in the out-of-plane case, and $\delta B = \sqrt{\delta B_x^2 + \delta B_y^2 + \delta B_z^2}$ in the in-plane case). The amplitudes are averaged in the region of $x/\lambda_{si} = 129 - 134$, located about $2\lambda_{si}$ from the shock. A full comparison of results between 1D- and 2D setups can be found in Fig. 6.19 in Sec. 6.3, which presents time evolution of the field amplitudes thus calculated. One can note that in contrast to 1D simulation, in which the wave amplitude initially decreases with time due to the heating effects discussed above and then saturates, the level of the magnetic field fluctuations in 2D run, after initial short increase, stays roughly constant throughout the simulation. This is due to the fact that the shock front ripples quickly emerge in the system and dominate the emission of the precursor waves.

The magnetic field oscillations amplitude can also be compared to the results obtained for ultra relativistic shocks. Since the emission of precursor waves is governed by the electron magnetization, in Table 6.1 the available results for shocks with $\sigma_e = 5$ are listed. As expected, the amplitudes obtained here are smaller than the level reported in 1D simulation of pair shocks in Gallant et al. [1992], both in terms of $\delta B_z/B_0$ and ϵ_pHowever, they are much larger than amplitudes obtained for pair shocks in 1D and

Table 6.1: *Precursor wave amplitudes $\delta B/B_0$ obtained in my simulations, compared with other works. Here, δB refers to the total turbulent magnetic fields that constitute the precursor waves ($\delta B = \delta B_z$ in the out-of-plane case, and $\delta B = \sqrt{\delta B_x^2 + \delta B_y^2 + \delta B_z^2}$ in the in-plane case). I averaged the amplitude in a region $5\lambda_{si}$ wide, located $2\lambda_{si}$ upstream of the shock. Iwamoto et al. [2019] performed the average of the wave energy and amplitude in a region that contains the entire laminar (i.e. non collapsing) wake-field, about $70\lambda_{si}$-wide, and about $32\lambda_{si}$ upstream of the shock. This is done to focus on the linear phase of the PDI. Gallant et al. [1992] performed the average in a region upstream including the full precursor.*

	$\delta B/B_0$	$\delta B^2/(2\mu_0\gamma_0 N_e m_e c^2)$
2D $i-e^-$, out-of-plane	0.19 ± 0.01	0.09 ± 0.005
1D $i-e^-$	0.18 ± 0.01	0.08 ± 0.005
2D $i-e^-$, in-plane	0.15 ± 0.01	0.07 ± 0.005
1D e^+-e^- Gallant et al. [1992]	$0.46^{+0.18}_{-0.12}$	$0.53^{+0.22}_{-0.15}$
2D e^+-e^- Iwamoto et al. [2019]	0.064 ± 0.031	0.010 ± 0.005
1D e^+-e^- Iwamoto et al. [2019]	0.10 ± 0.01	0.025 ± 0.005
2D $i-e^-$ Iwamoto et al. [2019]	0.50 ± 0.10	0.65 ± 0.25
1D $i-e^-$ Iwamoto et al. [2019]	0.75 ± 0.09	1.4 ± 0.4

2D simulations by Iwamoto et al. [2019]. The amplitudes are much smaller than in ion-electron shocks with $\gamma_0 = 40$ [Iwamoto et al., 2019]. For these ultra relativistic shocks, the wave energy for both 1D and 2D exceeds that in pair plasmas by almost two orders of magnitude and the 2D amplitude is close to the 1D level. This amplification over the pair plasmas is attributed in high-Γ_{sh} shocks to the so-called positive feedback process, in which incoming electrons heated in the wake-field cause enhanced precursor wave emission, that in turn induces a stronger wake-field. In the case analysed in here, however, the wake-field does not reach very high amplitudes (see Sec. 6.2.3) and the positive feedback should not operate. However, electromagnetic precursor wave amplification up to the 1D level is achieved through the effects of the shock rippling.

6.2.3 Particle Heating and Acceleration

6.2.3(a) Electron Interactions with Upstream Waves

Figs. 6.13a-c show electron and ion phase-space distributions across the shock, as well as the mean particle kinetic energy, $\langle \gamma - 1 \rangle m_l c^2$, normalized to the bulk kinetic energy of injected upstream ions, $(\gamma_0 - 1)m_i c^2$. It can be seen that electrons flowing in towards the shock become gradually heated, and in the close upstream region a very small population of particles accelerated up to $\gamma \sim 40$ can be found. Inspection of

panel e) indicates that up to $x/\lambda_{si} \simeq 160$, the mean kinetic energy stays at the far upstream value and it is modulated with a regular energy increase and decrease pattern. Closer to the shock one can observe a steady, albeit a weak, average energy growth.

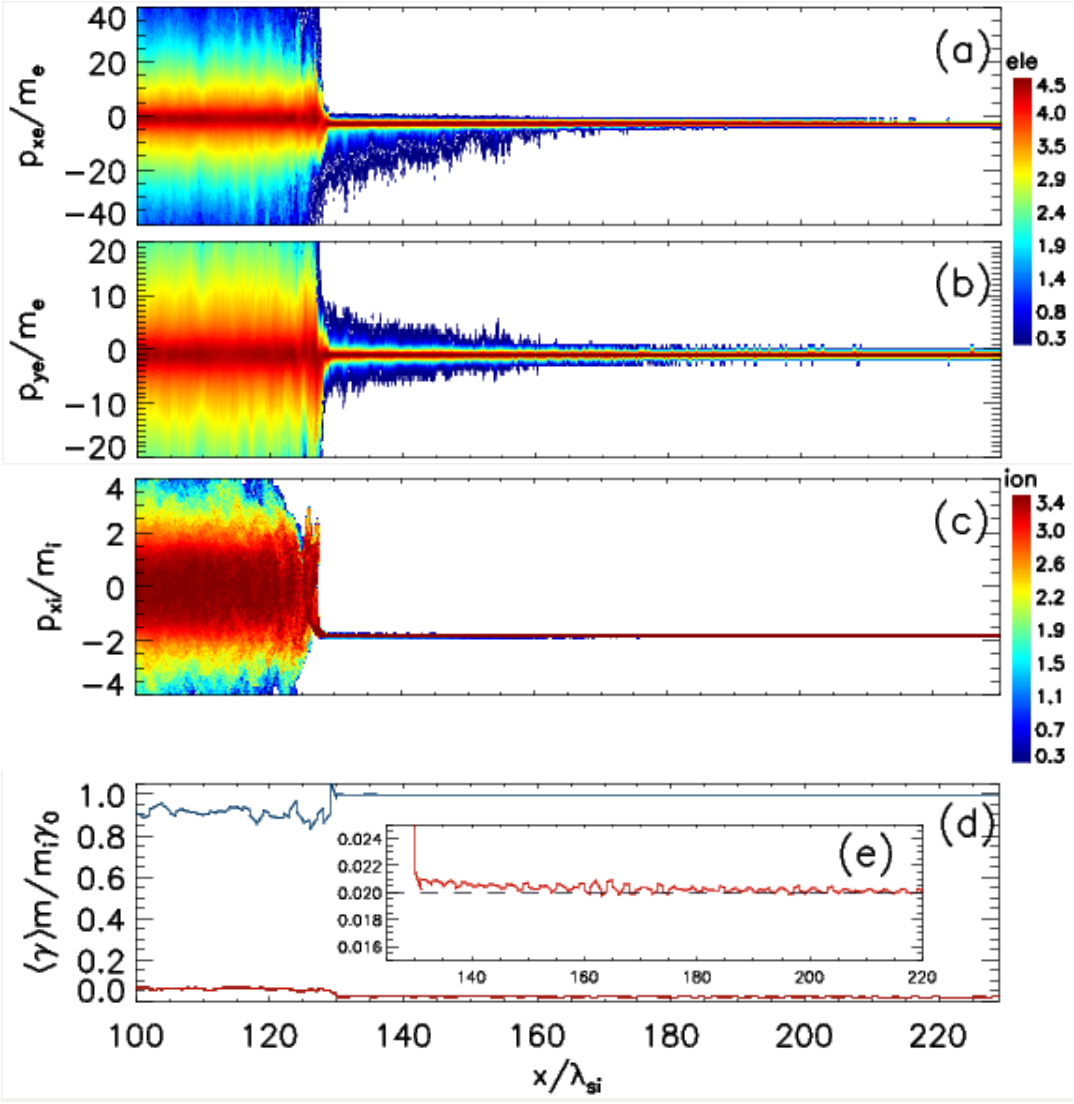

Figure 6.13: *Phase-space distributions map for electrons along x axis (a) and along y axis (b), and distributions map for ions along x axis (c) in the upstream region, at time $t = 84.3\ \Omega_{ci}^{-1}$; mean particle energy (blue for ions and red for electrons) in units of the ions upstream bulk energy (d) and close up of the electron mean particle energy in the vicinity of the shock (e).*

As noted before, the action of the ponderomotive force on the upstream plasma leads to the excitation of the longitudinal plasma motions and associated Langmuir waves (i.e. the wake-field waves). However, as it can be seen from Fig. 6.12a, the average amplitude of the wake-field does not exceed $\langle E_x \rangle/(B_0 c) \sim 0.01$, and the wave can be considered weak. This results from a relatively weak amplitude of the precursor waves, that can be measured through the so-called strength parameter $a = e\delta E/m_e c\omega$,

where δE is the amplitude of the wave electric field and ω is the wave frequency [Kuramitsu et al., 2008]. The waves are considered to be strong if $a \gtrsim 1$, in which conditions they can generate large-amplitude Langmuir waves. One can estimate the strength parameter applying the approximate formula used in Iwamoto et al. [2017]:

$$a \simeq \gamma_0 \sqrt{\sigma_e} \frac{\omega_{\rm pe}}{\omega} \frac{\delta B}{B_0}. \tag{6.10}$$

As one can see in Fig. 6.11a, typical wavenumbers range in $k \sim (15-40)\lambda_{si}^{-1} \approx (2.1-5.7)\lambda_{se}^{-1}$. Combining these wavenumbers with the dispersion relation in Equation 6.5, one obtains the wave frequency in a range:

$$\frac{\omega}{\omega_{pe}} \sim 2.6-5.9. \tag{6.11}$$

With the average magnetic field amplitude, $\delta B_z/B_0 \simeq 0.19$ (see Table 6.1), the strength parameter is:

$$a \simeq 0.15-0.30, \tag{6.12}$$

and the corresponding amplitude of the wake-field [Hoshino, 2008]:

$$\frac{\langle E_x \rangle}{B_0 c} \simeq \frac{\xi a^2}{\sqrt{1+\xi a^2}} \left(\frac{1}{\sqrt{\sigma_e}\gamma_0}\right) \simeq 2.5\times10^{-3}-0.01, \tag{6.13}$$

in agreement with my simulation result. Here I assumed $\xi = 1/2$, appropriate for a linearly polarised wave.

The interactions of the incoming electrons with a Langmuir wave, even of such small amplitude, should lead to oscillatory motion that can be observed as modulations in phase-space correlated with the phase of the $\langle E_x \rangle$ field. Such modulations are responsible for the acceleration-deceleration pattern in the mean electron energy in Fig. 6.13e. Since far upstream from the shock the wave is sinusoidal, there is no net acceleration. However, these coherent oscillations in velocity can be regarded as an apparent heating, with the maximum energy [Hoshino, 2008]:

$$\frac{\epsilon_{\rm max}}{\gamma_0 m_e c^2} \simeq e\langle E_x \rangle L \simeq \frac{\eta a^2}{\sqrt{1+\eta a^2}}(1+\beta_0) \simeq 0.1, \tag{6.14}$$

where the wavelength $L \sim 1/k$ and I considered the maximum amplitude of the wake-

field from Equation 6.13. This is compatible with the amplitude of the average electron energy oscillations but much less than the maximum $\epsilon_{\max}/\gamma_0 m_e c^2 \approx 20$, noted above in the near upstream region. Hence, the enhanced energisation in this region suggests that the electrons may be involved also in nonlinear interactions with the wake-field.

As discussed above, the occurrence of the shock surface rippling causes enhanced emission of the precursor waves at oblique angles. This in turn produces oblique Langmuir waves. The wake-field profile shown in Fig. 6.12a averages these fluctuations, which at different spatial locations may reach large amplitudes. In fact, the time evolution analysis shows that from time $t\Omega_{ci} \sim 40$ on, when the oblique precursor wave structure is well established, episodes of stronger semi-coherent wave emission from the shock lead to generation of stronger wake-field in the close upstream region. These wake-field not only leads to enhanced oscillations visible in the electron phase-space for $x/\lambda_{si} \sim 127 - 180$, but also to electron acceleration demonstrated by a higher-energy (anisotropic) component in $p_{\rm xe} - x$ and $p_{\rm xe} - x$ distributions. This is a signature of the nonlinear collapse of the wake-field. I will show below that the signatures of electron acceleration in this region can be explained as resulting from interactions between electrons and strong wake-field. It can be noted that even the ion phase-space shows very weak disturbances in the amplified wake-field region.

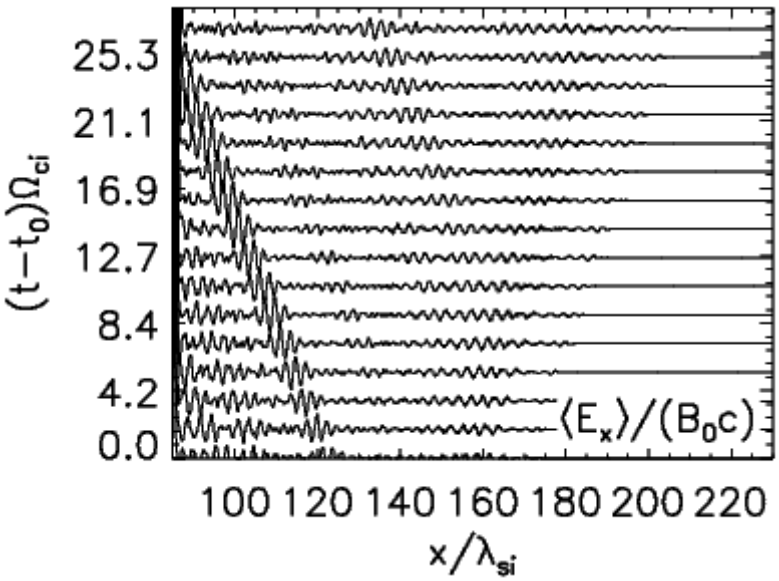

Figure 6.14: *Stack plot of the averaged wake-field waveforms, $\langle E_x \rangle/(B_0 c)$, upstream of the shock, starting at time $t_0\Omega_{ci} = 56.2$ and ending at $t_{\max}\Omega_{ci} = 84.7$. The profiles are shifted so that the shock at all times is located at the left side of the figure at $x/\lambda_{si} \simeq 86$.*

As described in Sec. 4.2, the ponderomotive force is proportional to the gradient of the wave pressure and can act also inside the precursor if the electromagnetic waves are modulated. One of the modulation process is the stimulated Raman scattering instability that couples to the wave modes generated by the Parametric Decay Instability (PDI). The enhanced emission of the precursor waves through rippling structures discussed above amplifies the waves and it may also trigger nonlinear processes of the Forward Raman Scattering (FRS). In nonlinear FRS the scattered electromagnetic waves successively decay into another electromagnetic waves and Langmuir waves. As the frequency of the scattered waves is lower than that of the pump waves, broadband precursor wave spectra extending from the initial $\omega' \gtrsim \Omega_{ce}$ down to $\omega' > \omega_{pe}$ are generated. Similarly, broadband Langmuir waves are produced with $k'_L < \omega_{pe}/c$ and $\omega'_L \simeq \omega_{pe}$ [Hoshino, 2008] .

In the upstream plasma rest frame the electromagnetic and Langmuir waves at all wavenumbers have phase velocities in the upstream direction. However, as an effect of non-linear FRS, in the simulation frame part of these waves move toward downstream. Since the phase velocities of the Langmuir waves are close to the speed of light, these waves can now scatter the electrons and boost them toward the shock. Fig. 6.14 shows the stack plot of the averaged wake-field profiles upstream of the shock for time frame $(t - t_0)\Omega_{ci} \simeq 28.1$, starting at $t_0\Omega_{ci} = 56.2$. The profiles are shifted so that the shock at all times is located at the leftmost boundary of the figure. Far upstream of the shock, the Langmuir waves propagate away from the shock, while in the region extending as far as $(x - x_{\rm sh})/\lambda_{si} \approx 70$, the wake-field on average moves along the negative x-direction, i.e. towards the shock front. This downstream-directed motion of the wake-field waves supports a scenario of the nonlinear FRS operating in the mildly relativistic shock. It also explains higher-energy components in the electron phase space in the close upstream region, in which large-amplitude Langmuir waves can be excited (see the structure at $x/\lambda_{si} \approx 120$ at $t = t_0$ in Fig. 6.14) and accelerate electrons. As in the ultrarelativistic shock studied in Hoshino [2008], the electron acceleration through these waves may be due to the so-called phase slippage effect, described in Sec 4.2, and it would account for the anisotropy in $p_{\rm xe} - x$ (Fig. 6.13a). It can be also combined with a direct acceleration in the upstream motional electric field in the shock-surfing acceleration (SSA) process that would accelerate electrons in the

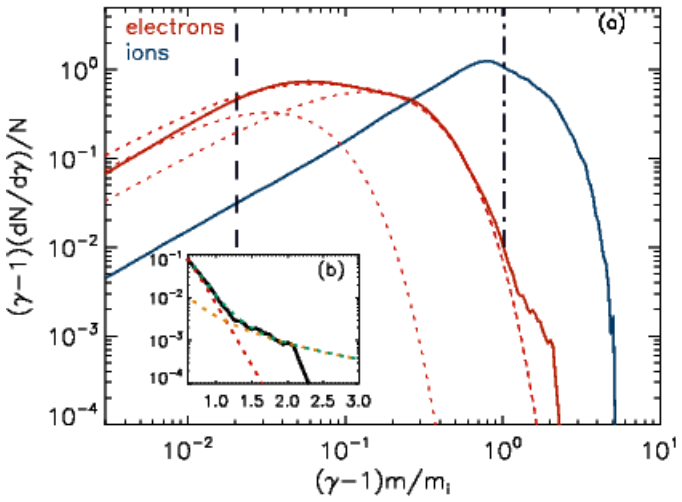

Figure 6.15: *Particle energy spectra (red for electrons, blue for ions) in a region* $x/\lambda_{si} = 113-123$ *downstream of the shock at* $x_{\rm sh}/\lambda_{si} \approx 127$ *at time* $t\Omega_{ci} = 84.3$ *(a). Energy axis is scaled with respective particle mass,* $m = m_e, m_i$*. Vertical dashed and dash-dotted lines mark initial bulk kinetic energies of the electrons and ions, respectively. The electron spectrum is fitted with double Maxwellian distribution (red thick dotted line) composed of relativistic 2D Maxwellians shown with thin red dotted lines. Inset (b) presents close-up of the high-energy part of the electron spectrum, in which fits of the double Maxwellian (red), a power-law* $\propto (\gamma-1)^{-2.1}$ *(yellow) and their sum (green) are shown with dotted lines.*

y-direction. The anisotropy in the $p_{\rm ye} - x$ toward positive momenta is the evidence that the SSA operates in the shock upstream (Fig. 6.13b). We further show in Sec. 6.2.3(c) through the analysis of trajectories of selected electrons that on their approach to the shock the energy gains and losses occur through the electron motion in the direction of E_y.

In spite of moderately efficient production of coherent precursor waves, the bulk energy gain of electrons before they hit the shock is only 5% of their initial kinetic energy (see Fig. 6.13e). The majority of the energy transfer from ions to electrons takes place in the shock transition and the close downstream region, as will be discussed in the following section.

6.2.3(b) Downstream Particle Spectra

Fig. 6.15 shows kinetic energy spectra of electrons (red line) and ions (blue line) at time $t\Omega_{ci} = 84.3$ in a region $x/\lambda_{si} = 113-123$ downstream of the shock. The shock is located at $x_{\rm sh}/\lambda_{si} \approx 127$. Vertical lines in the plot mark initial bulk kinetic energies of the particles.

It can be seen that although some electrons reach energies exceeding the kinetic

energy of upstream ions, their average Lorentz factor, $\langle \gamma_e - 1 \rangle / m_i \approx 0.11$ is only 13% of the mean downstream ion Lorentz factor, $\langle \gamma_e - 1 \rangle / m_i \approx 0.81$. The two species do not reach equipartition, differently from what it is typically observed in ultrarelativistic shocks [e.g., Lyubarsky, 2006, Sironi and Spitkovsky, 2011]. Downstream of the shock ions and electrons carry, respectively, $\sim 81.5\%$ and $\sim 10.6\%$ of the initial ion kinetic energy per particle, $(\gamma_0 - 1) m_i c^2$. Thus as much as $\sim 7.9\%$ of the energy is transferred to electromagnetic waves and turbulence, since as expected the total energy in the upstream region is compatible with the total energy in the downstream, when measured in the simulation frame.

The ion spectrum shows mainly relaxation around the mean ion energy and tends towards a 2D relativistic Maxwellian distribution. Higher-energy part of the spectrum contains particles with Lorentz factors up to $\gamma_i \approx 6$. These are particles reflected from the shock compressed magnetic field, that typically perform a single loop in the upstream motional electric field before being advected, experiencing one cycle of the shock-drift acceleration (SDA). The electron distribution is more asymmetric. The bulk of the spectrum can be best fitted with two Maxwellians. They are shown with *thin* red dotted lines, and the *thick* red dotted line is the combined fit. The hotter Maxwellian peaks at $(\gamma_e - 1)/m_i \simeq 0.2$ and dominates the lower-temperature Maxwellian that has a maximum at the Lorentz factor about 6 times smaller. The electron spectrum also shows a supra-thermal narrow-range component for $(\gamma - 1)/m_i \gtrsim 1$, whose slope is compatible with a power-law $\propto (\gamma - 1)^{-p}$ with a spectral index of $p \simeq 2.1$, as shown with the yellow dotted line in Fig. 6.15b. The particle spectrum presented in Fig. 6.15 represents a steady-state distribution that does not appreciably change with the distance from the shock.

6.2.3(c) Energisation Processes

As it was discussed in Sec. 6.2.3(a), although coherent precursor waves exist upstream where they generate wake-field, the interaction of the latter with the incoming plasma causes only a limited energy transfer from ions to electrons. Nevertheless, particle heating at the shock proceeds beyond adiabatic compression and also supra-thermal electrons are produced. Note that due to a weak electron and ion coupling in the upstream region, the ions enter the shock with bulk energy much larger than electrons. On their gyration at the shock-compressed magnetic field, the ions thus

penetrate deeper, and the charge-separation electrostatic field is produced at the shock that points towards upstream. However, unless the field-particle interaction time is shorter than an electron gyro-time, this cross-shock electric potential field cannot provide B-parallel electron heating in our strictly perpendicular shock with out-of-plane $\boldsymbol{B_0} = B_z$, as the particle motion is constrained in the x-y plane.

In this section I provide an interpretation for the electron energisation processes in the shock transition region and the production of downstream particle spectra by analysing sample particle trajectories.

Fig. 6.16 illustrates the main stages of electron energisation, in which we trace trajectories of particles traversing the shock transition. The particles are selected in the far upstream region of the shock at the same x-coordinate along the y-axis, so that they reach the vicinity of the shock ramp at the same time. Some of the traced particle trajectories are shown with thin grey lines in panels (a)-(c). At each time interval I selected a single representative electron whose trajectory is plotted with thick red line for better visualisation: in each panel a different particle is highlighted. The temporal evolution of the kinetic energy *averaged* over the whole particle sample is shown with red line in panel (d). In the same panel we also plot contributions to the energy gains or losses from the work done by the E_x (green line) and E_y (blue line) electric field components, $(\gamma - 1)_{E_i} = \int_{t_0}^{t_1} q_e v_i \cdot E_i/(m_e c^2) dt, i = x, y$, where $q_e = -e$, local electric field values are measured at particle positions, and the integration time is from $t_0\Omega_{ci} = 20$ to $t_1\Omega_{ci} = 30$. Finally, in panel (e) we plot with red line the particle-sample average of the magnetic moment, μ, and the magnetic field profile (blue line) along particle trajectories. Here μ is defined as $\mu = p_\perp/2m_e|\boldsymbol{B_p}|$, where $p_\perp$ is the transverse momentum of the particles in a local magnetic field, $\boldsymbol{B_p}$, and $\mu_0 = \mu(t_0)$. Note that the averaged quantities shown in panels (d) and (e) are calculated from much larger particle set than that shown in panels (a)-(c).

As discussed in Sec. 6.2.3(a), the electrons approaching the shock may interact with the wake-field. In the far upstream region the wake-field amplitude is weak and most of the particles only oscillates in the waves' electrostatic field not gaining net energies. Closer to the shock the wake-field is stronger and the electrons interacting with these waves may become decoupled from the bulk flow. When this occurs, the electron gyro-centres still move toward the shock with the $\boldsymbol{E_0} \times \boldsymbol{B_0}$ drift velocity, but

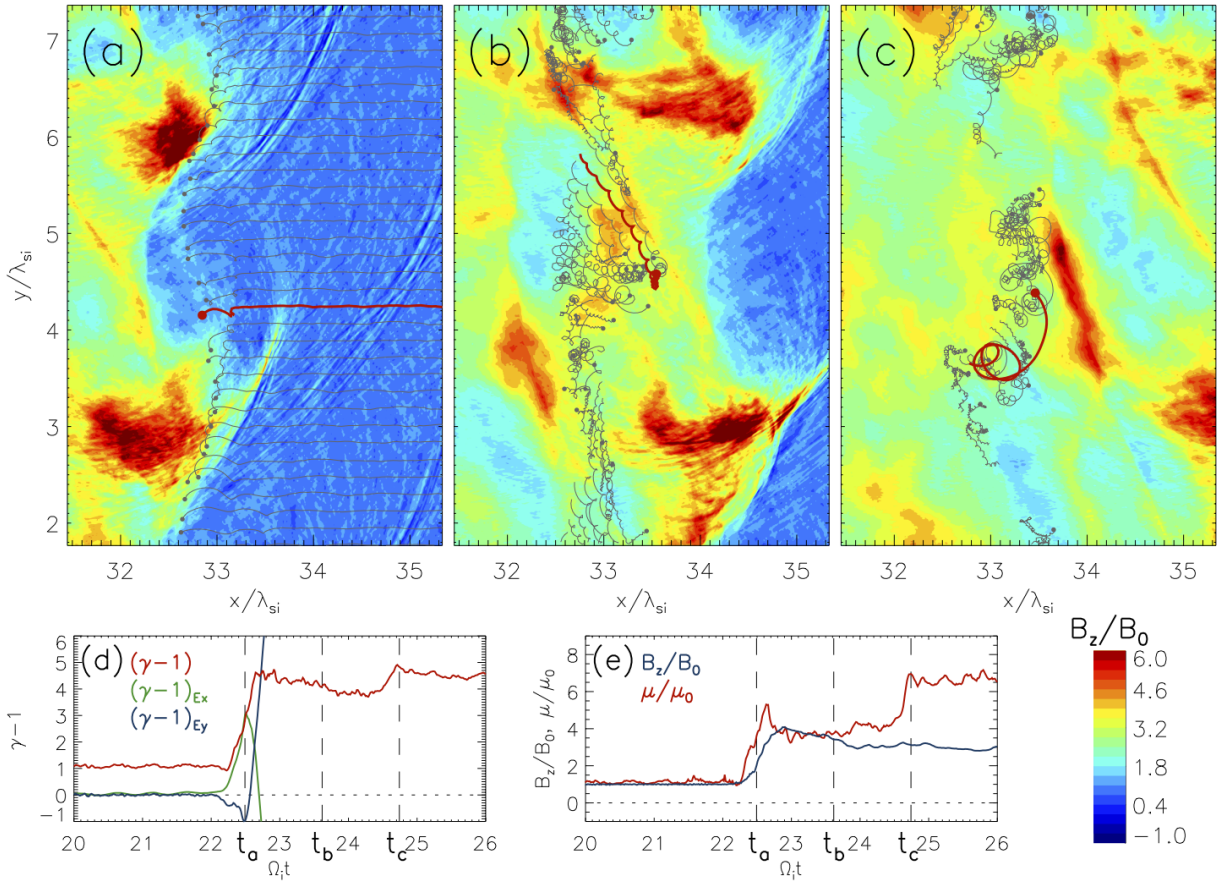

Figure 6.16: *Trajectory segments of sample electrons superposed on the map of the normalised magnetic field strength, $|B_z|/B_0$, at three time intervals. The scale of the map is linear and only a small portion of the numerical box is shown. The panels (a)–(c) display the state of the system at times t_a (a), t_b (b), and t_c (c) that are marked in panels (d) and (e), and the circles indicate the positions of the electrons at these moments. The particles are selected in the far upstream region of the shock to originate at the same x-coordinate along the y-axis. The grey lines show trajectories history for the time span $0.3\Omega_{ci}^{-1}$. Selected single electron trajectories are plotted with thick red lines, each panel displaying a different particle. Panel (d) shows the time evolution of the total kinetic energy (red line)* averaged *over the particle sample from time $t_0\Omega_{ci} = 20$ to $t_1\Omega_{ci} = 26$ and the* average *acceleration rates in the electric field at particle positions split into the x- (green line) and y- (blue line) components of the electric field work, $(\gamma-1)_{E_i} = \int_{t_0}^{t_1} q_e v_i \cdot E_i/(m_e c^2)dt, i = x, y$, that is perpendicular to the magnetic field. Panel (e) shows the magnetic moment (red line) and the magnetic field profile (blue line) along particle trajectories averaged over the electron sample.*

they start to feel the motional electric field and are accelerated in the y-direction. We noted in Sec. 6.2.3(a) that this SSA-like process is visible through the anisotropy in the $p_{ye} - x$ phase-space. However, very few particles experience strong interactions with the wake-field and most of them reach the shock vicinity unaffected. Only a portion of them are weakly decoupled from the bulk flow and show small-amplitude oscillations

in their trajectories, as it can be visible for some particles in Fig. 6.16a. A significant impact of the upstream waves can be instead observed just in front of the shock for electrons that on their way encounter strong waves emitted by a shock ripple. As one can see in Fig. 6.16a, the waves form an arc-like features in the B_z distribution and also have corresponding E_x and E_y electric field components (not shown). The E_x wave field is strong enough to effectively stop a particle and decouple it from the bulk flow. This causes wiggles in particle trajectories, well visible for the electron marked with red line at $(x/\lambda_{si}, y/\lambda_{si}) \approx (33.2, 4.2)$ and particles below it at $y/\lambda_{si} \approx 3.2-4$ that were smashed by the waves emitted by the lower ripple, and particles at $y/\lambda_{si} \approx 5.9-7.4$, affected by the upper ripple. Note, that at time t_a at which Fig. 6.16a is plotted the emitted strong waves are already behind the affected electrons. After decoupling from the flow, the electrons experience strong pull by the upstream-directed electrostatic E_x field and also the acceleration in the motional E_y field. The corresponding particle average energy gain is dominated at t_a by the work done by the E_x field, since the work in the E_y field is averaged over the phase of the gyrating electrons in the motional electric field (see panel (d)). I interpret the electrostatic field that acts on particles as due to strong wake-field excited by the waves emitted by the ripple. It can also be partially due to the cross-shock potential field that exists in this region and can be probed by the electrons because their interaction time is shorter than the electron gyration time. Energisation at this stage is non-adiabatic, as evidenced by a jump in the average magnetic moment (panel (e)). The interaction of an electron with the waves produced by the ripples as described above is a crucial and necessary step for its subsequent acceleration to higher energies. Such interaction is possible in the mildly relativistic shock only because the formation of the strong rippling. To my knowledge, such a process for a rippled shock has not been reported in the literature before.

At a later stage, the electrons hitting the shock experience the adiabatic heating in the compressed magnetic field. This takes place while the particles undergo the $\boldsymbol{E}\times\boldsymbol{B}$ drift, which has $-E_x B_z \hat{\boldsymbol{y}}$ component that is equal to the velocity of the rippling waves along the shock surface. In fact, the combined motion of transmitted ions and the shock-reflected ions drifting across the shock and along its surface results in the charge-separation electric field in the ripples with components of amplitude $E_x \sim E_y \gg E_0$. Thus in the simulation frame the particles are dragged together with the downward moving

and advancing ripple and are accelerated along the E_y field and decelerated in the E_x field. This corresponds to diverging $(\gamma-1)_{E_x}$ and $(\gamma-1)_{E_y}$ energy gains at $t \gtrsim t_a$. One can see the drifting electron trajectories in Fig. 6.16b. Note, however, that the behaviour of individual particles may differ from that of the averaged picture. When an electron is decoupled in the upstream from the bulk flow and starts gyrating in the motional electric field it may hit the shock with an unfavourable phase and with a low energy. After adiabatic heating at the shock it will be advected downstream and it will populate the low-energy portion of the downstream electron spectrum, together with electrons that are transmitted through the shock without interacting with the ripple-generated upstream waves.

After a net non-adiabatic energy gain of the averaged population around t_a, the electrons reside in the shock overshoot and their energy evolution is well described by adiabatic processes. This stage is illustrated in Fig. 6.16b at t_b. At this stage the magnetic moment is conserved while the magnetic field strength decreases, which results in gradual energy loss due to decompression (compare panels (d) and (e) at t_b). However, the mean energy of the electrons again increases at around $t \approx t_c$, which is associated with a second jump in the magnetic moment. Inspection of particle trajectories in panel (c) reveals that gyroradii of some electrons are comparable to the scale of the turbulent field (note sample electron marked with red line). These electrons can therefore undergo resonant scattering off these waves. Essentially all electrons with Lorentz factor $\gamma \gtrsim 10$ have large enough gyroradii to experience a gyro-resonant interaction and become accelerated. They will populate a higher-energy portion of the downstream spectrum.

One can see that at times $t > t_c$ the average energy for the analysed particle sample saturates. This is due to the lack in the downstream of the turbulent fields with larger scales that would enable resonant interactions with higher-energy particles. The scale of the turbulence in the region of the resonant scattering is set by the ripple wavelength and it exists in a narrow zone downstream of the overshoot, so that only particles that happen to encounter the resonant waves while they drift downstream can be energised.

The features discussed here for the average electron population can explain the structure of the downstream electron energy spectrum as formed by a single population of particles accelerated in the shock transition: some particles that are decoupled by the

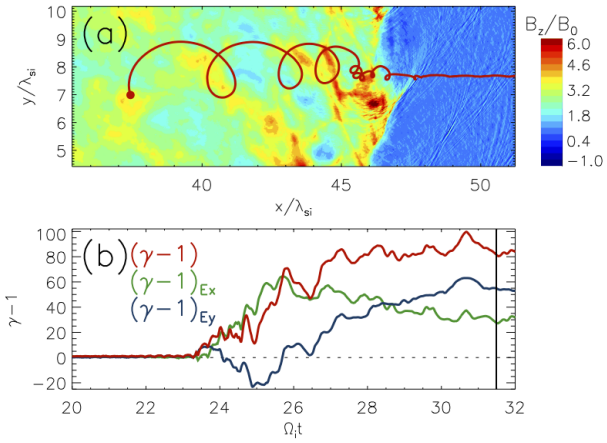

Figure 6.17: *Trajectory of a highly energetic electron overlaid on the map of B_z magnetic field (a). The map is plotted at time $t\Omega_{ci} = 23.6$, at which the particles first interact with the shock front, located at $x/\lambda_{si} \simeq 34$. The scale of the map is linear. Time evolution of the total kinetic energy for the electron (red line) and acceleration rates in the E_x and E_y electric fields (b, see Fig. 6.16). The trajectory ends at time $t \simeq 31.5$, as marked with black vertical line.*

upstream waves from the bulk flow and accelerated in the shock through the ripple-mediated processes can experience further acceleration in gyro-resonant interactions with the waves. Therefore, the transition between the low-energy and high-energy components in the electron spectrum is smooth. It is in addition deformed by yet another energising process that is the stochastic second-order Fermi-like scattering off the turbulence present in the shock. Electrons accelerated in this process can find favourable conditions of local turbulence encountered on their way across the shock. Example is the particle shown in Fig. 6.17. After decoupling from the upstream flow this electron experienced multiple inelastic scatterings in the shock transition gaining or loosing its energy through the action of E_x and E_y electric fields and finally reaching an energy in excess of $\gamma_e \approx 80$. Such particles form the supra-thermal power-law portion of the electron spectrum. However, these particles are rare, and most of the scattered particles are less successful and they contribute to the bulk of the downstream electron population. In this mildly relativistic magnetized shock, the electromagnetic turbulence in the shock transition is relatively narrow, so that stochastic scattering does not lead to additional significant electron acceleration further downstream. I again stress that on the approach to the shock some electrons are accelerated in resonant interactions with strong wake-field occasionally generated in the upstream, and they will also contribute to the higher-energy portion of the downstream electron spectrum.

6.3 Comparison with a 1D simulation

The results presented in Section 6.2 can be compared with the results of a 1D simulation. In such a setup the development of the rippling and obliquely emitted waves is suppressed. In the ultra relativistic regime 1D amplitudes of the SMI-generated precursor waves are observed to be systematically larger than in 2D because of the inhomogeneity in the shock surface through which the waves may loose coherence in phase [Iwamoto et al., 2017, 2018]. However, in the electron-ion plasma the waves can be significantly amplified due to the positive feedback process, in which electrons accelerated in the shock upstream enhance the precursor wave emission that in turn induce stronger wakefield, accelerating the incoming electrons even more efficiently, up to the energy equipartition between electrons and ions [Lyubarsky, 2006, Hoshino, 2008]. We have recently showed in Iwamoto et al. [2019], that in ultrarelativistic shocks this mechanism operates in 2D at high electron magnetizations, $\sigma_e \gtrsim 1$, at which the amplitude of the precursor waves is comparable to the 1D case. In our 2D simulation with $\varphi_B = 90°$ the positive feedback process is not operative. However, the wave amplification observed is ascribed to the presence of the shock rippling. The 1D simulation is performed to evaluate the precursor wave amplitudes in a setup devoid of multidimensional effects that should possibly provide the most efficient wave generation through SMI.

1D simulation setup is the same as that for the 2D simulation, but the transverse dimension of the computational box is only 5 cells wide. The simulation can be thus considered 1D, since $\Delta y \ll \lambda_{se} \ll \lambda_{si}$. Fig. 6.18 shows the wave profile for the 1D simulation at time of $\Omega_{ci}t = 84.7$, the same as t_{max} in 2D simulations. The shock is located at $x/\lambda_{si} \sim 127$, and its velocity is compatible to the one measured in the 2D

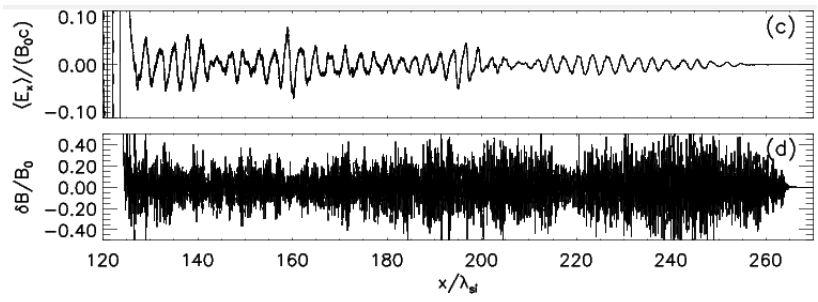

Figure 6.18: *Upstream wave profiles for E_x and B_z in 1D simulation at time $t = 84.7\Omega_{ci}^{-1}$.*

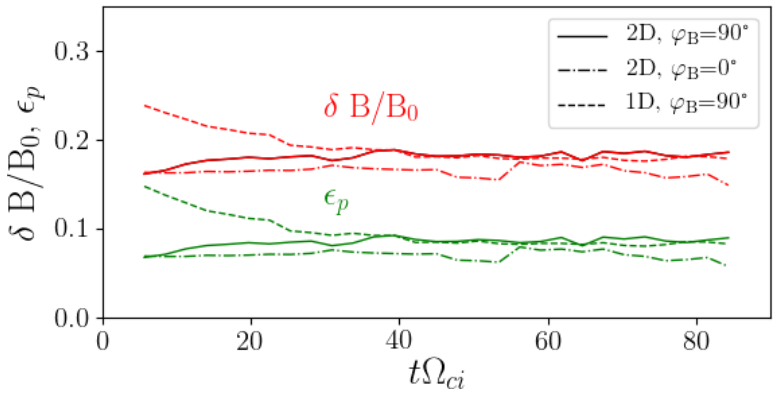

Figure 6.19: *Wave amplitude normalised to the upstream magnetic field, $\delta B/B_0$, and precursor wave energy normalised to the upstream electron kinetic energy, ϵ_p, for the 2D out-of-plane (thick line), 2D in-plane (dashed-dotted-line) and 1D simulations (dashed line), in function of the simulation time.*

out-of plane simulation. 1D setup allows only the E_x, E_y and B_z field components. The fluctuations in E_y are correlated with B_z and so the waves are X-mode electromagnetic waves. The precursor wave profiles in the 1D setup can be directly compared with that obtained in 2D (see Fig. 6.12 and also Fig. 6.24 below). Their amplitudes are also listed in Table 6.1. The 1D structure of the precursor waves is different than in 2D. In the latter case, the wave amplification due to shock ripples causes the amplitude near the shock to be larger than the one of the waves emitted in the early stage of the simulation. In the 1D case, the waves emitted in the later stage are weaker, since the presence of electrons heated on their way to the shock deteriorates the emission of the precursor waves [Amato and Arons, 2006].

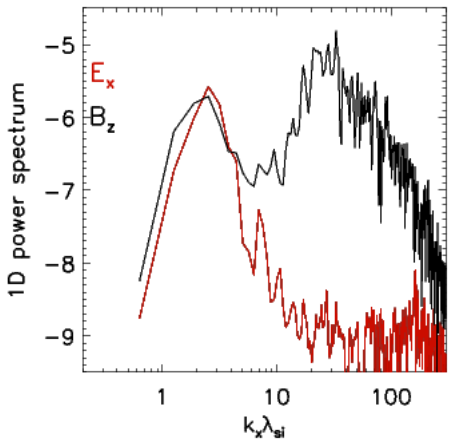

Figure 6.20: *1D Fourier power spectrum for B_z and E_x (black and red respectively), in the region $x/\lambda_{si} = 130 \div 140$ at time $t = 84.3\ \Omega_{ci}^{-1}$.*

Fig. 6.19 shows the time evolution of the wave amplitude normalised to the upstream magnetic field strength ($\delta B/B_0$) and the precursor wave energy $\epsilon_p = \delta B^2/(2\mu_0\gamma_0 N_e m_e c^2)$ (see Sec. 6.2.2(d)) for 1D and 2D simulations. The profile for 1D demonstrates the influence of the thermal effects noted above. A discussion of the results for 2D out-of-plane simulation is given in Sec. 6.2.2(d). One can note that in the 2D in-plane case the total precursor waves amplitude is only slightly smaller than the one observed for $\varphi_B = 90^o$ and the wave evolution is similar. This shows that a shock rippling-mediated amplification mechanism is operating also in the in-plane case. I discuss the $\varphi_B = 0^o$ simulation results in Sec. 6.4.1(a)).

Fig. 6.20 shows the 1D Fourier power spectra upstream of the shock, in the region $x/\lambda_{si} = (130 - 140)$. The signal band in the magnetic field oscillations, B_z, is consistent with the SMI precursor waves observed in the 2D case. The electrostatic component in E_x has a wavenumber of $k_{E_x,1D} \sim 2$, consistent with the theoretical wave number for SMI-generated wake-field.

A 1D simulation imposes a much lighter computation burden, so my 1D simulation has been prolonged up to $t\Omega_{ci} \sim 163.6$, in order to investigate possible long-term effects. Fig. 6.21 shows the particle phase-space distribution at this final simulation time. The shock is located at $x/\lambda_{si} \sim 239$. The phase-space structure is consistent to the one

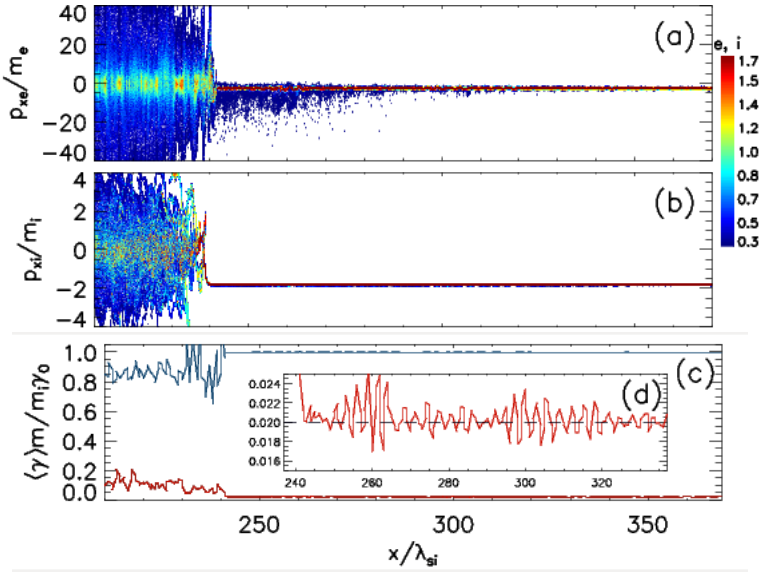

Figure 6.21: *Phase-space distributions map for electrons (a) and ions (b) along the x-axis (b) in the upstream region, at time t = 163.1 Ω_{ci}^{-1}; mean particle energy (blue for ions and red for electrons) in units of the ion upstream bulk energy (c) and close up of the electron mean particle energy in the vicinity of the shock (d).*

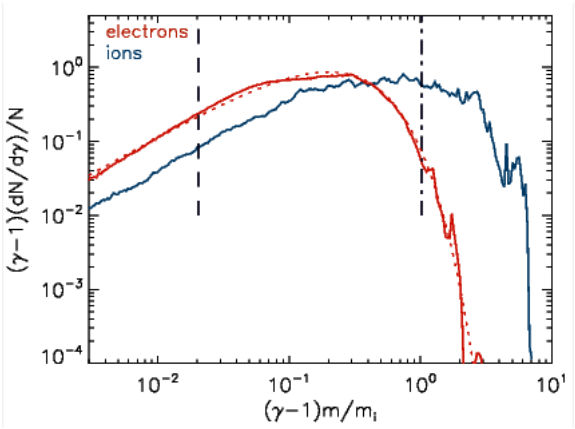

Figure 6.22: *Particle energy spectra in 1D run (red for electrons, blue for ions) in a region* $x/\lambda_{si} = (204-234)$ *downstream of the shock at* $x_{\rm sh}/\lambda_{si} \approx 239$ *at time* $t\Omega_{ci} = 163.6$ *(a). Energy axis is scaled with respective particle mass,* $m = m_e, m_i$*. Vertical dashed and dash-dotted lines mark initial bulk kinetic energies of the electrons and ions, respectively. The electron spectrum is fitted with a Maxwellian distribution (red thick dotted line).*

observed at $t\Omega_{ci} \sim 84.3$ (not shown), and it is qualitatively similar to the phase-space presented in Fig. 6.13 for the 2D out-of-plane run. As in the latter case, the energisation of particles in the upstream in extremely limited, and the majority of the ion-to-electron energy transfer takes place at the shock front and in the immediate downstream.

The particle kinetic energy spectra downstream of the shock at $x/\lambda_{si} = (204-234)$ are shown in Fig. 6.22. The ion spectrum shows again mainly relaxation around the mean ion energy and tends towards a 2D relativistic Maxwellian distribution. Electron distribution can also be approximated with a 2D Maxwellian. In the downstream, electrons' average Lorentz factor is $\langle \gamma_e - 1 \rangle / m_i \approx 0.0.17$, about 22% of the mean downstream ion Lorentz factor, $\langle \gamma_e - 1 \rangle / m_i \approx 0.78$. Energy equipartition is not reached also in this case. However, the energy transfer process is slightly more efficient than in 2D simulations (see Fig. 6.31 below. No signature of the positive feedback process is observed, even in this very long 1D run. Downstream of the shock ions carry $\sim 78.3\%$ of their initial kinetic energy per particle, $(\gamma_0 - 1)m_i c^2$, while electrons $\sim 16.7\%$. The fraction of energy transferred to electromagnetic waves is thus $\sim 5\%$. The electron heating also in this case proceeds above adiabatic compression, which is due to electron scattering off turbulent fields in the shock downstream.

6.4 Results of the in-plane setup

In this section I investigate a mildly relativistic shock in the setup with the upstream magnetic field lying in the plane of the simulation, $\boldsymbol{B_0} = B_y \hat{\boldsymbol{y}}$, thus $\varphi_B = 0°$ (see Fig. 6.1). I discuss the shock structure and particle acceleration and heating processes and compare them with the results obtained in Section 6.2.

6.4.1 The Shock Structure

In the case with the in-plane magnetic field configuration the shock structure quickly acquires its steady-state form and does not develop strong rippling features observed in the out-of-plane case. Because of that here I discuss only the nonlinear shock properties at a final simulation time, $t\Omega_{ci} = 84.3$.

The shock structure is presented in Fig. 6.23. The shock front is located at $x/\lambda_{si} \simeq 108$, indicating that it moves with the velocity $v = 0.41c$ that is smaller than the shock speed in the case with the out-of-plane magnetic field. The density jump is $n_2/n_1 \sim 3.2$. Both the slower shock velocity and the slightly larger density compression with comparison to the out-of-plane case are consistent with theoretical jump conditions in relativistic plasma with three degrees of freedom, in which the adiabatic index $\Gamma = 4/3$ [Plotnikov et al., 2018].

At the shock front, the fluctuations in density and electromagnetic fields can be observed together with corrugations in the shock surface. The latter develop at very early stages of the simulation and fast evolve into a long-wave rippling mode with $\lambda_{\rm rippl} \simeq 5\lambda_{si}$. They propagate along the mean magnetic field and their amplitude does not exceed $\sim \lambda_{si}$. The nature of the shock-front turbulence and ripples is different from the previously analysed case with the mean field $\boldsymbol{B_0}$ out of the simulation plane. In the present case, I ascribe these waves to the anisotropy in the ion temperature, $T_{\rm i\perp} > T_{\rm i\parallel}$, resulting from the ion reflection from the shock, as shown in panel Fig. 6.23e). The temperatures are defined here with respect to the mean magnetic field direction. In such conditions the Alfvén Ion Cyclotron instability is triggered, known to be a source of ripples in low Mach number shocks [e.g., Winske and Quest, 1988, Umeda et al., 2014, Lowe and Burgess, 2003]. Note that similar temperature-anisotropy instabilities on the Alfvén mode branch were found to generate magnetic field fluctuations in the front of relativistic pair shocks in Iwamoto et al. [2018]. The shock-front corrugations

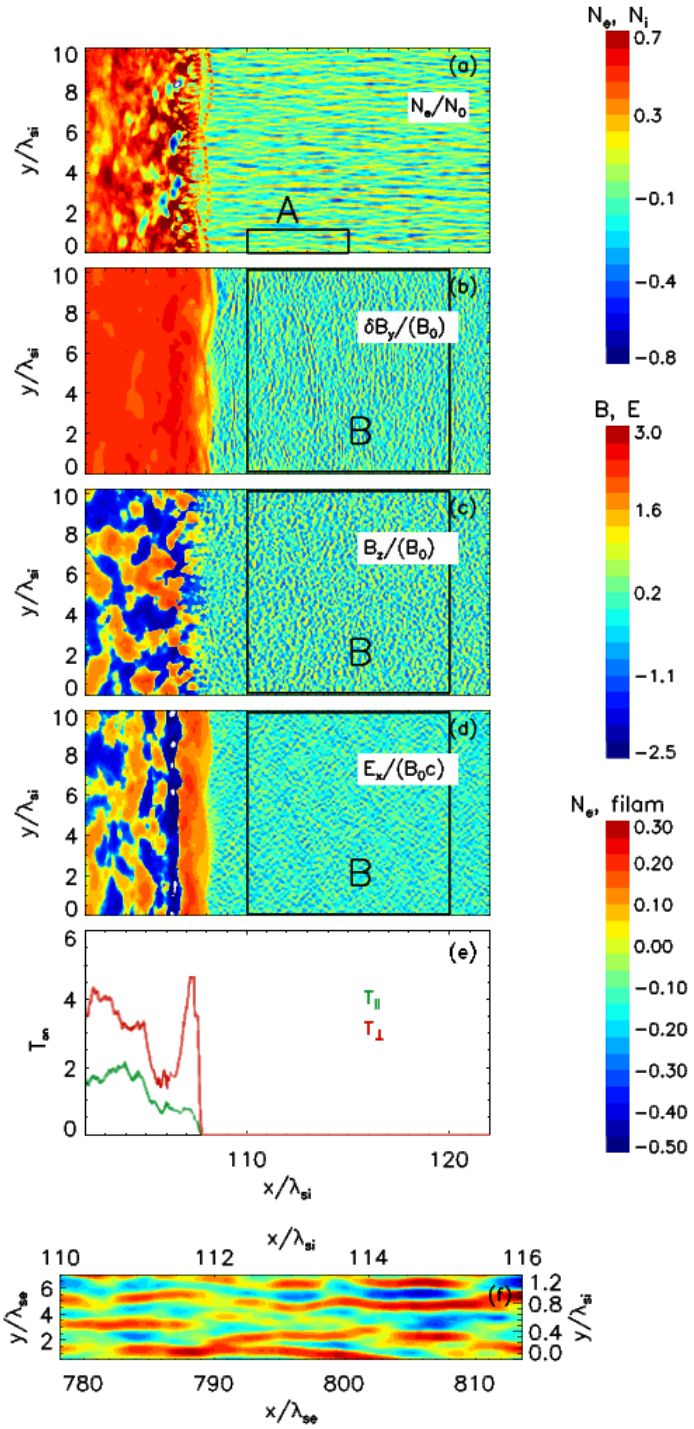

Figure 6.23: *Distribution of the normalised electron number density (a), B_y magnetic field fluctuations, δB_y (b), B_z magnetic field component (c) and E_x electric field (d) at the final stage of the simulation with $\varphi_B = 0°$, $t\Omega_{ci} = 84.3$. Logarithmic scalings are applied to density and field maps (see Fig. 6.5). Panel (e) shows the profiles of the ion temperature at the shock, differentiating between components parallel and perpendicular to the ambient magnetic field. Panel (f) shows a close-up of Region A in the electron density plot (a). Region B marked with squares in panels (b-d) for $x/\lambda_{si} = 110 - 120$ is chosen for the calculations of the Fourier power spectra presented in Fig. 6.26 (compare Fig. 6.9).*

and fluctuations are also a source of downstream turbulence, via the mechanism of the vorticity generation through a process similar to the Richtmyer-Meshkov instability [e.g., Mizuno et al., 2011, 2014].

6.4.1(a) Upstream Waves

One can see in Fig. 6.23b-d that short-scale oscillations are present upstream of the shock in all magnetic field components. These precursor waves are accompanied with long-wave electrostatic, E_x, wake-field (Fig. 6.23d). Fig. 6.24 shows the profiles of these fluctuations in the entire upstream region at time $t\Omega_{ci} = 84.3$, applying the same format as the one used in Fig. 6.12 for 2D out-of-plane simulation and in Fig. 6.18 in Sec. 6.3 for 1D run. Fig. 6.25 shows the enlarged view of the region $x/\lambda_{si} = (120 - 125)$, presenting also the fluctuations in the E_y and E_z electric field components.

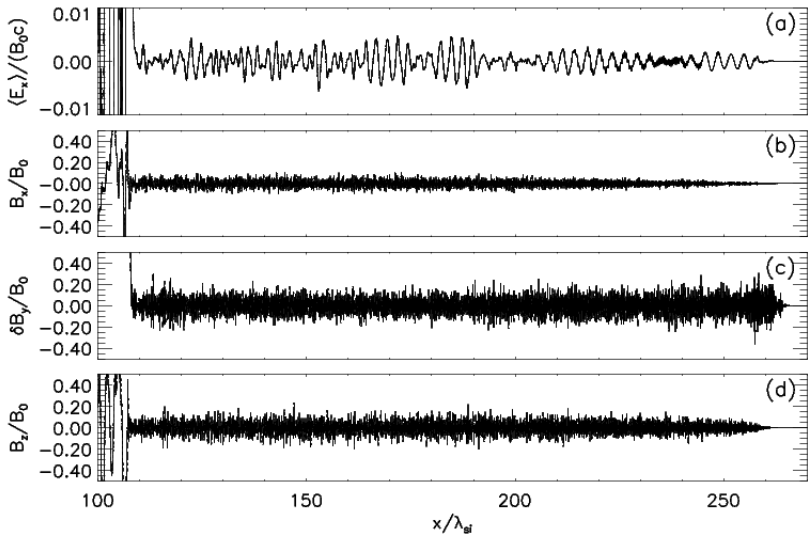

Figure 6.24: *Profiles along the shock normal of normalised upstream waves for simulation with the in-plane magnetic field configuration at time $t\Omega_{ci} = 84.3$. The electric field $\langle E_x \rangle$ is averaged over y-direction (a) and fluctuations in the magnetic field components, $B_y, \delta B_y = (B_y - B_0)$, and B_z are taken in the middle of the box along $y/\lambda_{si} = 6$ (b-d) (see also Fig. 6.12).*

Electromagnetic waves with the B_y component represent fluctuating magnetic fields parallel to the mean upstream magnetic field $\boldsymbol{B_0} = B_y\hat{\boldsymbol{y}}$ and perpendicular to the wave vector $\boldsymbol{k} = k_x\hat{\boldsymbol{x}}$. Similar in amplitude, the fluctuating E_z electric field component is perpendicular to both $\boldsymbol{B_0}$ and k_x and anti-correlates in phase with δB_y (see Fig. 6.25a). This wave is thus identified as an X-mode, linearly polarised along the direction of the mean upstream field. The wave with B_z and E_y electromagnetic field components of the same amplitude and correlated in phase (Fig. 6.25b) has fluctuating magnetic field

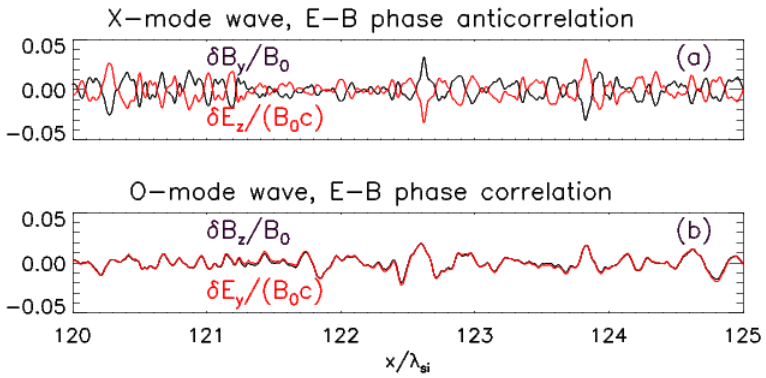

Figure 6.25: *Enlarged view of the region $x/\lambda_{si} = (120-125)$ shown in Fig. 6.24 demonstrating phase (anti)correlation between y and z components of the wave electromagnetic fields for the X-mode (a) and O-mode (b) waves. The wave amplitudes are normalised as in Fig. 6.24. The black and red lines show the magnetic field and the electric field components, respectively.*

perpendicular to $\boldsymbol{B_0}$ and the electric field oscillations along the ambient magnetic field. The wave is then an O-mode linearly polarised transverse wave with $\boldsymbol{k} = k_x\hat{\boldsymbol{x}}$.

The magnetic field fluctuation amplitudes are listed in Table 6.1, together with the results obtained in 1D and 2D out-of-plane simulations. As before, the amplitudes are averaged in the region located about $2\lambda_{si}$ from the shock, at $x/\lambda_{si} = 110-115$. Time evolution of the field amplitudes thus calculated is shown in Fig. 6.19 in Sec. 6.3. Both in Fig. 6.19 and in Table 6.1 I list the total amplitude of the magnetic field oscillations, $\delta B = \sqrt{\delta B_x^2 + \delta B_y^2 + \delta B_z^2}$, not differentiating between the X-mode and O-mode waves. Nevertheless, one can see in Fig. 6.24 that the amplitude of the X-mode wave, $\delta B_X/B_0 = \sqrt{\delta B_x^2 + \delta B_y^2}/B_0 \simeq 0.12$, is much larger than the amplitude of the O-mode wave, $\delta B_O/B_0 = \delta B_z/B_0 \simeq 0.08$. The total precursor wave amplitude, $\delta B/B_0 \simeq 0.15$, is also slightly smaller than the amplitudes obtained in my 2D run with the mean magnetic field out of the simulation plane and in 1D simulation.

As explained in Sec. 6.2.2(d), strong shock ripples generated in the 2D run with the out-of-plane magnetic field configuration cause the enhancement of the precursor waves amplitude to the level observed in 1D simulation. In the present case, I also see similar amplification by the ripples. This can be best noted in Fig. 6.23b, which shows the emission of the precursor waves in bunches, whose shapes correspond to the long-wave profiles of the rippling mode along the shock surface at a given time (note a weak oblique component that produces oscillations in B_x with $\delta B_x/B_0 \simeq 0.016$). However, the AIC instability-driven rippling mode is relatively weak and the in-phase bunching of the waves cannot fully overcome losses in the wave coherency due to random

inhomogeneities at the shock surface and the suppression of the wave amplitudes caused by thermal effects. Irrespective of that, the precursor wave amplitude is large enough to induce the wake-field and influence the particle acceleration and heating processes. As one can see in Fig. 6.19 the up8tream oscillations amplitude is roughly constant throughout the 2D simulation with the in-plane setup, which corresponds to an early formation of the shock ripples.

As already noted, the X-mode emission is consistent with the linear theory of the SMI. This theory also predicts that the emission of the X-mode waves is dominant over the emission of the O-mode waves [Wu and Lee, 1979, Lee et al., 1980, Melrose et al., 1984]. Nevertheless, the production of the O-mode waves was previously observed in 2D simulations of ultrarelativistic pair plasma shocks with the in-plane magnetic field setup [Iwamoto et al., 2018]. In that work the O-mode energy was observed to even exceed the X-mode energy at very small electron magnetizations, $\sigma_e \lesssim 10^{-2}$. As explained in that work, the O-mode results from the mode conversion from the X-mode generated in the turbulent shock transition. In the early stages of the shock evolution, the mean magnetic field is aligned along the y-axis, causing charged particle gyration in the $x-z$ plane and triggering the X-mode waves with δB_y. As plasma instabilities develop in the shock transition and generate fluctuations in B_z of amplitude comparable to B_0, the net magnetic field undulates also in the $y-z$ plane. X-mode waves produced by the SMI now have both δB_y and δB_z components. When propagating upstream of the shock in the unaltered magnetic field and maintaining their polarisation, the X-mode waves may be converted into the O-mode waves. In support that this interpretation is valid also in the case of my mildly relativistic shock, I note that the O-mode waves are produced with a small delay with respect to the X-mode waves. As one can see in Fig. 6.24c-d, the tip of the B_z wave is behind the tip of the B_y wave. This supports the notion that O-mode waves are generated after the shock front has developed large enough turbulence. Note that a relatively smaller amplitude of the O-mode waves with respect to the X-mode waves are compatible with a moderate level of the B_z fluctuations in the shock front, $\delta B_z/B_0 \sim 1$, in some regions (compare results for $\sigma_e \gtrsim 10^{-2}$ in Iwamoto et al. [2019]).

Fig. 6.26 shows Fourier power spectra of fluctuations in B_y, B_z, E_x, and the electron density in *Region B* marked in Fig. 6.23. These spectra can be compared to the spectra

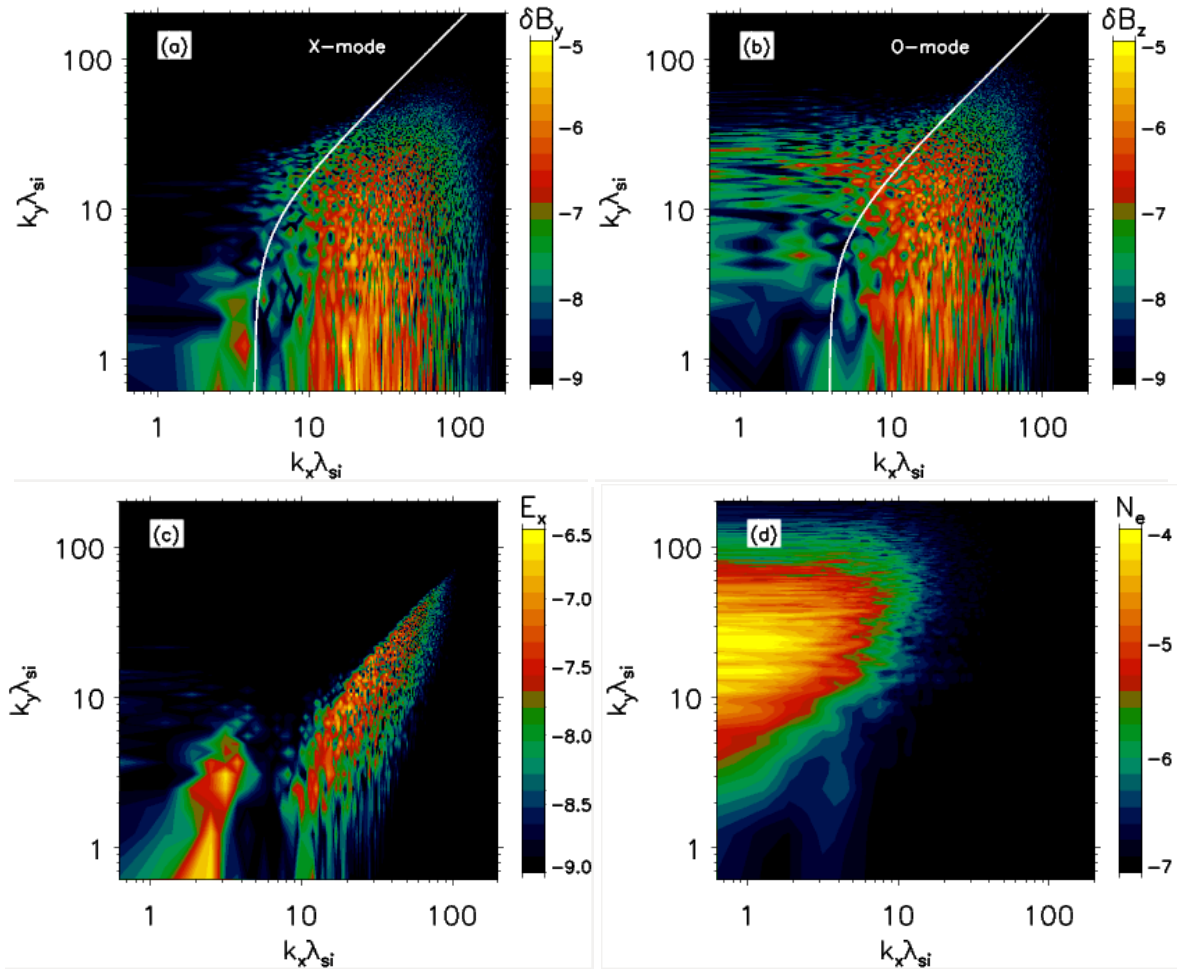

Figure 6.26: *Fourier power spectra for wave fluctuations in B_y (a) and B_z (b) magnetic field and E_x (c) electric field components and the electron density (d) for Region B at $x/\lambda_{si} = 110 - 120$ at time $t\Omega_{ci} = 84.3$ (see Fig. 6.23). The solid lines show the theoretical cutoff wavenumber for the X-mode (a) and the O-mode (b) waves.*

in Fig. 6.11 obtained for $\boldsymbol{B_0}$ out of the simulation plane. The cutoff wavenumber that is marked in the figure panels with white lines for the respective modes was estimated for O-mode waves in an analogous way as in the out-of-plane-case (see Sec. 6.2.1). The dispersion relation for these waves in the simulation frame is the same as for the electromagnetic wave in unmagnetized plasma, and it can be recovered from Eq. 6.3 by imposing $\sigma = 0$:

$$\omega^2 = k^2c^2 + \omega_{pe}^2 \tag{6.15}$$

which leads to the cutoff wavenumber for the ordinary mode:

$$k_x = \beta_{\rm sh}\Gamma_{sh}\sqrt{\frac{\omega_{pe}^2}{c^2} + k_y^2}\,. \tag{6.16}$$

Note that the wave power in the spectra for δB_y and δB_z is located to the right of the theoretical cutoff wavenumbers. The waves thus propagate upstream with the group velocity larger than the shock velocity, as expected. The wave-vector range of the precursor waves is similar to the range reported in the out-of-plane setup. These waves propagate predominantly with $k \approx k_x$, but an oblique component is also present, as observed in the field maps in Fig. 6.23.

As in the case of my simulation with the out-of-plane setup (Sec. 6.2.2(c)), also in the case with $\boldsymbol{B_0}$ in the simulation plane transverse density filaments are formed upstream of the shock. One can see in Figures 6.23a and 6.23e, that the amplitude of the filaments, $\delta N_e/N_0 \approx 0.5$ is much larger than in the previous simulation and they are mostly aligned in the x-direction, that corresponds to the dominant wave power at $k \approx k_y$ in Fig. 6.26d. As before, I interpret the origin of these structures by the parametric filamentation instability, the development of which is not disturbed here by the weak ripples at the shock. This again shows persistence of the coherent precursor waves in mildly relativistic shocks, albeit with smaller amplitude compared to the ultrarelativistic regime.

One can note in Fig. 6.23d that the wake-field is excited upstream of the shock, as in the case with out-of-plane magnetic field. Fig. 6.26c shows that the main signal is at $k \approx k_x \simeq 2\lambda_{si}^{-1}$ and also has an oblique component with $k\lambda_{si} \simeq 3$. This is consistent with the estimate in Equation 6.8. The average amplitude of these Langmuir modes is slightly less but still comparable to that observed in the simulation with the out-of plane magnetic field (compare Fig. 6.24a with Fig. 6.12a). In fact, noting from Figures 6.26a-b that a typical wavenumber of the precursor waves is $k \sim 20\lambda_{si}^{-1} \approx 2.8\lambda_{se}^{-1}$, one can apply the procedure used in Sec. 6.2.3(a) and combine the wave-vector with the dispersion relation for the dominant X-mode waves given by Equation 6.15 to obtain a typical wave frequency:

$$\frac{\omega}{\omega_{pe}} \sim 3.2. \tag{6.17}$$

Using Equation 6.10 with $\delta B/B_0$, thus adding the contributions from the X- and O-modes, one can estimate the strength parameter

$$a \simeq 0.21, \tag{6.18}$$

and calculate the amplitude of the wake-field (Eq. 6.13):

$$\frac{\langle E_x \rangle}{B_0 c} \simeq 5 \times 10^{-3}. \tag{6.19}$$

Therefore, the wake-field in the simulation with the in-plane magnetic field configuration should exert similar effects on the upstream plasma as observed in the case with an angle between magnetic field and shock normal $\varphi_B = 90°$. I will show in the next section that this indeed is the case.

For comparison with the out-of-plane case I also present in Fig. 6.27 the $\omega' - k'$ plot for waves in B_y in a region located at $x/\lambda_{si} = 77 - 87$. The shock is located at $x/\lambda_{si} \approx 70$. The Fourier-Laplace analysis was brought forth in the same way as for the out-of-plane case. The theoretical dispersion relation calculated in Sec. 4.1 is overplotted with white dots.

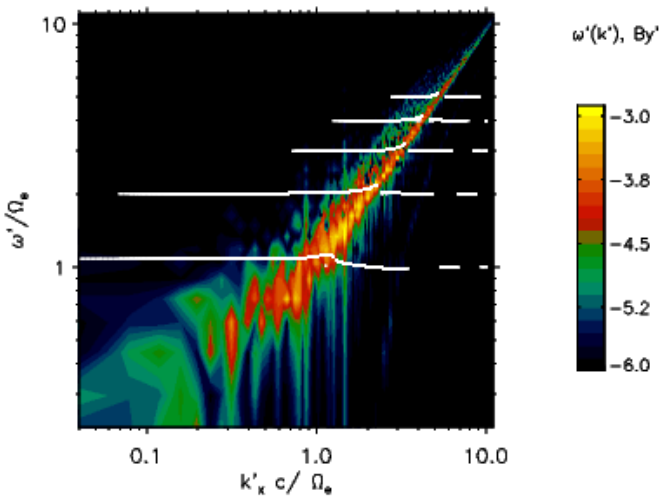

Figure 6.27: *Fourier power spectrum of B_z magnetic field oscillations in $\omega - k_x$ space taken along $y = 5\lambda_{si}$ in a region located at $x/\lambda_{si} = 77 - 87$. The shock is located at $x/\lambda_{si} \approx 70$. The time interval is $0.562\,\Omega_{ci}^{-1} \simeq 28.1\,\Omega_{ce}^{-1}$, starting from time $t\Omega_{ci} \simeq 56.23$. The analysis is performed in the* upstream *plasma rest frame. The angular frequency, ω', is normalised with the electron cyclotron frequency, Ω_{ce}, and the wave-vector, k'_x, by Ω_{ce}/c. Overlaid with white dots is the theoretical dispersion relation derived from the linear analysis presented in Sec. 4.1.*

The region choosen for the analysis of the wave power spectra is close to the shock and direct comparison can be drawn with Fig. 6.8b for $\varphi_B = 90^o$. Similarly to that case, the close-shock region is influenced by the the effects of the AIC-driven shock corrugations and by the nonlinear evolution of the wave modes. This effect can be noted in the low frequency and wavenumber part of the plot. Overall though, as for

the out-of-plane case, the spectrum retains its qualitative consistency with the theory of the electron SMI.

6.4.2 Particle Energisation in the In-Plane Case

6.4.2(a) Upstream Particle-Wave Interactions and Downstream Spectra

The phase-space distributions of electrons and ions and the mean particle kinetic energy profiles in the upstream and across the shock are presented in Fig. 6.28. One can see that results for the in-plane case are very similar to that shown in Fig. 6.13 for the simulation with $\varphi_B = 90°$. This is because the amplitudes of the precursor waves and wake-field are compatible in both runs. Therefore, essentially the same physical mechanisms of particle interactions with the upstream waves operate here.

In particular, the electrons can be accelerated by strong wake-field waves, that are observed to propagate toward the shock also in this case (see Fig. 6.29), and reach energies in excess of $\gamma_e \sim 20$. In effect, the anisotropy in $p_{xe} - x$ is produced. As I will show below, the SSA process works as well, though the corresponding anisotropy along the motional electric field in the $p_{ze} - x$ cannot be observed in my 2D simulation. The bulk energy gain of electrons before they reach the shock is again about 5% of their initial kinetic energy, so that electrons and ions are far from the energy equipartition upstream of the shock.

Fig. 6.30 shows downstream particle spectra. As in the case with the out-of-plane magnetic field, the ions are in the process of thermalization around their mean energy and the reflected particles undergo SDA at the shock. Electron distribution is close to the combination of two 3D Maxwellians, each described by:

$$f(\gamma-1)d\gamma \propto \sqrt{(\gamma-1)}\, e^{-\frac{m_e c^2}{kT_e}(\gamma-1)} \tag{6.20}$$

and where the two peaks are very close together. The distribution can be also approximated by a single 3D Maxwellian, but the two Maxwellians provide a slightly better fit. Also in the present case a limited-range supra-thermal component in the electron spectrum is present with the power-law spectral index $p \simeq 2.1$, as shown in inset (b) of Fig. 6.30. The slope of the supra-thermal component is similar to that in the out-of-plane simulation.

One can see that the level of electron-ion coupling downstream of the shock in the

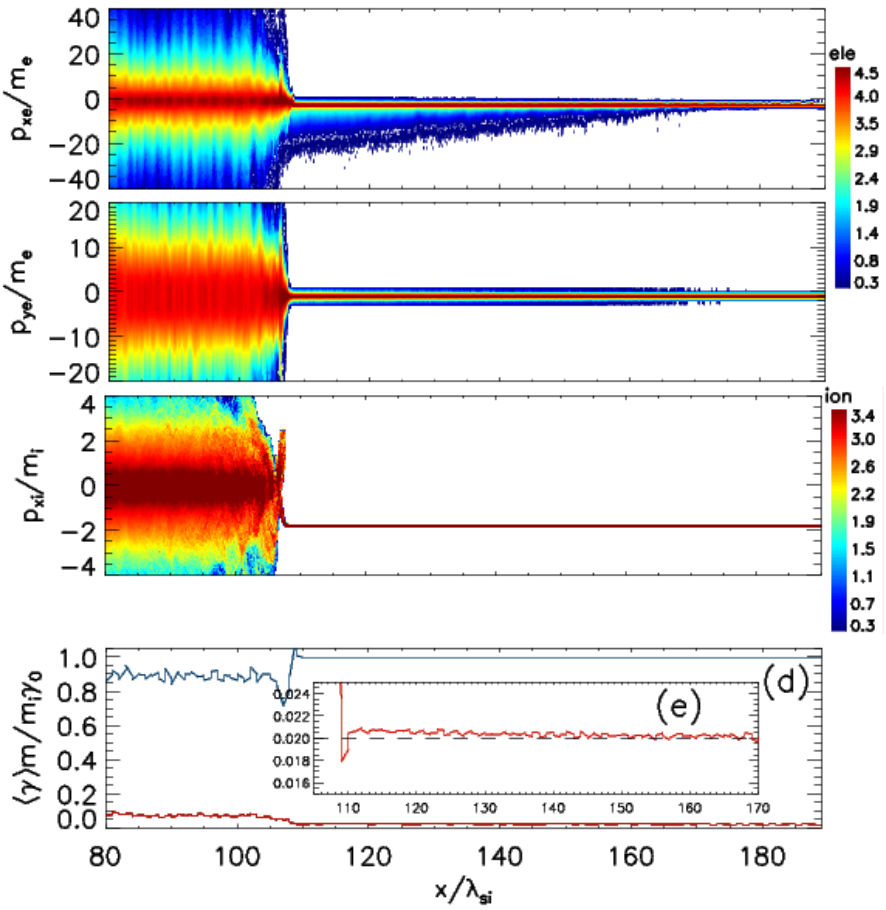

Figure 6.28: *Phase-space distributions map for electrons along x axis (a) and along y axis (b), and distributions map for ions along x axis (c) in the upstream region, at time t = 84.3* Ω_{ci}^{-1}*; mean particle energy (blue for ions and red for electrons) in units of the ions upstream bulk energy (d) and close up of the electron mean particle energy in the vicinity of the shock (e). Phase-space distributions map for electrons along x axis (a) and along y axis (b), and distributions map for ions along x axis (c) in the upstream region, at time t = 84.3* Ω_{ci}^{-1}*; mean particle energy (blue for ions and red for electrons) in units of the ions upstream bulk energy (d) and close up of the electron mean particle energy in the vicinity of the shock (e).*

in-plane case is far from the energy equipartition, as in the setup with $\varphi_B = 90°$. To facilitate a direct comparison, in Fig. 6.31 I once again show the electron spectra for both 2D runs and also for 1D simulation.

In the case with $\varphi_B = 0°$, the average Lorentz factor of electrons $\langle\gamma_e - 1\rangle/m_i \approx 0.13$ is 16% of that of the ions, $\langle\gamma_e - 1\rangle/m_i \approx 0.77$, the electrons carry $\sim 12.6\%$ of the initial ion kinetic energy per particle and 77,2% stays in the downstream ion energy. The ion-to-electron energy transfer is thus slightly larger in the in-plane case, but comparable in both 2D runs. In 1D simulations the coupling is slightly stronger, the electrons gaining 16,8% of the ion energy. Nevertheless, in all cases the electrons and ions are weakly coupled.

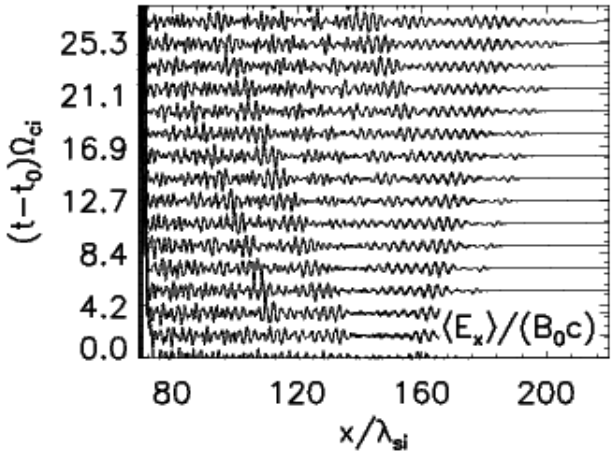

Figure 6.29: *Stack plot of the averaged wake-field waveforms, $\langle E_x \rangle/(B_0 c)$, upstream of the shock, starting at time $t_0\Omega_{ci} = 56.2$ and ending at $t_{\max}\Omega_{ci} = 84.7$, for the in-plane case. The profiles are shifted so that the shock at all times is located at the left side of the figure at $x/\lambda_{si} \simeq 70$.*

6.4.2(b) Electron Energisation Mechanisms

As in Sec. 6.2.3(c), I describe the electron heating and acceleration processes by analysing average quantities derived from sample of traced particles. Fig. 6.32 illustrates the main electron energisation phases in a format similar to that in Fig. 6.16. In the present case I split the work done by the electric field into components parallel and perpendicular to the *local* magnetic field (see caption of Fig. 6.32).

Qualitatively, in the setup with the in-plane $\boldsymbol{B_0}$ the electron energisation proceeds with the same phases as described for the case with $\varphi_{\rm B} = 90°$. On the approach toward the shock the particles interact with the wake-field, and those that later can gain significant energies are decoupled from the bulk flow at an interaction with strong waves emitted by the ripples. A strong pull by the E_x electric field and acceleration in the motional electric field, E_z, results in an initial energy gain that is due to work done by the perpendicular electric field components. The magnetic moment increases. This is a step at time $t = t_a$ (Fig. 6.32a). Note, that gyration in the magnetic field is in the $x-z$ plane and the $\boldsymbol{E}\times\boldsymbol{B}$ drift motion due to the E_x field is out of the simulation plane, $-E_x B_y \hat{\boldsymbol{z}}$, and is not visible through particle trajectories.

Upon entering the shock the particles undergo adiabatic heating. The magnetic moment stays roughly constant until the electrons come close to the overshoot at time t_b (Fig. 6.32b), when the magnetic moment starts to increase and particles gain a significant amount of energy through the work of the y-component of the parallel

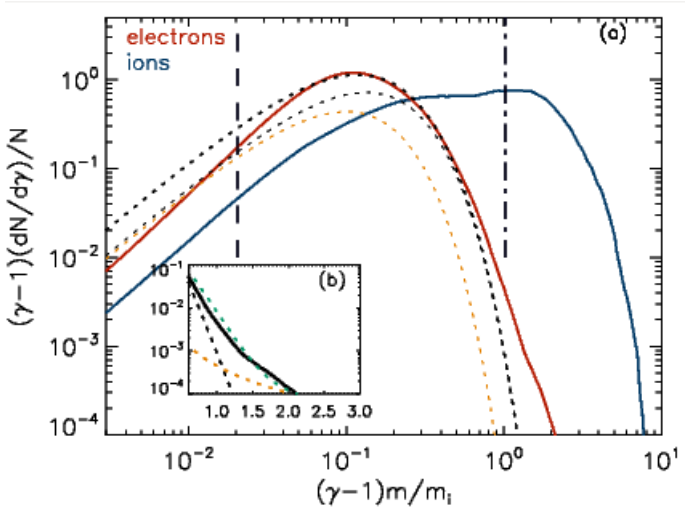

Figure 6.30: *Particle energy spectra (red for electrons, blue for ions) in a region $x/\lambda_{si} = 87-97$ downstream of the shock at $x_{sh}/\lambda_{si} \approx 107$ at time $t\Omega_{ci} = 84.3$ (a) and close-up of the high-energy part of the electron spectrum (b). Dotted line in panel (a) shows relativistic 3D Maxwellian fit to the electron spectrum (see Fig. 6.15).*

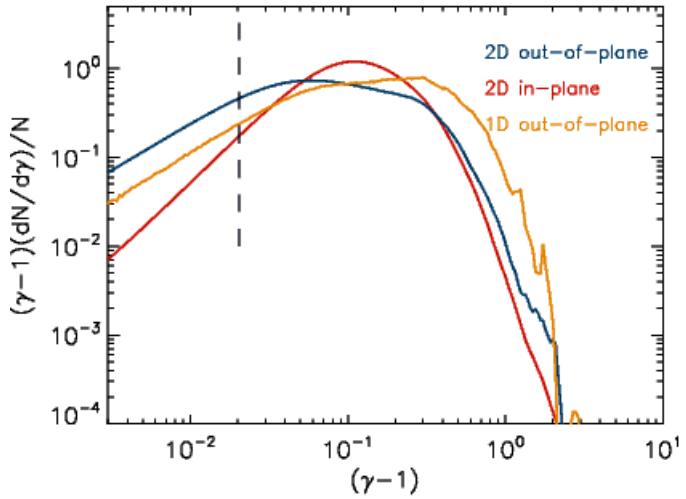

Figure 6.31: *Comparison of the electron spectra downstream of the shock obtained in 2D (blue line for $\varphi_B = 90°$, red line for $\varphi_B = 0°$) and 1D simulations (orange line). The spectra are calculated in a region $5\lambda_{si} - 15\lambda_{si}$ downstream of the shock front (compare Figs. 6.15 and 6.30).*

electric field. The inset in panel (b) shows that $B_y\hat{\boldsymbol{y}}$ magnetic-field-aligned electric fields exist everywhere along the magnetic overshoot. Their structure in a larger portion of the overshoot and the region downstream is shown in Fig. 6.33.

One can note that in the overshoot density of ions is much larger than that of electrons. This creates strong charge-separation electric fields. The ion density increase results from their deceleration during a coherent reflection in the shock-compressed

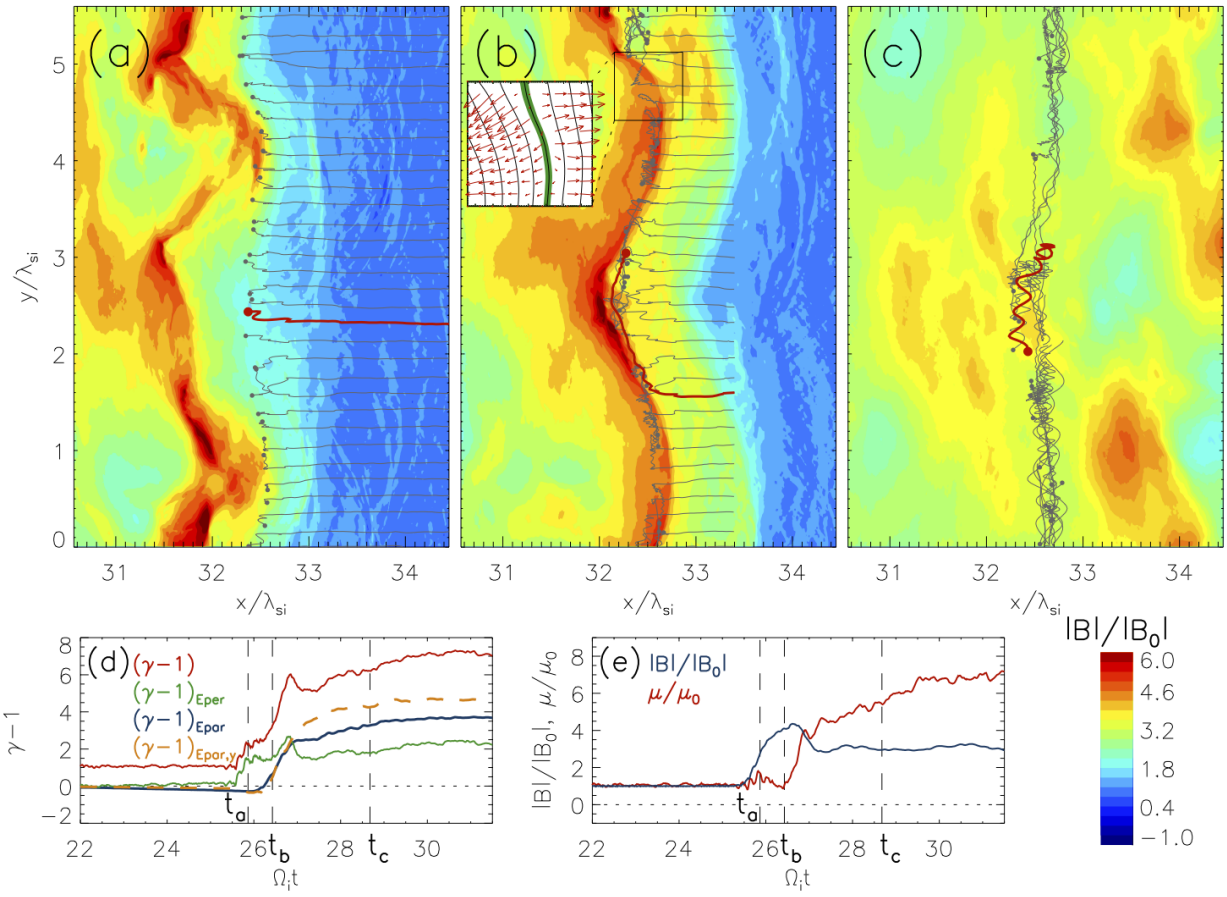

Figure 6.32: *Trajectory segments of sample electrons (a-c), time evolution of the average kinetic energy and acceleration rates (d) and the magnetic moment and the magnetic field profile (e) in the simulation with $\varphi_B = 0°$e. The format is the same as in Fig. 6.16, except that the total magnitude of the magnetic field strength, $|B|/B_0$, is shown in panels (a-c) and (e) and the acceleration rates are split into components parallel, $(\gamma-1)_{E_{par}} = \int_{t_0}^{t_1} q_e \boldsymbol{v}\cdot\boldsymbol{E}_{\parallel}/(m_e c^2)dt$ (blue line), and perpendicular $(\gamma-1)_{E_{per}} = \int_{t_0}^{t_1} q_e \boldsymbol{v}\cdot\boldsymbol{E}_{\perp}/(m_e c^2)dt$ (green line) to the magnetic field. For $(\gamma-1)_{E_{par}}$ I also show its y-component with orange line. The inset in panel (b) shows zoom-in of the fields configuration in a region marked with a square box, where red arrows present the in-plane electric field, black lines the contours of the A_z-component of the vector potential (displaying the in-plane magnetic field lines), and the the green thick line shows the region with strong electric field component along the magnetic field.*

magnetic field. The electrostatic field is thus associated with the cross-shock potential that reflects the ions and accelerates the electrons toward downstream. In a laminar shock the cross-shock potential electric field is directed toward its normal, so in our geometry this electric field would lie along the x-coordinate and flip sign across it. This is visible in Figure 6.33 upstream and downstream from the overshoot (red arrows). However, in the overshoot the electric field structure forms a complex set of thin and warped filaments that at some locations are at a large angle with respect to the y-axis.

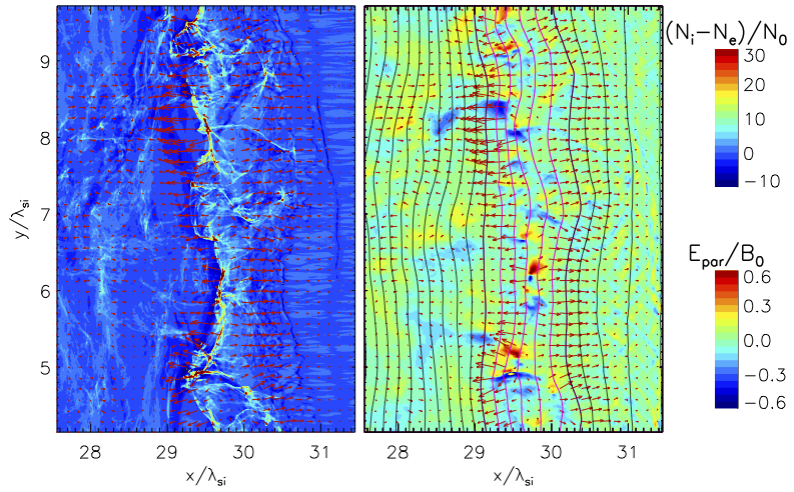

Figure 6.33: *Distribution of the normalized charge density (left panel) and the electric field component aligned with the magnetic field (right panel) at time $t\Omega_{ce} = 24.2$ and a portion of the box around the shock overshoot. Red arrows show the in-plane electric field. Magnetic field lines in the right panel are shown with black and magenta lines, the latter highlighting the region, in which $E_{\rm par}$ has a substantial amplitude.*

The charge-separation field thus acquires a component along the magnetic field, that is largely in the y-direction. Electrons that are able to move freely along magnetic field lines can be efficiently accelerated in the co-aligned electric fields (see a trajectory of sample electron marked with red line in Fig. 6.32b).

Electrostatic fields with components transverse to the shock normal often occur in non relativistic systems. The electrons that are accelerated in the cross-shock potential can excite two-stream instabilities while streaming across the background electrons or ions [Thomsen et al., 1983, Goodrich and Scudder, 1984]. Similar processes can occur here. However, one can see in Fig. 6.33 that the overshoot structure is modulated on large scales by the shock ripples. The presence of modulations at scales of the ion skin depth and smaller suggests that some other instabilities may also operate in the overshoot. The coupling between these unstable modes is difficult to disentangle. I only note that the effect of the $E_{||}$ fields is specific to the in-plane magnetic field configuration under study. The strength of this electric field component is much larger than that typically observed in non relativistic shocks, and may be due to specific conditions in our mildly relativistic and magnetized shock. Also note that the adiabatic heating works on top of the processes discussed. However, it is difficult to separate this component from the other contributions in our in-plane setup.

After crossing the overshoot the average kinetic energy of the particle sample and

the magnetic moment keep increasing, despite the magnetic field decompression. As in the case with $\boldsymbol{B_0}$ out-of-plane, this non adiabatic acceleration is due to either gyro-resonant or stochastic scattering of the electrons off downstream turbulent fields created due to the shock front ripples (Fig. 6.32c). Note, that magnetic-field aligned electric fields persist in an extended region past the overshoot, providing scattering centres.

CHAPTER 7
SUMMARY AND CONCLUSIONS

In this dissertation I investigate with PIC simulations the shock structure, production of plasma instabilities, and associated particle acceleration and heating in mildly-relativistic magnetized shocks. The main application of this study is in the physics of AGN jets, that are observed to be sources of high-energy electromagnetic emission and also CR particles. In this context the focus of this work is on conditions typically assumed in the internal shock scenario of the electromagnetic emission production. I therefore assume the shock Lorentz factor of $\Gamma_{sh} \simeq 2$ and plasma magnetization, $\sigma = 0.1$. At this magnetization the shocks are mediated through particle reflection off the shock-compressed magnetic field and the flow energy dissipation processes involve emission of strong coherent electromagnetic radiation. Nevertheless, mildly-relativistic shocks in this parameter regime have been poorly explored and only with very-low-resolution PIC simulations, that indicated a low efficiency of particle energisation processes and a resulting very weak proton-electron coupling. However, it has been recently noticed that an appropriate scrutiny of the electromagnetic shock structure requires sufficiently high numerical resolution. Only such studies can properly quantify the amplitude of the precursor waves and their interactions with particles. The aim of this thesis is to re-assess the physics of mildly relativistic magnetized shocks with kinetic PIC simulations that have unprecedentedly high-resolution and in addition take into account large-scale effects related to the proton gyration at the shock and the excitation of the corrugations along the shock surface. This is to investigate the applicability of the WFA model in AGN jets for the problem of high-energy CR origin and also to evaluate a realistic level of the proton-to-electron energy transfer in the shock. The study is performed for shocks in plasma composed of electrons and ions, without a positron content. As relativistic shocks are typically superluminal, my simulations investigate strictly perpendicular shocks. The geometry of the simulations is 2D because 3D large-scale high-resolution studies are at present not feasible from the computational side. However, to evaluate realistic 3D physics I probe two different configurations of the mean magnetic field with respect to the simulation plane, namely the out-of-plane and the in-plane field orientation.

My results show that the SMI operates in mildly relativistic shocks in agreement

with theoretical predictions and produces coherent emission of upstream-propagating electromagnetic waves. As observed in Iwamoto et al. [2017, 2018] for ultra relativistic shocks, the amplitude of these precursor waves in high-resolution studies in the mildly relativistic regime is much larger than the amplitude obtained at low resolutions. The strength of the waves is nevertheless much smaller than in high-Γ_{sh} shocks. However, the waves continue to persist and their amplitudes reach finite moderate level that in 2D is comparable to that in 1D simulations. This effective wave amplification overcomes destructive effects of the inhomogeneous shock surface and the temperature of the inflowing plasma and is due to the shock-front corrugations. The shock ripples appear for both configurations of the mean magnetic field, though their generation mechanisms differ in each case – it is the process described by Burgess and Scholer [2007] for $\varphi_B = 90^o$ and the AIC temperature-anisotropy instability in the case with $\varphi_B = 0^o$. In each case the ripples heavily influence the upstream plasma. Their presence is also essential for the electron acceleration and heating processes.

In the case with the out-of-plane mean magnetic field the precursor waves are of the X-mode type. The shock ripples cause them to be on average emitted at oblique angles to the shock normal. The ripple structure with strong plasma compressions enables the wave amplification. The AIC-generated shock front corrugations in the in-plane case are of slightly lower amplitude, and the waves are mostly propagating along the shock normal with only a weak oblique component. The presence of magnetic field turbulence in the shock leads in this case to the generation of the O-mode waves, in addition to the dominant X-mode waves. For each magnetic field configurations studied I observe the production of density filaments upstream of the shock via the parametric filamentation instability. Also in each case the electrostatic Langmuir wave modes – the wakefields – are excited in the upstream plasma.

It has been suggested that the wakefield acceleration in ultrarelativistic shocks may account for the production of highly energetic particles up to the UHECRs energy range through nonlinear collapse of the waves [Lyubarsky, 2006, Hoshino, 2008, Iwamoto et al., 2017, 2018, Iwamoto et al., 2019]. In the mildly relativistic shocks, the shock ripples generate at times stronger precursor wave emission that results in nonlinear wakefield amplitudes. The nonlinear processes of FRS are then triggered, producing downstream-propagating wakefields that accelerate electrons through the

phase-slippage effect combined with SSA [Hoshino, 2008]. However, the WFA is less efficient than in the ultra relativistic regime and only few particles become significantly energized close to the upstream bulk energy of ions in the upstream precursor wave region. In result, in contrast to ultrarelativistic shocks, the electrons and ions do not reach equipartition by the time they arrive to the vicinity of the shock.

The ion-to-electron energy transfer is comparable in both 2D simulations. In both cases it is far below equipartition, with electrons on average carrying $\sim 11\% - 13\%$ of the initial ion kinetic energy per particle. However, it is still much in excess of $m_e/m_i = 2\%$, for the assumed $m_i/m_e = 50$. The majority of the energy transfer takes place in the shock and downstream and electron heating proceeds beyond adiabatic compression at the shock. Resulting steady-state downstream electron energy spectra are close to thermal distributions, although narrow-energy-range supra-thermal power-law components are also present. The presence of the shock rippling is again crucial for electron energisation processes. Strong waves emitted by the shock ripples close to the shock excite wakefields that are able to effectively decouple a particle from the bulk flow. These particles can then experience strong acceleration in the electrostatic field in the turbulent rippling zone. This non-adiabatic energisation phase mediated by the shock corrugations is a necessary step to subsequent acceleration in the shock. To my knowledge, such process has not previously been reported in the literature.

In the setup with the out-of-plane magnetic field electrons crossing the shock ramp reside in the overshoot, wherein they experience adiabatic heating. Here some particles that underwent significant acceleration in the rippled shock front now have gyro-radii comparable to scale of the downstream turbulent field, that is set by the ripples' evolution. They can gain further energies via gyro-resonant interactions with the turbulence. Stochastic second-order Fermi-like inelastic scattering also takes place, with some particles reaching supra-thermal energies. Similar processes shape the downstream energy spectra in the in-plane magnetic field case. Additional significant energisation for this field configuration takes place in the shock overshoot, where the charge-separation electric fields associated with the cross-shock potential and modified by the shock ripples form a peculiar structure of complex thin and warped filaments. In effect, the electric fields acquire magnetic-field-aligned component, facilitating electron acceleration.

My studies underline a critical role of the shock front rippling in forming the shock structure and facilitating the electron heating and acceleration processes. Such effects have not been reported so far for relativistic shocks. Sironi et al. [2013] observed the shock corrugations generated in the mechanism of Burgess and Scholer [2007] in their simulations of perpendicular high Lorentz factor shocks. They showed that the rippling occurs only in a limited range of plasma magnetization, $3\times10^{-4} \lesssim \sigma \lesssim 10^{-1}$, and at other values of σ it is suppressed by too high a temperature of electrons heated in the upstream. For $\sigma \leq 10^{-4}$ the electrons are heated in the region of the Weibel instability filaments, while for $\sigma > 0.1$ in the SMI-mediated precursor. One can expect that the ripples in the mildly relativistic shocks can similarly be suppressed at low magnetizations, since the Weibel instability is important for the shock formation down to trans-relativistic shock velocities [e.g., Kato and Takabe, 2010]. On the other hand, at magnetizations higher than $\sigma \approx 0.1$, one does not expect that the precursor wave emission be stronger than in the case of $\sigma = 0.1$ analysed here [see Iwamoto et al., 2019], so that the rippling may survive in the conditions of higher magnetizations. The same argument should hold for the AIC-instability-generated corrugations.

The simulations presented in this thesis are 2D, and the persistence of the obtained results in realistic 3D systems should be discussed. As my simulations show that intense coherent precursor waves are generated by the SMI irrespective of the magnetic field configuration, one can expect that this mechanism will excite the waves also in 3D. In a three-dimensional setup one should expect that both the X-mode and O-mode waves are emitted by the shock, but the efficiency of the ordinary mode emission is difficult to estimate for the 3D configuration. The source of instabilities in the shock transition region that enable the generation of the O-mode is the gyration of particles at the shock front. As this gyration motion in 3D is expected to be less coherent than in the in-plane 2D simulations, one may presume that O-mode emission is less efficient in the 3D configuration [Iwamoto et al., 2018]. Recent multidimensional simulations of ultra relativistic shocks in pair plasmas carried out by Plotnikov and Sironi [2019] showed that at high $\sigma_e \gtrsim 1$ (recall that here $\sigma_e = 5.2$ is assumed) the physics of the precursor wave emission in 3D is better represented with the out-of-plane 2D model. This result should in principle hold in the electron-ion plasma, since the emission mechanism of the SMI waves in this case is the same as in the pair plasma. However, as demonstrated

in this thesis, the precursor wave strength and structure in mildly relativistic shocks is significantly influenced by the shock ripples. The survival of the rippling structure observed in the out-of-plane simulation in the 3D regime is not assured. This is because the Burgess and Scholer [2007] mechanism requires a suppression of the fluctuations parallel to the main magnetic field that might be difficult to achieve in 3D. Nevertheless, because the ripples generated through the AIC instability in the in-plane setup amplify the precursor waves to amplitudes comparable to that in the $\varphi_B = 90^o$ case, similar strength of the precursor waves can be expected in 3D.

Similar conclusion should be valid to what concerns the particle energisation efficiency. For both field configurations studied similar processes operate to heat and accelerate electrons and thermalize the ions. In 3D, a restriction that cross-field diffusion is suppressed in the in-plane configuration is waived [Jokipii et al., 1993], and thus gyroresonant or stochastic electron scattering may proceed even more efficiently to generate high-energy particles. On the other hand, the coherency of the precursor waves in 3D should rather not be greater than in lower-dimensionality simulations. As a consequence, the particle acceleration efficiency in 3D is expected to be at best the same as observed in 2D simulations. In result, I do not anticipate the possibility to obtain a stronger ion-electron coupling in three-dimensional studies. Note that the level of the coupling does not significantly depend on the superluminal shock angle in ultrarelativistic shocks [Sironi and Spitkovsky, 2011], in which the energy transfer occurs in the turbulent precursor. Future studies need to verify whether the effects of the shock rippling can enhance the coupling at angles lower than the strictly perpendicular to the shock normal.

The absence of energy equipartition between ions and electrons has important implications when one considers the astrophysical application of this result. Previous works concerning internal shock model for blazar jets require energy equipartition between the two species to reproduce blazars SED via leptonic models [see, e.g. Spada et al., 2001a,b]. Copious electrons naturally explain large luminosities of blazars. If the equipartition is not reached, then significant amount of energy is held by ions. It needs to be checked if and under which conditions the level of the electron-ion coupling reported in this work can be reconciled with the observed γ-ray luminosities of blazars. A modeling needs also to account for the observed X-ray spectra. As shown in Sikora

et al. [2013] under the assumption of strong coupling, the observed 2-10 keV spectral slopes of blazars can be explained in the external radiation Compton (ERC) mechanism of γ-ray production only if electrons are efficiently cooled down at sub-parsec distances from the accretion disk or the spectra are dominated by the synchrotron self-Compton (SSC) component up to at least 10 keV, though the SSC model is less favoured in blazar modeling. These conclusions may be different for the the lower-level coupling observed here if mildly relativistic and magnetized shock conditions prevail in the AGN jet emission sites. The ion-electron coupling also plays a role in estimating the fraction of pairs-vs-ions in the jet [see, e.g., Sikora et al., 2013].

Recent observations by the IceCube Collaboration reported the detection of a high-energy neutrino events correlated with the flaring blazar TXS 0506+056 [Aartsen et al., 2018]. This result prompts to exclude pure pair plasma composition of jets, at least for this particular source, and it points towards the presence of protons in these sources. My results show that high-energy protons that produced the IceCube neutrinos could not be accelerated via WFA or DSA in a magnetized mildly relativistic shock in the jet. However, in the plasma composed of electron-positron pairs with the proton content, in some conditions an additional process may operate that accelerates electrons and positrons. Reflected ions gyrating in the shock emit left-handed elliptically polarized magnetosonic waves with frequencies that are harmonics of the ion cyclotron frequency (the ion SMI). If the spectrum of the ion-emitted waves has enough power at high harmonics at and above the cyclotron frequencies of positrons and electrons, then pair particles traversing the shock can be accelerated to non-thermal energies through resonant relativistic synchrotron absorption of the magnetosonic waves [Hoshino and Arons, 1991]. In ultrarelativistic shocks this mechanism was demonstrated to be very efficient in accelerating positrons [Hoshino and Arons, 1991, Hoshino et al., 1992]. Non-thermal electrons are also created, albeit in a less efficient way because of the left-handed wave polarization of the ion waves [Amato and Arons, 2006, Stockem et al., 2012]. Therefore, also in mildly relativistic shocks one can expect similar processes to operate to increase the coupling between leptons and protons and possibly make the leptonic models capable of explaining the blazar emission. New high-resolution and large-scale PIC simulation studies are necessary to investigate the mildly relativistic scenario in ion-pair plasmas.

REFERENCES

A. Aab et al. Search for photons with energies above 10^{18} eV using the hybrid detector of the Pierre Auger Observatory. Journal of Cosmology and Astroparticle Physics, 2017(4):009, April 2017a. doi: 10.1088/1475-7516/2017/04/009.

A. Aab et al. A Targeted Search for Point Sources of EeV Photons with the Pierre Auger Observatory. ApJ, 837(2):L25, March 2017b. doi: 10.3847/2041-8213/aa61a5.

M. G. Aartsen et al. Neutrino emission from the direction of the blazar TXS 0506+056 prior to the IceCube-170922A alert. *Science*, 361(6398):147–151, July 2018. doi: 10.1126/science.aat2890.

R. U. Abbasi et al. Search for Ultra-High-Energy Neutrinos with the Telescope Array Surface Detector. *arXiv e-prints*, art. arXiv:1905.03738, May 2019.

H. Abdalla et al. A very-high-energy component deep in the γ-ray burst afterglow. Nature, 575(7783):464–467, November 2019. doi: 10.1038/s41586-019-1743-9.

V. A. Acciari et al. Teraelectronvolt emission from the γ-ray burst GRB 190114C. Nature, 575(7783):455–458, November 2019a. doi: 10.1038/s41586-019-1750-x.

V. A. Acciari et al. Observation of inverse Compton emission from a long γ-ray burst. Nature, 575(7783):459–463, November 2019b. doi: 10.1038/s41586-019-1754-6.

M. Ackermann et al. Detection of the Characteristic Pion-Decay Signature in Supernova Remnants. *Science*, 339(6121):807–811, February 2013. doi: 10.1126/science.1231160.

F. Aharonian et al. Primary particle acceleration above 100 TeV in the shell-type supernova remnant RX J1713.7-3946 with deep HESS observations. A&A, 464(1): 235–243, March 2007. doi: 10.1051/0004-6361:20066381.

J. Aleksić et al. Measurement of the Crab Nebula spectrum over three decades in energy with the MAGIC telescopes. *Journal of High Energy Astrophysics*, 5:30–38, March 2015. doi: 10.1016/j.jheap.2015.01.002.

D. Allard, E. Parizot, and A. V. Olinto. On the transition from galactic to extragalactic cosmic-rays: Spectral and composition features from two opposite scenarios. *Astroparticle Physics*, 27(1):61–75, February 2007. doi: 10.1016/j.astropartphys.2006.09.006.

R. Aloisio, S. Matarrese, and A. V. Olinto. Super Heavy Dark Matter in light of BICEP2, Planck and Ultra High Energy Cosmic Rays Observations. Journal of Cosmology and Astroparticle Physics, 2015(8):024, August 2015. doi: 10.1088/1475-7516/2015/08/024.

E. Amato and J. Arons. Heating and Nonthermal Particle Acceleration in Relativistic, Transverse Magnetosonic Shock Waves in Proton-Electron-Positron Plasmas. ApJ, 653(1):325–338, 2006.

S. Archambault et al. Gamma-Ray Observations of Tycho's Supernova Remnant with VERITAS and Fermi. ApJ, 836(1):23, February 2017. doi: 10.3847/1538-4357/836/1/23.

K. Asano and P. Mészáros. Neutrino and Cosmic-Ray Release from Gamma-Ray Bursts: Time-dependent Simulations. ApJ, 785(1):54, April 2014. doi: 10.1088/0004-637X/785/1/54.

W. I. Axford. The Origins of High-Energy Cosmic Rays. ApJS, 90:937, February 1994. doi: 10.1086/191928.

W. I. Axford, E. Leer, and G. Skadron. The Acceleration of Cosmic Rays by Shock Waves. In *International Cosmic Ray Conference*, volume 11 of *International Cosmic Ray Conference*, page 132, January 1977.

W. Baade and F. Zwicky. Remarks on Super-Novae and Cosmic Rays. *Physical Review*, 46(1):76–77, July 1934. doi: 10.1103/PhysRev.46.76.2.

P. Baerwald, M. Bustamante, and W. Winter. Are gamma-ray bursts the sources of ultra-high energy cosmic rays? *Astroparticle Physics*, 62:66–91, March 2015. doi: 10.1016/j.astropartphys.2014.07.007.

D. Bauer, P. Mulser, and W. H. Steeb. Relativistic ponderomotive force, Uphill acceleration, and transition to chaos. Phys. Rev. Lett., 75(25):4622–4625, December 1995. doi: 10.1103/PhysRevLett.75.4622.

J. Bednarz and M. Ostrowski. The acceleration time-scale for first-order Fermi acceleration in relativistic shock waves. MNRAS, 283(2):447–456, November 1996. doi: 10.1093/mnras/283.2.447.

M. C. Begelman and J. G. Kirk. "Shock-drift particle acceleration in superluminal shocks - A model for hot spots in extragalactic radio sources". ApJ, 353:66, 1990.

A. R. Bell. The acceleration of cosmic rays in shock fronts - I. MNRAS, 182:147–156, January 1978a. doi: 10.1093/mnras/182.2.147.

A. R. Bell. The acceleration of cosmic rays in shock fronts - II. MNRAS, 182:443–455, February 1978b. doi: 10.1093/mnras/182.3.443.

V. Berezinsky, M. Kachelrieß, and A. Vilenkin. Ultrahigh Energy Cosmic Rays without Greisen-Zatsepin-Kuzmin Cutoff. Phys. Rev. Lett., 79(22):4302–4305, December 1997. doi: 10.1103/PhysRevLett.79.4302.

V. Berezinsky, A. Gazizov, and S. Grigorieva. On astrophysical solution to ultrahigh energy cosmic rays. Phys. Rev. D, 74(4):043005, August 2006. doi: 10.1103/PhysRevD.74.043005.

V. S. Berezinsky and G. T. Zatsepin. Cosmic rays at ultrahigh-energies (neutrino?).

Phys. Lett. B, 28:423–424, 1969. doi: 10.1016/0370-2693(69)90341-4.

C. K. Birdsall and A. B. Langdon. *"Plasma Physics via Computer Simulation"*. The Adam Hilger Series on Plasma Physics., 1991.

R. D. Blandford and J. P. Ostriker. Particle acceleration by astrophysical shocks. ApJ, 221:L29–L32, April 1978. doi: 10.1086/182658.

P. Blasi. Origin of the Positron Excess in Cosmic Rays. Phys. Rev. Lett., 103(5):051104, July 2009. doi: 10.1103/PhysRevLett.103.051104.

A. Bohdan, J. Niemiec, O. Kobzar, and M. Pohl. Electron Pre-Acceleration at Nonrelativistic High-Mach-Number Perpendicular Shocks. ApJ, 847(1):71, 2017.

A. Bret and M. E. Dieckmann. How large can the electron to proton mass ratio be in particle-in-cell simulations of unstable systems? *Physics of Plasmas*, 17(3):032109, 2010.

O. Buneman. "Dissipation of Currents in Ionized Media". Phys. Rev. Lett., 1:8–9, 1959.

O. Buneman. "TRISTAN: The 3-d electromagnetic particle code.". In Matsumoto & Omura, editor, *Computer Space Plasma Physics: Simulation Techniques and Software*. Terra, Tokyo, 1993.

D. Burgess and M. Scholer. Shock front instability associated with reflected ions at the perpendicular shock. *Physics of Plasmas*, 14:012108–012108, 2007.

J. D. Callen. "Collective Plasma Phenomena". In *Fundamentals of Plasma Physics*. 2006.

A.C. Cangellaris and R. Lee. On the accuracy of numerical wave simulations based on finite methods. *Journal of Electromagnetic Waves and Applications*, 6(12):1635–1653, 1992. doi: 10.1163/156939392X00779.

C. J. Cesarsky. Cosmic-ray confinement in the galaxy. ARA&A, 18:289–319, January 1980. doi: 10.1146/annurev.aa.18.090180.001445.

Pisin Chen, Toshiki Tajima, and Yoshiyuki Takahashi. Plasma Wakefield Acceleration for Ultrahigh-Energy Cosmic Rays. Phys. Rev. Lett., 89(16):161101, October 2002. doi: 10.1103/PhysRevLett.89.161101.

I. M. Christie, M. Petropoulou, L. Sironi, and D. Giannios. Radiative signatures of plasmoid-dominated reconnection in blazar jets. MNRAS, 482(1):65–82, January 2019. doi: 10.1093/mnras/sty2636.

M. H. Cohen, W. Cannon, G. H. Purcell, D. B. Shaffer, J. J. Broderick, K. I. Kellermann, and D. L. Jauncey. The Small-Scale Structure of Radio Galaxies and Quasi-Stellar Sources at 3.8 Centimeters. ApJ, 170:207, December 1971. doi: 10.1086/151204.

National Research Council. *"Plasma Science: Advancing Knowledge in the National Interest"*. The National Academies Press, Washington, DC, 2007.

R. Courant, K. Friedrichs, and H. Lewy. "Über die partiellen Differenzengleichungen der mathematischen Physik". *Mathematische Annalen*, 100:32–74, 1928.

J. M. Dawson. "Particle simulation of plasmas". *Reviews of Modern Physics*, 55:403–477, 1983.

M. E. Dieckmann, B. Eliasson, M. Parviainen, P. K. Shukla, and A. Ynnerman. Electron surfing acceleration in oblique magnetic fields. MNRAS, 367:865–872, 2006.

J. F. Drake, P. K. Kaw, Y. C. Lee, G. Schmid, C. S. Liu, and M. N. Rosenbluth. Parametric instabilities of electromagnetic waves in plasmas. *Physics of Fluids*, 17:778–785, 1974.

G. Drenkhahn. Acceleration of GRB outflows by Poynting flux dissipation. A&A, 387: 714–724, May 2002. doi: 10.1051/0004-6361:20020390.

G. Drenkhahn and H. C. Spruit. Efficient acceleration and radiation in Poynting flux powered GRB outflows. A&A, 391:1141–1153, September 2002. doi: 10.1051/0004-6361:20020839.

L. Oc. Drury. An introduction to the theory of diffusive shock acceleration of energetic particles in tenuous plasmas. *Reports on Progress in Physics*, 46(8):973–1027, August 1983. doi: 10.1088/0034-4885/46/8/002.

L. O'C. Drury and J. H. Voelk. Hydromagnetic shock structure in the presence of cosmic rays. ApJ, 248:344–351, August 1981. doi: 10.1086/159159.

D. C. Ellison and G. P. Double. Diffusive shock acceleration in unmodified relativistic, oblique shocks. *Astroparticle Physics*, 22(3-4):323–338, November 2004. doi: 10.1016/j.astropartphys.2004.08.005.

D. C. Ellison, F. C. Jones, and S. P. Reynolds. First-Order Fermi Particle Acceleration by Relativistic Shocks. ApJ, 360:702, September 1990. doi: 10.1086/169156.

E. Esarey, P. Sprangle, J. Krall, and A. Ting. Overview of plasma-based accelerator concepts. *IEEE Transactions on Plasma Science*, 24(2):252–288, April 1996. doi: 10.1109/27.509991.

E. Fermi. On the Origin of the Cosmic Radiation. *Physical Review*, 75(8):1169–1174, April 1949. doi: 10.1103/PhysRev.75.1169.

E. Fermi. Galactic Magnetic Fields and the Origin of Cosmic Radiation. ApJ, 119:1, January 1954. doi: 10.1086/145789.

F. Filbet, E. Sonnendrücker, and P. Bertrand. "Conservative Numerical Schemes for the Vlasov Equation". *Journal of Computational Physics*, 172:166–187, 2001.

A. Friedman. "Damped time advance methods for particles and EM fields". In *US-Japan Workshop on Advanced Computer Simulation Techniques Applied to Plasmas and Fusion*. 1990.

W. Fugmann. Are all flat-spectrum radio source blazars ? *Astr. and Astrophys.*, 205:

86–92, 1988.

Y. A. Gallant, M. Hoshino, A. B. Langdon, J. Arons, and C. E. Max. Relativistic, Perpendicular Shocks in Electron-Positron Plasmas. ApJ, 391:73, 1992.

S. Gao, A. Fedynitch, W. Winter, and M. Pohl. Modelling the coincident observation of a high-energy neutrino and a bright blazar flare. *Nature Astronomy*, 3:88–92, January 2019. doi: 10.1038/s41550-018-0610-1.

G. Ghisellini and P. Madau. On the origin of the gamma-ray emission in blazars. MNRAS, 280:67–76, 1996.

D. Giannios, D. A. Uzdensky, and M. C. Begelman. Fast TeV variability in blazars: jets in a jet. MNRAS, 395(1):L29–L33, May 2009. doi: 10.1111/j.1745-3933.2009.00635.x.

V. L. Ginzburg and S. I. Syrovatsky. Origin of Cosmic Rays. *Progress of Theoretical Physics Supplement*, 20:1–83, January 1961. doi: 10.1143/PTPS.20.1.

C. C. Goodrich and J. D. Scudder. The adiabatic energy change of plasma electrons and the frame dependence of the cross-shock potential at collisionless magnetosonic shock waves. J. Geophys. Res., 89(A8):6654–6662, August 1984. doi: 10.1029/JA089iA08p06654.

M. Goossens. *"An Introduction to Plasma Astrophysics and Magnetohydrodynamics"*. Springer Netherlands., 2003.

A. D. Greenwood, K. L. Cartwright, J. W. Luginsland, and E. A. Baca. "On the elimination of numerical Cerenkov radiation in PIC simulations". *Journal of Computational Physics*, 201:665–684, 2004.

K. Greisen. End to the Cosmic-Ray Spectrum? Phys. Rev. Lett., 16(17):748–750, April 1966. doi: 10.1103/PhysRevLett.16.748.

F. Guo, H. Li, W. Daughton, and Y.-H. Liu. Formation of Hard Power Laws in the Energetic Particle Spectra Resulting from Relativistic Magnetic Reconnection. Phys. Rev. Lett., 113(15):155005, October 2014. doi: 10.1103/PhysRevLett.113.155005.

F. Guo, H. Li, W. Daughton, and Y.-H. Liu. Particle acceleration during magnetic reconnection in a low-beta pair plasma. *Physics of Plasmas*, 23(5):055708, May 2016. doi: 10.1063/1.4948284.

F. Guo, X. Li, W. Daughton, P. Kilian, H. Li, Y.-H. Liu, W. Yan, and D. Ma. Determining the Dominant Acceleration Mechanism during Relativistic Magnetic Reconnection in Large-scale Systems. ApJ, 879(2):L23, July 2019. doi: 10.3847/2041-8213/ab2a15.

J. Guo and Q.-M. Lu. Effects of ion-to-electron mass ratio on electron dynamics in collisionless magnetic reconnection. *Chinese Physics Letters*, 24(11):3199–3202, 2007.

M. F. Hadi and A. Picket-May. "A modified (2,4) scheme for modeling electrically large structures with high phase accuracy". *IEEE Transmission and Antennas Propagation*, 45:254–264, 1997.

F. Harlow. "A Machine Calculation Method for Hydrodynamic Problems". *Los Alamos Scientific Laboratory report*, 1956.

V. Hess. Über Beobachtungen der durchdringenden Strahlung bei sieben Freiballonfahrt. *Physikalische Zeitschrif*, 13:62, 1912.

A. M. Hillas. The Origin of Ultra-High-Energy Cosmic Rays. ARA&A, 22:425–444, January 1984. doi: 10.1146/annurev.aa.22.090184.002233.

A. M. Hillas. Cosmic Rays: Recent Progress and some Current Questions. *arXiv e-prints*, art. astro-ph/0607109, July 2006.

M. Honda, J. Meyer-ter Vehn, and A. Pukhov. Collective stopping and ion heating in relativistic-electron-beam transport for fast ignition. Phys. Rev. Lett., 85:2128–2131, 2000.

D. Hooper, S. Sarkar, and A. M. Taylor. The intergalactic propagation of ultra-high energy cosmic ray nuclei. *Astroparticle Physics*, 27(2-3):199–212, March 2007. doi: 10.1016/j.astropartphys.2006.10.008.

M. Hoshino. Wakefield Acceleration by Radiation Pressure in Relativistic Shock Waves. ApJ, 672:940–956, 2008.

M. Hoshino and J. Arons. Preferential positron heating and acceleration by synchrotron maser instabilities in relativistic positron-electron-proton plasmas. *Physics of Fluids B*, 3:818–833, 1991.

M. Hoshino, J. Arons, Y. A. Gallant, and A. B. Langdon. Relativistic magnetosonic shock waves in synchrotron sources - Shock structure and nonthermal acceleration of positrons. ApJ, 390:454–479, 1992.

N. Ikeya and Y. Matsumoto. Stability property of numerical Cherenkov radiation and its application to relativistic shock simulations. PASJ, 67(4):64, August 2015. doi: 10.1093/pasj/psv052.

C. D. Impey, C. R. Lawrence, and S. Tapia. Optical Polarization of a Complete Sample of Radio Sources. ApJ, 375:46, 1991.

M. Iwamoto, T. Amano, M. Hoshino, and Y. Matsumoto. Persistence of Precursor Waves in Two-dimensional Relativistic Shocks. ApJ, 840:52, 2017.

M. Iwamoto, T. Amano, M. Hoshino, and Y. Matsumoto. Precursor Wave Emission Enhanced by Weibel Instability in Relativistic Shocks. ApJ, 858:93, 2018.

M. Iwamoto, T. Amano, Y. Hoshino, M.and Matsumoto, J. Niemiec, A. Ligorini, O. Kobzar, and M. Pohl. Precursor Wave Amplification by Ion-Electron Coupling through Wakefield in Relativistic Shocks. *in print,* ApJ, 2019.

Idunn B. Jacobsen, Kinwah Wu, Alvina Y. L. On, and Curtis J. Saxton. High-energy neutrino fluxes from AGN populations inferred from X-ray surveys. MNRAS, 451 (4):3649–3663, August 2015. doi: 10.1093/mnras/stv1196.

J. R. Jokipii, J. Kota, and J. Giacalone. Perpendicular transport in 1- and 2-dimensional shock simulations. Geophys. Res. Lett., 20(17):1759–1761, September 1993. doi: 10.1029/93GL01973.

Tsunehiko N. Kato and Hideaki Takabe. Nonrelativistic Collisionless Shocks in Weakly Magnetized Electron-Ion Plasmas: Two-dimensional Particle-in-cell Simulation of Perpendicular Shock. ApJ, 721(1):828–842, September 2010. doi: 10.1088/0004-637X/721/1/828.

P. Kaw, G. Schmidt, and T. Wilcox. Filamentation and trapping of electromagnetic radiation in plasmas. *Physics of Fluids*, 16:1522–1525, 1973.

A. Keivani, K. Murase, M. Petropoulou, D. B. Fox, S. B. Cenko, S. Chaty, A. Coleiro, J. J. DeLaunay, S. Dimitrakoudis, P. A. Evans, J. A. Kennea, F. E. Marshall, A. Mastichiadis, J. P. Osborne, M. Santand er, A. Tohuvavohu, and C. F. Turley. A Multimessenger Picture of the Flaring Blazar TXS 0506+056: Implications for High-energy Neutrino Emission and Cosmic-Ray Acceleration. ApJ, 864(1):84, September 2018. doi: 10.3847/1538-4357/aad59a.

C. F. Kennel and F. V. Coroniti. "Confinement of the Crab pulsar's wind by its supernova remnant". ApJ, 283:694–709, 1984.

J. G. Kirk and P. Schneider. Particle Acceleration at Shocks: A Monte Carlo Method. ApJ, 322:256, November 1987. doi: 10.1086/165720.

J. G. Kirk, O. Skjæraasen, and Y. A. Gallant. Pulsed radiation from neutron star winds. A&A, 388:L29–L32, June 2002. doi: 10.1051/0004-6361:20020599.

M. D. Kistler, T. Stanev, and H. Yüksel. Cosmic PeV neutrinos and the sources of ultrahigh energy protons. Phys. Rev. D, 90(12):123006, December 2014. doi: 10.1103/PhysRevD.90.123006.

Y. L. Klimontovich. "Physics of collisionless plasma". *Physics-Uspekhi*, 40(1):21, 1997.

N. A. Krall and A. W. Trivelpiece. *Principles of Plasma Physics* . International series in pure and applied physics. McGraw-Hill, 1973.

W. L. Kruer. The physics of laser plasma interactions. volume 73 of *Frontiers in Physics Lecture Note Series*, pages 165–172, 1988.

Y. Kuramitsu, Y. Sakawa, T. Kato, H. Takabe, and M. Hoshino. Nonthermal Acceleration of Charged Particles due to an Incoherent Wakefield Induced by a Large-Amplitude Light Pulse. ApJ, 682:L113, 2008.

P. O. Lagage and C. J. Cesarsky. The maximum energy of cosmic rays accelerated by supernova shocks. A&A, 125:249–257, September 1983.

L. D. Landau and E. M. Lifshitz. *"Course of Theoretical Physics, Volume 6: Fluid Mechanics"*. Pergamon Press, Oxford, 1959.

A. B. Langdon. "Implicit Plasma Simulation". *Space Science Reviews*, 42:67–83, 1985.

A.|B. Langdon, J. Arons, and C. E. Max. Structure of relativistic magnetosonic shocks in electron-positron plasmas. Phys. Rev. Lett., 61(7):779–782, August 1988. doi: 10.1103/PhysRevLett.61.779.

L. C. Lee, J. R. Kan, and C. S. Wu. Generation of auroral kilometric radiation and the structure of auroral acceleration region. Planet. Space Sci., 28(7):703–711, 1980.

A. Letessier-Selvon and T. Stanev. Ultrahigh energy cosmic rays. *Reviews of Modern Physics*, 83(3):907–942, July 2011. doi: 10.1103/RevModPhys.83.907.

R. E. Lowe and D. Burgess. The properties and causes of rippling in quasi-perpendicular collisionless shock front. *Annals of Geophysics*, 21, 2003.

Y. E. Lyubarskii. A model for the energetic emission from pulsars. A&A, 311:172–178, July 1996.

Y. Lyubarsky. Electron-Ion Coupling Upstream of Relativistic Collisionless Shocks. ApJ, 652:1297–1305, 2006.

Y. E. Lyubarsky. On the relativistic magnetic reconnection. MNRAS, 358(1):113–119, March 2005. doi: 10.1111/j.1365-2966.2005.08767.x.

K. Mannheim, R. J. Protheroe, and J. P. Rachen. Cosmic ray bound for models of extragalactic neutrino production. Phys. Rev. D, 63(2):023003, January 2001. doi: 10.1103/PhysRevD.63.023003.

W. Marshall. The Structure of Magneto-Hydrodynamic Shock Waves. *Proceedings of the Royal Society of London Series A*, 233(1194):367–376, December 1955. doi: 10.1098/rspa.1955.0272.

S. F. Martins, R. A. Fonseca, L. O. Silva, and W. B. Mori. Ion Dynamics and Acceleration in Relativistic Shocks. ApJ, 695(2):L189–L193, April 2009. doi: 10.1088/0004-637X/695/2/L189.

A. Meli. Diffusive and Shock-Drift Acceleration in Relativistic Shocks. *Few-Body Systems*, 53(1-2):157–165, July 2012. doi: 10.1007/s00601-011-0254-5.

A. Meli and J. J. Quenby. Particle acceleration in ultra-relativistic parallel shock waves. *Astroparticle Physics*, 19(5):637–648, August 2003a. doi: 10.1016/S0927-6505(02)00256-6.

A. Meli and J. J. Quenby. Particle acceleration in ultra-relativistic oblique shock waves. *Astroparticle Physics*, 19(5):649–666, August 2003b. doi: 10.1016/S0927-6505(02)00257-8.

D. B. Melrose, R. G. Hewitt, and G. A. Dulk. Electron-cyclotron maser emission: Relative growth and damping rates for different modes and harmonics. *Journal of Geophysics Research*, 89(A2):897–904, 1984.

M. Milgrom and V. Usov. Possible Association of Ultra–High-Energy Cosmic-Ray Events with Strong Gamma-Ray Bursts. ApJ, 449:L37, August 1995. doi: 10.1086/

309633.

Y. Mizuno, M. Pohl, J. Niemiec, B. Zhang, K. I. Nishikawa, and P. E. Hardee. Magnetic-field Amplification by Turbulence in a Relativistic Shock Propagating Through an Inhomogeneous Medium. ApJ, 726(2):62, January 2011. doi: 10.1088/0004-637X/726/2/62.

Y. Mizuno, M. Pohl, J. Niemiec, B. Zhang, K. I. Nishikawa, and P. E. Hardee. Magnetic field amplification and saturation in turbulence behind a relativistic shock. MNRAS, 439(4):3490–3503, April 2014. doi: 10.1093/mnras/stu196.

G. Morlino and D. Caprioli. Acceleration of cosmic rays in Tycho's SNR. Mem. Soc. Astron. Italiana, 82:731, January 2011.

Gerard A. Mourou, Toshiki Tajima, and Sergei V. Bulanov. Optics in the relativistic regime. *Reviews of Modern Physics*, 78(2):309–371, April 2006. doi: 10.1103/RevModPhys.78.309.

K. Murase, Y. Inoue, and C. D. Dermer. Diffuse neutrino intensity from the inner jets of active galactic nuclei: Impacts of external photon fields and the blazar sequence. Phys. Rev. D, 90(2):023007, July 2014. doi: 10.1103/PhysRevD.90.023007.

K. Nalewajko, D. Giannios, M. C. Begelman, D. A. Uzdensky, and M. Sikora. Radiative properties of reconnection-powered minijets in blazars. MNRAS, 413(1):333–346, May 2011. doi: 10.1111/j.1365-2966.2010.18140.x.

K. Nalewajko, J. Zrake, Y. Yuan, W. E. East, and R. D. Blandford. Kinetic Simulations of the Lowest-order Unstable Mode of Relativistic Magnetostatic Equilibria. ApJ, 826 (2):115, August 2016. doi: 10.3847/0004-637X/826/2/115.

K. Nalewajko, Y. Yuan, and M. Chruślińska. Kinetic simulations of relativistic magnetic reconnection with synchrotron and inverse Compton cooling. *Journal of Plasma Physics*, 84(3):755840301, June 2018. doi: 10.1017/S0022377818000624.

J. Niemiec and M. Ostrowski. Cosmic-Ray Acceleration at Relativistic Shock Waves with a "Realistic" Magnetic Field Structure. ApJ, 610(2):851–867, August 2004. doi: 10.1086/421730.

J. Niemiec and M. Ostrowski. Cosmic Ray Acceleration at Ultrarelativistic Shock Waves: Effects of a "Realistic" Magnetic Field Structure. ApJ, 641(2):984–992, April 2006. doi: 10.1086/500541.

J. Niemiec, M. Ostrowski, and M. Pohl. Cosmic-Ray Acceleration at Ultrarelativistic Shock Waves: Effects of Downstream Short-Wave Turbulence. ApJ, 650(2):1020–1027, October 2006. doi: 10.1086/506901.

J. Niemiec, M. Pohl, T. Stroman, and K.-I. Nishikawa. "Production of Magnetic Turbulence by Cosmic Rays Drifting Upstream of Supernova Remnant Shocks". ApJ, 684:1174–1189, 2008.

H. Okuda. "Numerical solution of inital boundary value problems involving Maxwell's

equations in isotropic media". *Journal of Computational Physics*, 10:475–486, 1972.

J. Ortuño-Macías and K. Nalewajko. Radiative kinetic simulations of steady-state relativistic plasmoid magnetic reconnection. *arXiv e-prints*, art. arXiv:1911.06830, November 2019.

M. Ostrowski. Monte Carlo simulations of energetic particle transport in weakly inhomogeneous magnetic fields. I - Particle acceleration in relativistic shock waves with oblique magnetic fields. MNRAS, 249:551–559, April 1991. doi: 10.1093/mnras/249.3.551.

T. J. Pearson, S. C. Unwin, M. H. Cohen, R. P. Linfield, A. C. S. Readhead, G. A. Seielstad, R. S. Simon, and R. C. Walker. Superluminal expansion of quasar 3C273. Nature, 290(5805):365–368, April 1981. doi: 10.1038/290365a0.

B. M. Peterson. Variability of Active Galactic Nuclei. In Itziar Aretxaga, Daniel Kunth, and Raúl Mújica, editors, *Advanced Lectures on the Starburst-AGN*, 2001.

I. Plotnikov and L. Sironi. The synchrotron maser emission from relativistic shocks in Fast Radio Bursts: 1D PIC simulations of cold pair plasmas. MNRAS, 485(3): 3816–3833, May 2019. doi: 10.1093/mnras/stz640.

I. Plotnikov, A. Grassi, and M. Grech. Perpendicular relativistic shocks in magnetized pair plasma. MNRAS, 477(4):5238–5260, July 2018. doi: 10.1093/mnras/sty979.

M. Pohl, M. Hoshino, and J. Niemiec. PIC simulation methods for cosmic radiation and plasma instabilities. *Progress in Particle and Nuclear Physics*, 111:103751, March 2020. doi: 10.1016/j.ppnp.2019.103751.

P. W. Rambo, J. J. Ambrosiano, A. Friedman, and D. E. Nielsen, Jr. "Temporal and spatial filtering remedies for dispersion in electromagnetic particle codes". In *13th Conference on the Numerical Simulation of Plasmas, Santa Fe, NM,17-20 Sep.* 1989.

M. J. Rees. Appearance of Relativistically Expanding Radio Sources. Nature, 211(5048): 468–470, July 1966. doi: 10.1038/211468a0.

M. J. Rees. Black Hole Models for Active Galactic Nuclei. *Annual Review of Astronomy and Astrophysics*, 22:471–506, 1984.

M. Sikora, M. C. Begelman, G. M. Madejski, and J.-P. Lasota. Are Quasar Jets Dominated by Poynting Flux? ApJ, 625:72–77, 2005a.

M. Sikora, G. M. Madejski, J.-P. Lasota, and M. C. Begelman. Are Quasar Jets Matter or Poynting Flux Dominated? In Tomasz Bulik, Bronislaw Rudak, and Grzegorz Madejski, editors, *Astrophysical Sources of High Energy Particles and Radiation*, volume 801 of *American Institute of Physics Conference Series*, pages 165–172, 2005b.

M. Sikora, M. Janiak, K. Nalewajko, G. M. Madejski, and R. Moderski. On the Origin of X-Ray Spectra in Luminous Blazars. ApJ, 779(1):68, 2013.

L. Sironi and A. Spitkovsky. Particle Acceleration in Relativistic Magnetized

Collisionless Pair Shocks: Dependence of Shock Acceleration on Magnetic Obliquity. ApJ, 698(2):1523–1549, June 2009. doi: 10.1088/0004-637X/698/2/1523.

L. Sironi and A. Spitkovsky. "Particle Acceleration in Relativistic Magnetized Collisionless Electron-Ion Shocks". ApJ, 726:75, 2011.

L. Sironi and A. Spitkovsky. Relativistic Reconnection: An Efficient Source of Non-thermal Particles. ApJ, 783(1):L21, March 2014. doi: 10.1088/2041-8205/783/1/L21.

L. Sironi, A. Spitkovsky, and J. Arons. The Maximum Energy of Accelerated Particles in Relativistic Collisionless Shocks. ApJ, 771(1):54, 2013.

P. Slane, S. H. Lee, D. C. Ellison, D. J. Patnaude, J. P. Hughes, K. A. Eriksen, D. Castro, and S. Nagataki. A CR-hydro-NEI Model of the Structure and Broadband Emission from Tycho's Supernova Remnant. ApJ, 783(1):33, March 2014. doi: 10.1088/0004-637X/783/1/33.

M. Spada, G. Ghisellini, D. Lazzati, and A. Celotti. Internal shocks in the jets of radio-loud quasars. MNRAS, 325:1559–1570, 2001a.

M. Spada, D. Lazzati, G. Ghisellini, and A. Celotti. Internal shocks in the jets of blazars. *Memorie della Societa Astronomica Italiana*, 72:157–159, 2001b.

A. Spitkovsky. On the structure of relativistic collisionless shocks in electron-ion plasmas. ApJ, 673(1):L39–L42, dec 2007.

P. Sprangle, V. L. Granatstein, and A. Drobot. The electron cyclotron maser instability. *Journal de Physique*, 38(12):C6–135, December 1977.

A Stockem, F. Fiúza, R. A. Fonseca, and L. O. Silva. "Acceleration in perpendicular relativistic shocks for plasmas consisting of leptons and hadrons". ApJ, 755:68–79, 2012.

T. Tajima and J. M. Dawson. Laser electron accelerator. Phys. Rev. Lett., 43(4):267–270, July 1979. doi: 10.1103/PhysRevLett.43.267.

M. Tanaka, C. C. Goodrich, D. Winske, and K. Papadopoulos. A source of the backstreaming ion beams in the foreshock region. J. Geophys. Res., 88(A4):3046–3054, April 1983. doi: 10.1029/JA088iA04p03046.

M. F. Thomsen, H. C. Barr, S. Peter Gary, W. C. Feldman, and T. E. Cole. Stability of electron distributions within the earth's bow shock. J. Geophys. Res., 88(A4):3035–3045, April 1983. doi: 10.1029/JA088iA04p03035.

R. A. Treumann. Fundamentals of collisionless shocks for astrophysical application, 1. Non-relativistic shocks. A&A Rev., 17(4):409–535, December 2009. doi: 10.1007/s00159-009-0024-2.

T. Umeda. "Study on Nonlinear Processes of Electron Beam Instabilities via Computer Simula- tions". *PhD thesis, Graduate School of Informatics, Kyoto*, 2004.

T. Umeda, Y. Omura, T. Tominaga, and H. Matsumoto. "A new charge conservation method in electromagnetic particle-in-cell simulations". *Computer Physics Communications*, 156:73–85, 2003.

T. Umeda, Y. Kidani, S. Matsukiyo, and R. Yamazaki. Dynamics and microinstabilities at perpendicular collisionless shock: A comparison of large-scale two-dimensional full particle simulations with different ion to electron mass ratio. *Physics of Plasmas*, 21(2):022102, 2014.

C. M. Urry and P. Padovani. Unified Schemes for Radio-Loud Active Galactic Nuclei. *Publication of the Astronomical Society of the Pacific*, 107:803, 1995.

E. Valtaoja, H. Terasranta, S. Urpo, N. S. Nesterov, M. Lainela, and M. Valtonen. Five years monitoring of extragalactic radio sources. IV. Variability statistics and unified models for AGN. A&A, 254:80, 1992.

J. L. Vay. "Simulation of beams or plasmas crossing at relativistic velocity". *Physics of Plasmas*, 10, 2008.

T. Vuillaume, G. Henri, and P. O. Petrucci. A stratified jet model for AGN emission in the two-flow paradigm. A&A, 620:A41, November 2018. doi: 10.1051/0004-6361/201731899.

S. P. Wakely and D. Horan. TeVCat: An online catalog for Very High Energy Gamma-Ray Astronomy. In *International Cosmic Ray Conference*, volume 3 of *International Cosmic Ray Conference*, pages 1341–1344, January 2008.

J. F. C. Wardle, D. C. Homan, R. Ojha, and D. H. Roberts. Electron-positron jets associated with the quasar 3C279. Nature, 395(6701):457–461, October 1998. doi: 10.1038/26675.

W. R. Webber. A New Estimate of the Local Interstellar Energy Density and Ionization Rate of Galactic Cosmic Cosmic Rays. ApJ, 506(1):329–334, October 1998. doi: 10.1086/306222.

T. C. Weekes et al. VERITAS: the Very Energetic Radiation Imaging Telescope Array System. *Astroparticle Physics*, 17(2):221–243, May 2002. doi: 10.1016/S0927-6505(01)00152-9.

G. R. Werner, D. A. Uzdensky, B. Cerutti, K. Nalewajko, and M. C. Begelman. The Extent of Power-law Energy Spectra in Collisionless Relativistic Magnetic Reconnection in Pair Plasmas. ApJ, 816(1):L8, January 2016. doi: 10.3847/2041-8205/816/1/L8.

V. Wieland, M. Pohl, J. Niemiec, I. Rafighi, and K.-I. Nishikawa. Nonrelativistic Perpendicular Shocks Modeling Young Supernova Remnants: Nonstationary Dynamics and Particle Acceleration at Forward and Reverse Shocks. ApJ, 820(1):62, 2016. doi: 10.3847/0004-637X/820/1/62.

Reva Kay Williams. Collimated Escaping Vortical Polar e^-e^+ Jets Intrinsically Produced by Rotating Black Holes and Penrose Processes. ApJ, 611(2):952–963, August 2004.

doi: 10.1086/422304.

B. J. Wills, D. Wills, M. Breger, R. R. J. Antonucci, and R. Barvainis. A Survey for High Optical Polarization in Quasars with Core-dominant Radio Structure: Is There a Beamed Optical Continuum? ApJ, 398:454, 1992.

D. Winske and K. B. Quest. Magnetic field and density fluctuations at perpendicular supercritical collisionless shocks. *Journal of Geophysics Research*, 93:9681–9693, 1988.

C. S. Wu and L. C. Lee. A theory of the terrestrial kilometric radiation. ApJ, 230:621–626, 1979.

K. Yee. "Numerical solution of inital boundary value problems involving maxwell's equations in isotropic media.". *IEEE Transmission and Antennas Propagation*, 14:302–307, 1966.

G. T. Zatsepin and V. A. Kuz'min. Upper Limit of the Spectrum of Cosmic Rays. *Soviet Journal of Experimental and Theoretical Physics Letters*, 4:78, August 1966.

Bing Zhang and Pawan Kumar. Model-Dependent High-Energy Neutrino Flux from Gamma-Ray Bursts. Phys. Rev. Lett., 110(12):121101, March 2013. doi: 10.1103/PhysRevLett.110.121101.